# Understanding of voltage decay in Li-excess Mn-Ni-Co transition-metal layered oxides

Seungjun Myeong

Department of Energy Engineering

(Battery Science and Technology)

Graduate School of UNIST

2018

# Understanding of voltage decay in Li-excess Mn-Ni-Co transition-metal layered oxide

Seungjun Myeong

Department of Energy Engineering
(Battery Science and Technology)

Graduate School of UNIST

# Understanding of voltage decay in Li-excess Mn-Ni-Co transition-metal layered oxides

A dissertation

submitted to the Graduate School of UNIST

in partial fulfillment of the requirements for the degree of

Doctor of Philosophy in Energy Engineering

Seungjun Myeong

06. 11. 2018

Approved by

Advisor

Jaephil Cho

# Understanding of voltage decay in Li-excess Mn-Ni-Co transition-metal layered oxides

Seungjun Myeong

This certifies that the dissertation of Seungjun Myeong is approved.

06. 11. 2018

Advisor: Jaephil Cho

Youngsik Kim

Nam-Soon Choi

Seok Ju Kang

Hyun-Wook Lee

# Abstract

In spite of the successful achievement in rechargeable lithium-ion battery, much more challenges, especially in terms of high energy density with low cost, are remained for EV (electrical vehicles) and ESS (energy storage systems). High capacity Li-excess 3*d*-transition-metal (3*d*TM) layered oxides ($Li_{1+x}Mn_yNi_zCo_{1-x-y-z}O_2$) are considered as a realistic candidate material for nearby battery market era because of the high reversible capacity exceeding 250 mAh $g^{-1}$ and price competitiveness came from cheap manganese price. The structural uniqueness and electrochemical characteristics of Li-excess 3*d*TM layered oxide materials have been intensively investigated by many research groups. Li-excess 3*d*TM layered cathode exhibits a highest initial discharge capacity approximately 250 mAh $g^{-1}$ among the cathode material such as LCO, NCA, and NCM due to the activation of $Li_2MnO_3$ component. Nevertheless, industrial application of Li/Mn-rich material is still challenging due to their low initial coulombic efficiency, inferior rate capability and severe discharge voltage decaying.

Voltages exceeding 4.40 V (vs. $Li^+/Li$) oxidize the alkyl carbonates (electrolyte decomposition) with the occurrence of the side-reaction in the electrolyte. Excessive oxidation (lithium extraction) and the oxygen extraction through high voltage leads to transition metal (TM) ions migration from TM sites in the TM layer to neighboring Li vacancies in Li layer, resulting in structural degradation from layered to spinel-like phase. Consequently, the Li-excess 3dTM cathode materials experience continuous voltage decaying during cycling. Therefore, to commercialize Li-excess 3dTM cathode materials, improvement on discharge average voltage retention and rate capability must be achieved. Therefore, researches with diverse approaches and in-depth understanding of the material characteristics are necessary to improve energy density of Li-excess 3dTM cathode materials for next generation.

In this dissertation, I start with brief review of the studies addressing voltage decay in Li-excess 3d-transition-metal layered oxides in chapter 1 with the recent progress of interpretation on voltage decay phenomenon and research strategies to mitigate voltage decay for increasing energy-density retention. Then after, i introduced my research results addressing voltage decay phenomenon in Li-excess 3d-transition-metal layered oxide for mitigating average discharge voltage drop and expanding the understanding of original voltage decay mechanism. Especially, Li-excess 3d-transition-metal layered oxide considered as a realistic candidate material for nearby battery market era because of the high reversible capacity exceeding 250 mAh $g^{-1}$ and price competitiveness came from cheap manganese price.

In chapter 2, I synthesized novel $Al(OH)_3$ nanosheet coating concept on $Li_{1.12}[Ni_{0.2}Co_{0.2}Mn_{0.6}]_{0.88}O_2$ through a delicately planned coating chemistry yielding a fully enveloping coating morphology with controlled thickness of 4 nm. This layer inhibits the continuous degradation mechanism, and retains surface structure by trapping $PF_6^-$ anions and protecting the surface from unstable side reactions. As a result, surface treated materials showed superior voltage retention as well as improved cycle/rate

performances compared to conventional coating methods, both at 25 °C and 60 °C. The enhanced performance confirmed by HAADF-STEM, XPS and EIS analysis.

In chapter 3, i synthesized partially disordered Li-excess 3d-transition-metal layered oxide and discovered a fundamental reason of the voltage decay phenomenon by comparing ordered and pre-disordered materials with a combination of X-ray absorption spectroscopy and transmission electron microscopy studies. The cation arrangement determines the TM-O covalency and structural reversibility related to voltage decay. The identification of structural arrangement with de-lithiated oxygen-centred octahedron ($M_4O$) and interactions between $M_4O$ octahedrons affecting the oxygen stability and TM mobility of transition-metal oxide provides a new insight into the degradation chemistry of cathode materials and a way to develop high-energy density electrodes.

# Contents

# List of Figures

**Figure 2-5.** Morphology comparison for pristine, CC-LNMC, and PC-LNMC. SEM images of (a) Pristine, (b) CC-LNMC, and (c) PC-LNMC. (d) SEM-EDS mapping image of PC-LNMC. (e,f) Simulated structure of $Al(OH)_3$ and $Al_2O_3$ coating material, respectively.

**Figure. 2-6.** Inductively coupled plasma-atomic emission spectroscopy (ICP-AES) data of pristine, PC-LNMC, and CC-LNMC. ICP data shows the same amount of Al (0.66 wt%) was used for both $Al_2O_3$ and $Al(OH)_3$ coating.

**Figure. 2-7.** Chemical composition analysis with HRTEM-EDS.

**Figure 2-8.** HF generation mechanism in lithium ion battery and anion trapping mechanism of $Al(OH)_3$ coating layer.

**Figure 2-9.** Schematic view for anion trapping mechanism of $Al(OH)_3$ coating layer.

**Figure 2-10.** Anion trapping mechanism of $Al(OH)_3$ coating layer. (a) FTIR-ATR analysis of pristine, before and after cycling. (b) XPS analysis for F1s of CC-LNMC after cycling. (c) FTIR-ATR analysis of pristine, before and after cycling. (d) XPS analysis for F1s of CC-LNMC after cycling.

**Figure 2-11.** Comparison of electrochemical performances and structural analysis *via* TEM. (a) Comparison of 0.5C cycle retention at 25 °C. (b) Comparison of 0.5C cycle retention at 60 °C. (c) Voltage profile change of pristine during 0.5C cycle at 25 °C. (d) Voltage profile change of CC-LNMC during 0.5C cycle at 25 °C. (e) TEM image of pristine before cycling. (f) TEM image of CC-LNMC before cycling. (g) TEM image of pristine after cycling. (h) TEM image of CC-LNMC after cycling. All TEM images are obtained along $[3\ 1\ 0]_{monoclinic}$ zone axis.

**Figure 2-12.** Separator from disassembled half-cell of (a) pristine, (b) PC-LNMC, (c) CC-LNMC after 100 cycles between 2.0 - 4.6 V at 60℃. (d,e) SEM images showing by-product particles on the separator. (f) Energy dispersive X-ray spectroscopy (EDS) spectrum of a particle attached to the separator, indicating that the particles are composed of F, P and O (82 : 7.5 : 10).

**Figure 2-13.** Comparison of electrochemical performances between PC-LNMC and CC-LNMC. Cycle retention test at (a) 25 °C, and (b) 60 °C. (c) Voltage profile change of PC-LNMC during 0.5C cycle at 25 °C.

**Figure 2-14.** TEM image of pristine material after cycling.

**Figure 2-15.** Changes in dQ/dV plots of (a) Pristine, (b) PC-LNMC, and (c) CC-LNMC during 0.5C cycle retention test at 25 °C. (d) Comparison of dQ/dV plots after 200 cycles.

**Figure 3-7.** Average discharge voltage values of the OL-MNC, OH-MNC and D-MNC at each cycle.

**Figure 3-8. Transition-metal K-edge *operando* XANES variation during cycling.** Mn, Ni, and Co K-edge o*perando* XANES spectra (2D contour plot) and voltage profiles of (**a**) OH-MNC $10^{th}$, (**b**) D-MNC $10^{th}$ , (**c**) OH-MNC $100^{th}$, and (**d**) D-MNC $100^{th}$**;** Crossline intensity of Mn K-edge *operando* XANES spectra peaks (**e**) A and B; (**f**) C and D during $10^{th}$ cycle; Electrodes were cycled at 0.5C-rate charge 1.0C-rate discharge condition.

**Figure 3-9. Oxidation state variation of Mn ion for OL-MNC, OH-MNC and D-MNC during cycling.** Mn K-edge spectra of a) OL-MNC on $10^{th}$ cycling b) OH-MNC on $10^{th}$ cycling c) OH-MNC on $100^{th}$ cycling d) D-MNC on $10^{th}$ cycling e) D-MNC on $100^{th}$ cycling.

**Figure 3-10. Oxidation state variation of Ni ion for OL-MNC, OH-MNC and D-MNC during cycling.** Ni K-edge spectra of a) OL-MNC on $10^{th}$ cycling b) OH-MNC on $10^{th}$ cycling c) OH-MNC on $100^{th}$ cycling d) D-MNC on $10^{th}$ cycling e) D-MNC on $100^{th}$ cycling.

**Figure 3-11. Oxidation state variation of Co ion for OL-MNC, OH-MNC and D-MNC during cycling.** Co K-edge spectra of a) OL-MNC on $10^{th}$ cycling b) OH-MNC on $10^{th}$ cycling c) OH-MNC on $100^{th}$ cycling d) D-MNC on $10^{th}$ cycling e) D-MNC on $100^{th}$ cycling.

**Figure 3-12. XANES peak energy values of the OL-MNC, OH-MNC and D-MNC at Initial, charged and discharged state.**

**Figure 3-13. *Operando* XANES characterization of the OL-MNC during cycling.** Normalized Mn, Ni and Co K-edge *operando* XANES spectra (2D contour plot) and voltage profiles of OL-MNC on $10^{th}$ cycling.

**Figure 3-14. Crossline intensity of Ni K-edge *operando* XANES spectra during $10^{th}$ cycle.**
Crossline intensity of a) peak A; b) peak B; c) peak; C d) peak D

**Figure 3-15. Crossline intensity of Co K-edge *operando* XANES spectra during $10^{th}$ cycle.**
Crossline intensity of a) peak A; b) peak B; and c) peak C

**Figure 3-16. Oxygen stability of TM-O bonding and electron hole localization on oxygen.** Oxygen K-edge SXAS spectrum of (**a**) OL-MNC (**b**) OH-MNC (**c**) D-MNC; the spectra collected on Pristine, $10^{th}$ cycled and $100^{th}$ cycled particle. (**d**) Schematic diagram of the possible $O^{-}/O^{2-}$ redox couple position base on TM-O covalency variation observed in O K-edge SXAS.

**Figure 3-17.** STXM images of pristine O-MNC, D-MNC and cycled samples (10th and 100th cycled OL-MNC, OH-MNC and D-MNC)

**Figure 3-18.** Variation of the integrated intensity in the pre-edge peak region (shaded region in **Fig. 3-16a-c**) for O K-edge SXAS.

**Figure 3-19. Evolution of atomic structure.** HAADF-STEM image of the (**a**) $[100]_{mono}$ Pristine O-MNC (**b**) $[100]_{mono}$ Pristine O-MNC (**c**) $[310]_{mono}$ OH-MNC, (**d**) $[100]_{mono}$ OH-MNC**,** (**e**) $[310]_{mono}$ D-MNC and (**f**) $[100]_{mono}$ D-MNC particle after 100 charge-discharge cycles. Enlarged HAADF/ABF-STEM images of the surface region in images **c** and **d** with simulate HAADF/ABF-STEM images (in the inset) are presented; Scale bar denote 1nm.

**Figure 3-20. Structure model of $LiTMO_2$ and $Li_2TMO_3$ phase which consist of Li-excess 3*d*-transition-metal oxide** a) $LiTMO_2$ phase b) $Li_2TMO_3$ phase along [310]mono and [100]mono zone axis**; HAADF-STEM images, FFT patterns and signal profile of pristine O-MNC and D-MNC samples along [310]mono and [100]mono zone axis.** c) O-MNC [310]mono d) O-MNC [100]mono e) D-MNC [310]mono f) D-MNC [100]mono.

**Figure 3-21. Atomic structure analysis and identifying.** a) $[310]_{mono}$ direction HAADF-STEM image of $100^{th}$ cycled OH-MNC and b) collected FFT patterns were matched with simulated atomic structure model and simulated FFT pattern, respectively. c) Magnified HAADF-STEM image containing domain boundary. d) Signal profile of the region marked in grey and blue in image.

**Figure 3-22. Atomic structure analysis and identifying.** a) $[100]_{mono}$ direction HAADF-STEM image of $100^{th}$ cycled OH-MNC and b) collected FFT patterns were matched with simulated atomic structure model and simulated FFT pattern, respectively. c) Magnified HAADF-STEM image containing domain boundary. d) Signal profile of the region marked in grey and blue in image.

**Figure 3-23. HAADF-STEM images, FFT patterns and signal profile of 100th cycled D-MNC samples along [310]mono and [100]mono zone axis.** a) D-MNC [310]mono b) D-MNC [100]mono.

**Figure 3-24. HR-TEM image of pristine O-MNC/D-MNC samples and $100^{th}$ cycled OH-MNC/D-MNC for EDS mapping analysis.** Theoretical and experimental O/TM ratio result of pristine O-MNC/D-MNC and $100^{th}$ cycled OH-MNC/D-MNC from EDS mapping analysis.

**Figure 3-25. EDS line scan signal counts of Pristine and $100^{th}$ cycled OH-MNC /D-MNC samples.** Degree of elemental signal count change of a) Oxygen, b) Ni, c) Mn, and d) Co from outer-surface to 30nm.

**Figure 3-26. Comparison of surface atomic rearrangement of OH-MNC and D-MNC on long cycling**. a) The image plot of oxygen ratio line mapping (30nm long) for cycled OH-MNC and D-MNC

from surface region. The intensity represented as color scale bare shown on up. b) Schematic of surface structure rearrangement at $[310]_{mono}$ and $[100]_{mono}$ zone direction.

**Figure 3-27. Powder XRD pattern of pristine O-MNC, D-MNC and cycled samples (10 and 100 cycles).** a) OL-MNC, b) OH-MNC, and c) D-MNC.

**Figure 3-28.** Schematic diagram of scattering paths in the TM atomic arrangements within the ab plane.

**Figure 3-29.** Radial distribution function (RDF) of (a) Mn, (b) Ni, and (c) Co K-edge k3-weighted EXAFS spectra as a function of interatomic distance for pristine electrode of OH-MNC and D-MNC.

**Figure 3-30. Migration of specific elements due to the structural instability.** (**a**) Radial distribution function (RDF) of Mn, Ni, and Co K-edges $k^3$-weighted EXAFS spectra for pristine and $100^{th}$ cycled electrode of OH-MNC and D-MNC; Comparison of OH-MNC and D-MNC K-edge o*perando* EXAFS spectra (2D contour plot) collected during $10^{th}$ and $100^{th}$ cycle. Spectra represents (**b**) TM-O peak and (**c**) TM-A peak variation of Mn, Ni, and Co K-edges.

**Figure 3-31.** Radial distribution function (RDF) of (a) Mn, (b) Ni, and (c) Co K-edge k3-weighted EXAFS spectra as a function of interatomic distance for Pristine O-MNC, $10^{th}$ cycled and $100^{th}$ cycled electrode of OL-MNC.

**Figure 3-32.** Oxygen-centred structure model of pristine O-MNC and D-MNC (**a**) Three oxygen-centred octahedron ($M_6O$) of Li-excess material. Each oxygen anions coordinated by six cations with different portion of $Li^+$ and transition-metal in TM and Li layer. 2TM-O-4Li, 3TM-O-3Li and 4TM-O-2Li octahedron represent the base structure of $Li_2TMO_3$, $LiTMO_2$ and disordered-$LiTMO_2$ (**b**) Oxygen-centred macroscopic structure model of pristine O-MNC and D-MNC along $[100]_{mono}$.

**Figure 3-33. Factors to consider in interpreting the structural stability of high capacity cathode material.** (**a**) Three de-lithiated oxygen-centred octahedron ($M_4O$) of Li-excess material. Each oxygen anions coordinated by four cations and two lithium vacancies ($V_{Li}$) with different portion of $Li^+$ and transition-metal in TM and Li layer. 2TM-O-2Li [$2V_{Li}$], 3TM-O-1Li [$2V_{Li}$] and 4TM-O-0Li [$2V_{Li}$] octahedron represent the base structure of de-lithiated $Li_2TMO_3$, $LiTMO_2$ and pre-disordered-$LiTMO_2$, and the degree of stability on centred oxygen represented as different color (Red is highly labile); (**b**) Oxygen-centred macroscopic structure model of de-lithiated state OH-MNC and D-MNC along $[100]_{mono}$ (**c**) Schematic of structure stability according to the material characteristics

## List of publications

I contributed to the following publications during my PhD course.

**Peer-reviewed publications**

1. Cho W., **Myeong S**., Kim N., Lee S., Kim Y., Kim M., Kang S., Park N.*, Oh P.*, Cho J.* ”Critical Role of Cations in Lithium Sites on Extended Electrochemical Reversibility of Co-Rich Layered Oxide” **Adv. Mat.**, 29, 1605578 (**2017**).
2. Zheng J.†, **Myeong S**.†, Cho W., Yan P., Xiao J., Wang C., Cho J.*, Zhang J.* ” Li- and Mn-Rich Cathode Materials: Challenges to Commercialization” **Adv. Energy Mater.**, 7, 1601284 (**2017**).
3. Kalluri S., Yoon M., Jo M., Park S., **Myeong S**., Kim J., Dou S., Guo Z.*, Cho J.* ”Surface Engineering Strategies of Layered LiCoO2 Cathode Material to Realize High-Energy and High-Voltage Li-Ion Cells”, **Adv. Energy Mater.**, 7, 1601507 (**2017**).
4. Han J., Park I., Cha J., Park S., Park S., **Myeong S**., Cho W., Kim S., Hong S., Cho J.*, Choi N.* “Interfacial Architectures Derived by Lithium Difluoro(bisoxalato) Phosphate for Lithium-Rich Cathodes with Superior Cycling Stability and Rate Capability” **ChemElectroChem.**, 4, 1600184 (**2017**).
5. Oh P., Oh S., Li W., **Myeong S**., Cho J.*, Manthiram A.* ”High-Performance Heterostructured Cathodes for Lithium-Ion Batteries with a Ni-Rich Layered Oxide Core and a Li-Rich Layered Oxide Shell”, **Advanced Science.**, 3, 1600184 (**2016**).
6. Liu W., Oh P., Liu X., **Myeong S**., Cho W., Cho J.* “Countering Voltage Decay and Capacity Fading of Lithium-Rich Cathode Material at 60$^{o}$C by Hybrid Surface Protection Layers”, **Adv. Energy Mater.**, 5, 1500274 (**2015**).
7. Oh P., **Myeong S**., Cho W., Lee M., Ko M., Jeong H., Cho J.* “Superior long-term energy retention and volumetric energy density for Li-rich cathode matrials”, **Nano Lett.**, 14, 5965-5972 (**2014**)
8. Oh P., Ko M., **Myeong S**., Kim Y., Cho J.* “A Novel Surface Treatment Method and New Insight into Discharge voltage Deterioration for High-performance 0.4Li2MnO3-0.6LiNi1/3Co1/3Mn1/3O2 Cathode Materials”, **Adv. Energy Mater.**, 4, 1400631 (**2014**).

# Chapter 1

## Introduction of voltage decay in Li-excess 3d-transition-metal layered oxides

## 1.1 Introduction

In spite of the successful achievement in rechargeable lithium-ion battery, much more challenges, especially in terms of high energy density with low cost, are remained for EV (electrical vehicles) and ESS (energy storage systems).[1, 2] High capacity Li-excess 3*d*-transition-metal (3*d*TM) layered oxides ($Li_{1+x}Mn_yNi_zCo_{1-x-y-z}O_2$) are considered as a realistic candidate material for nearby battery market era because of the high reversible capacity exceeding 250 mAh $g^{-1}$ and price competitiveness came from cheap manganese price.[3-9] The structural uniqueness and electrochemical characteristics of Li-excess 3*d*TM layered oxide materials have been intensively investigated by many research groups.[10-13] Li-excess 3*d*TM layered cathode exhibits a highest initial discharge capacity approximately 250 mAh $g^{-1}$ among the cathode material such as LCO, NCA, and NCM due to the activation of $Li_2MnO_3$ component.[7, 14-16]Nevertheless, industrial application of Li/Mn-rich material is still challenging due to their low initial coulombic efficiency, inferior rate capability and severe discharge voltage decaying. [10, 17, 18] The crystal structure of Li-excess 3dTM cathode materials is composed of $LiTMO_2$ phase with rhombohedral R-3m space group and monoclinic $Li_2TMO_3$ phase with C2/m space group (**Fig. 1-1a, b**).

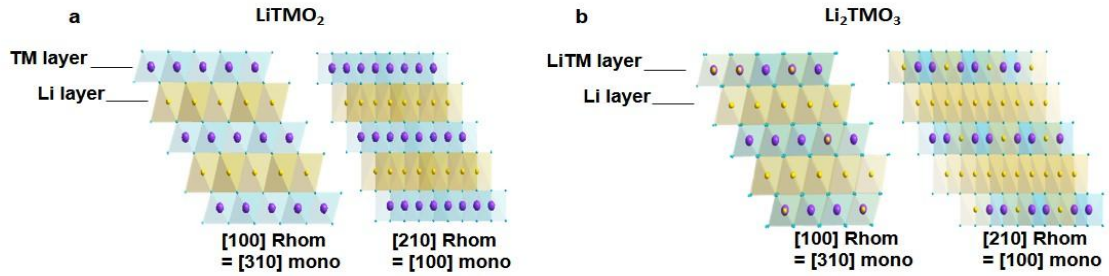


**Figure. 1-1** Schematic view of the (a) $LiTMO_2$ phase (space group: R-3m, TM = Ni, Co, and Mn) along with [310]mono zone-axis, and (b) $Li_2TMO_3$ phase (space group: C2/m) along with [100]mono zone-axis.

This part was reproduced from Zheng J, Myeong S, Cho W, Yan P, Xiao J, Wang C, *et al.* Li- and Mn-Rich Cathode Materials: Challenges to Commercialization. *Adv. Energy. Mater.* **2017,** 7.

Voltage decaying phenomenon is closely associated with the wide voltage window, 2.00 - 4.40 V~4.80 V vs. Li-metal which is required to activate the $Li_2MnO_3$ phase for high discharge capacity, and the structural instability attributed to the excessive hole creation in the O2p orbital and labile oxygen state which leads oxygen release from the lattice during cycling. Furthermore, High voltage conditions (4.60 - 4.80 V vs. Li-metal) to operate Li-excess 3*d*TM layered cathode materials is upper than the electrochemically stable range of typical organic electrolytes. Voltages exceeding 4.40 V (vs. $Li^+/Li$) oxidize the alkyl carbonates (electrolyte decomposition) with the occurrence of the side-reaction in the electrolyte.[19] Consequently, accumulation of a by-products and the thick SEI (solid electrolyte interface) layer on the cathode-electrolyte interface lead to increase of cell impedance and electrochemical performance degradation during charge and discharge processes. Excessive oxidation (lithium extraction) and the oxygen extraction through high voltage leads to transition metal (TM) ions migration from TM sites in the TM layer to neighboring Li vacancies in Li layer, resulting in structural degradation from layered to spinel-like phase.[18, 20] consequently, the Li-excess 3dTM cathode materials experience continuous voltage decaying during cycling. Therefore, to commercialize Li-excess 3dTM cathode materials, improvement on discharge average voltage retention and rate capability must be achieved. Therefore, researches with diverse approaches and in-depth understanding of the material characteristics are necessary to improve energy density of Li-excess 3dTM cathode materials for next generation.

## 1.2 Cation focused voltage decay mechanism

At a low charge cut-off voltage of 4.4 V, Li-excess 3dTM cathode materials can cycle well without voltage decaying,[21] which however is at the expense of a low discharge capacity < 150 mAh $g^{-1}$. The superior discharge capacity of Li-excess 3dTM cathode materials obtained through high cut-off voltage (4.6 ~ 4.8 V) to activate the $Li_2MnO_3$ phase via removal of $Li^+$ ions accompanied with an irreversible oxygen loss.[6, 22] The initial redox mechanism of Li-excess 3dTM cathode materials is different from the typical layered cathode (NCM, NCA, and LCO) materials.[6, 22-26] During the initial redox process called as activation, a substantial amount of oxygen are released with the formation of oxygen vacancies. Consequently, the TM ions coordinated with labile oxygen ions or oxygen vacancies are destabilized and migrate to the vacant octahedral sites in Li layers through the neighbouring tetrahedral sites.[27] Furthermore, researchers have been considered thick SEI layer on the electrode surface derived from side reactions between the extracted oxygen species and the electrolyte as a reason of electrochemical performance degradation including cell impedance and voltage degradation.[28] Even though the thick SEI layer also contributes to over-potential during discharge process occurred by electrode polarization, the intrinsic cation migration is considered to be the reason accounting for voltage decaying of Li-excess 3dTM cathode materials.

### 1.2.1 Structural evolution and voltage decaying

The structural degradation is initiate from the cathode material surface where the electrolyte is directly contact and causes the formation of a surface reconstruction layer which shows the oxygen deficient phase. The surface reconstruction structure has been investigated and is described at a 'spinel' phase.[18, 20, 27, 29-31] Through XRD/TEM techniques, however, there was no sufficient analysis data to conclude that the surface reconstruction structure in cycled Li-excess 3dTM cathode materials is a pure $LiMn_2O_4$ spinel structure. Therefore, researches have been explore the detailed structure of the 'spinel' phase to investigate the surface structural degradation pathway.[32-34] Oh et al and Zheng et al. proposed a structural degradation mechanism of Li-excess 3dTM cathode materials as a sequence from 'spinel-like phase' to 'cubic rock-salt phase' to investigate the improvement mechanism of a surface treatment.[32] As shown in **Fig. 1-2**, they referred that the layered structure of Li-excess 3dTM cathode material ($Li_{1.17}Ni_{0.17}Co_{0.17}Mn_{0.5}O_2$) transforms to spinel-like phase and then further converts to rock-salt phase due to the high charge voltage of 4.6 V. In this article, the formation of spinel-like phase and disordered rock-salt phase are considered to be the reason for the capacity decay and voltage decaying of Li-excess 3dTM cathode material during cycling.

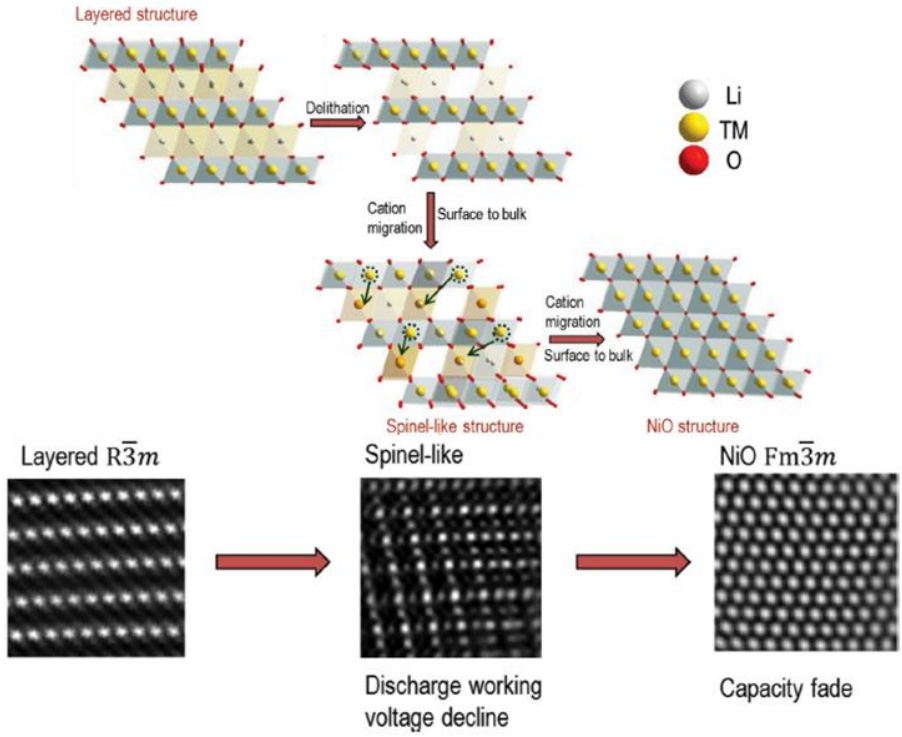


**Figure. 1-2** Schematics of structural degradation sequence from the *R*-3*m* layered phase to the *Fm*-3*m* cubic rock-salt structure during the electrochemical cycling.[32]

The detailed phase transition pathway of the Li-excess 3dTM cathode material is additionally proposed by Zheng et al. in **Fig. 1-3a**. The structure of Li-excess 3dTM cathode material is transformed from R-3m layered structure to LT-$LiCoO_2$ type defect spinel-like structure and then converted to a disordered rock-salt structure during cycling. According to recent findings,[35, 36] disordered rock-salt structure formation (cation disordering) is occurred in certain Li-excess cathode materials which all TM ions involves in the electrochemical redox reactions. The reversible Lithium ion in-/de-intercalation occurred in disordered rock-salt structure has been attributed to the Li-excess structure that permits Li percolation regardless of the increased kinetic barrier. Excess Lithium ion environment in the structure is indispensable to reach the threshold (x =1.1 ~ 1.2 in $Li_xTM_{2-x}O_2$) of a Li ion percolating network (1-TM and the 0-TM channels) in the disordered rock-salt structure. (**Fig. 1-3b**).[37]

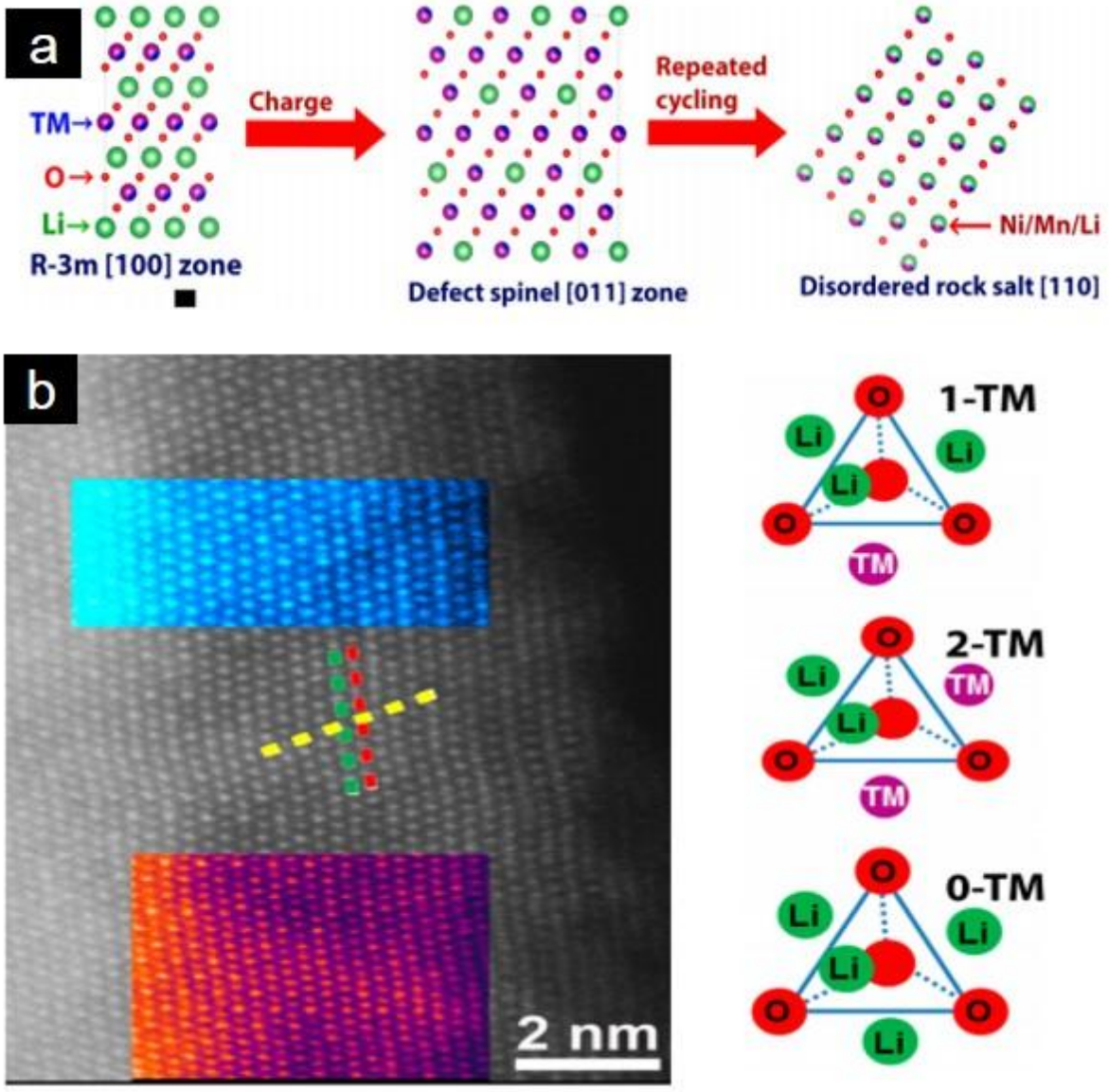


**Figure. 1-3** Crystal structural evolution of Li-excess 3dTM cathode material during cycling. (a) Schemetic view of structural evolution pathway by using atomic models. (b) High resolution Z-contrast image showing the rock-salt structure and possible environment for the Li diffusion in TM oxide [33]

### 1.2.2 Ni, Co, and Mn interlayer mixing from TM layer to Li layer

It have been reported that Ni substituent can stabilize the layered structure of Li-excess 3dTM cathode material.[38-40] The proposed possible mechanism of structure stabilization is that strong interlayer mixing between Ni ion and Li ion, where Ni ions perform as pillars with prevent structural transformation and stabilize original layered structure during cycling, demonstrating less voltage decaying.[41, 42] In the past, Ni ion and Li ion interlayer mixing has been confirmed by diffraction analysis tools such as X-ray diffraction (XRD) and neutron diffraction.[43-46] Yan et al. utilized advanced STEM technique with energy dispersive spectroscopy (EDS) to visually investigate the cation interlayer mixing in several layered TM oxides.[47]

Direct visualization of interlayer mixing of cations could provide direct evidence and help to understand deep insights of phenomenon. HAADF-STEM image with EDS mapping results for $Li_{1.2}Ni_{0.13}Co_{0.13}Mn_{0.54}O_2$ sample to investigate the cation interlayer mixing shown **in Fig 1-4**. Interestingly, Mn, Ni, and Co K map shows different behavior in crystal structure. Mn K map, main element in the TM layer of $Li_{1.2}Ni_{0.13}Co_{0.13}Mn_{0.54}O_2$ shows the clear confinement. However, different behavior in sub elements Co ion and Ni ion were observed by EDS mapping and line scan profiles. While the Co K map shows a well-resolved layered structure (**Fig. 1-4c**), Ni K map shows random distribution of Ni (**Fig. 1-4d**). Furthermore, integrated line scan profile provided quantitative X-ray counts for Mn, Ni, and Co (**Fig. 1-4e**).

As a result, Ni and Co ion line profiles are different despite of total counts are similar, consistent with EDS mapping result. Based on the analysis result, they calculated interlayer mixing level of Co and Ni ion. it is estimated that only 4% Co ion mixed with Li ion in interlayer while 41% Ni ion mixed (**Fig. 1-4f**). For the $Li_{1.2}Ni_{0.13}Co_{0.13}Mn_{0.54}O_2$ cathode, negligible interlayer mixing were observed for Mn and Co ion in contrast to Ni ion, which shows significantly higher interlayer mixing and suggested atomic model for $Li_{1.2}Ni_{0.13}Co_{0.13}Mn_{0.54}O_2$ is shown in **Fig. 1-4g**

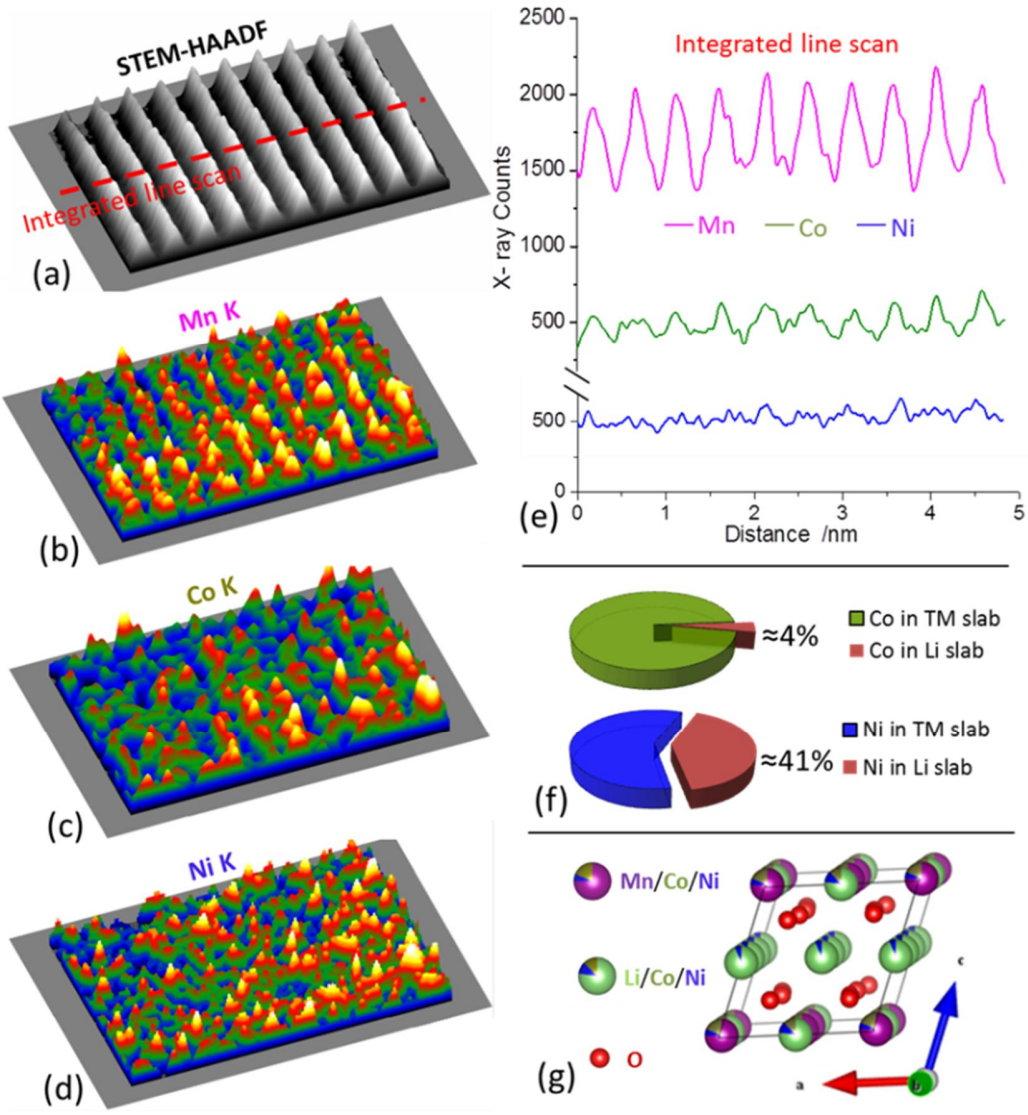


**Figure. 1-4** (a) HAADF- STEM image of $Li_{1.2}Ni_{0.13}Co_{0.13}Mn_{0.54}O_2$ sample along [010] zone-axis. Surface plot image of (b) Mn K map, (c) Co K map, (d) Ni K map. (e) Integrated line scan profile; X-ray counts shows the atomic distribution across the layered structure. (f) Calcultated occupancy ratio based on counts that from TM-layer and Li-layer. (g) Suggested atomic model for Li-excess 3dTM cathode material ($Li_{1.2}Ni_{0.13}Co_{0.13}Mn_{0.54}O_2$).[47]

## 1.3 Strategies to Mitigate Voltage Decaying

To address the voltage decaying issue which hinder the practical applications of Li-excess 3dTM cathode material, various strategies have been employed to mitigate voltage decaying without degradation of electrochemical performances in Li-excess 3dTM cathode material during cycling. So far, identified fundamental reason for the voltage decaying of Li-excess 3dTM cathode material is intrinsic structural instability and irreversible structural degradation (layered phase → spinel-like phase → disordered rock-salt phase). Representative approaches to mitigate voltage decaying phenomenon of Li-excess 3dTM cathode material have been introduced these days such as improving cation uniformity,[48] preferring crystal orientation,[49] lattice doping with certain atoms,[50] surface modification,[28] using proper electrolyte additives[28] and efficient binders,[51] manipulating the electrochemical process.[52, 53]

### 1.3.1 Mitigate Voltage decaying by improving Atomic Uniformity in crystal structure

Gu et al. reported that Li-excess 3dTM cathode material $Li[Li_{0.2}Ni_{0.2}M_{0.6}]O_2$ prepared by co-precipitation method forms segregation of Ni ions at a selective surface lattice plane.[54] This particular atomic segregation causes a higher kinetic barrier at the particle surface, which interfere the lithium ion diffusion at interface between cathode material and electrolyte, and consequent electrochemical performance degradation such as poor rate capability and voltage decaying during cycling. In this regard, properties of Li-excess 3dTM cathode material could be decided by the TM ions homogeneity in materials atomic structure. Since Ni and Mn ion distribution in crystal structure shows close relationship with synthetic conditions, Zheng et al. designed the synthesis of Li-excess 3dTM cathode material and optimized synthesis process to enhance the uniformity of Ni distribution and thus improve the performances of Li-excess 3dTM cathode material.

$Li[Li_{0.2}Ni_{0.2}M_{0.6}]O_2$, Li-excess 3dTM cathode material were synthesized by co-precipitation (CP), sol-gel (SG) and hydrothermal-assisted (HA) methods to investigate the correlation between atomic distribution and voltage decaying.[48] High efficient EDS mapping result in **Fig 1-5** clearly demonstrated that Mn and Ni ion in $Li[Li_{0.2}Ni_{0.2}M_{0.6}]O_2$ material synthesized by hydrothermal-assisted (HA) method are uniformly distributed in contrast with prepared by CP and SG methods, showing Ni segregation at the particle surface (**Fig. 1-5a**). Furthermore, the uniformity of TM ion without segregation leads to the superior electrochemical performance, exhibiting a stable rate capability and cycle retention (**Fig. 1-5b, c**).

The $Li[Li_{0.2}Ni_{0.2}M_{0.6}]O_2$ material synthesized by hydrothermal-assisted (HA) method shows a ~0.15 V decrease in average discharge voltage over 200 cycles, much smaller than 0.25 V decrease for $Li[Li_{0.2}Ni_{0.2}M_{0.6}]O_2$ material synthesized by co-precipitation (CP) method (**Fig. 1-5d, e**), indicating an

structural stabilization and mitigated cation migration during cycling. HAADF-STEM image demonstrate that the structural difference for HA and CP material. As a result, two phases were observed in CP material presented in **Fig. 1-6a**: rhombohedral $LiMO_2$ (R-3m phase) and monoclinic $Li_2MnO_3$ (C2/m phase).[6, 55-57] In contrast, the C2/m structure dominates in most regions of the HA material particles originating from the homogeneous cation distribution (**Fig. 1-6b**)

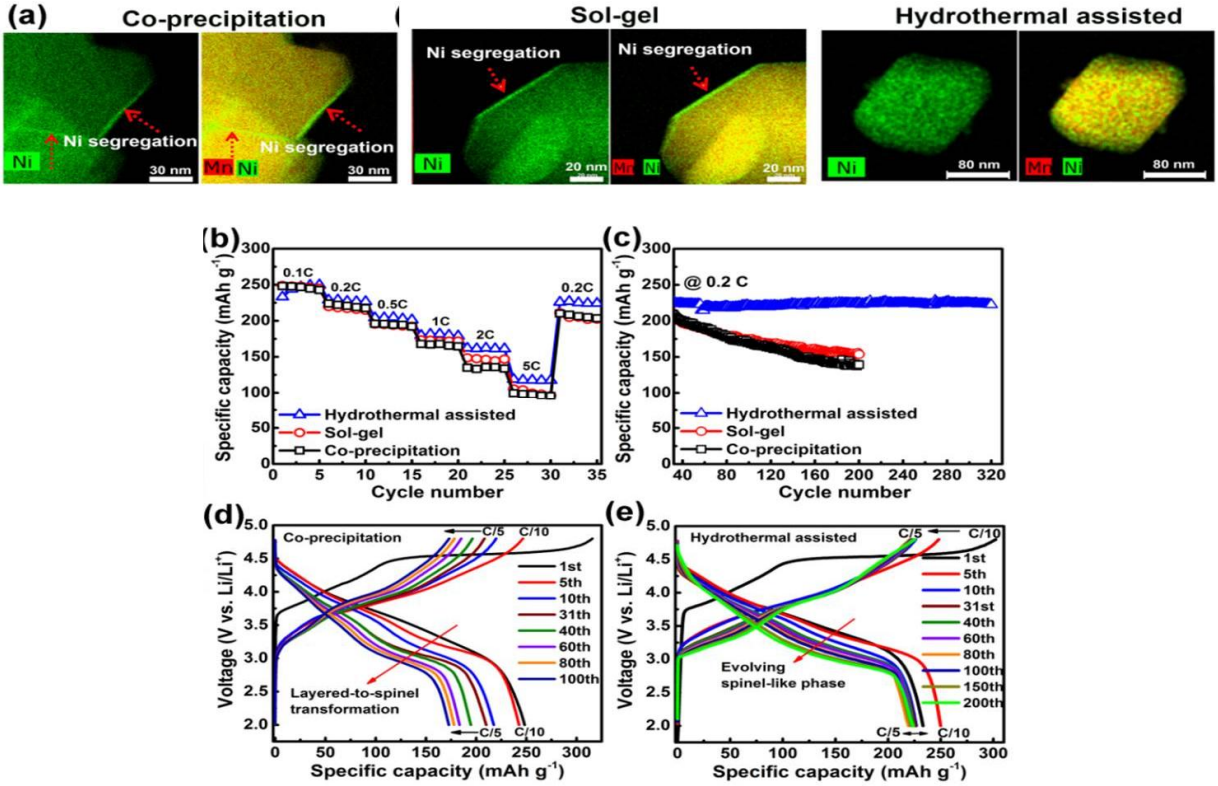


**Figure. 1-5** Comparison of $Li[Li_{0.2}Ni_{0.2}M_{0.6}]O_2$ Li-excess 3dTM cathode material prepared by different methods. (a) Bulk and surface EDS mapping image (b) rate performance and (c) cycle retention. (d, e) Voltage profile change of $Li[Li_{0.2}Ni_{0.2}M_{0.6}]O_2$ prepared by (d) CP method and (e) HA method during cycling.[48]

Li-excess 3dTM cathode material are generally represented with two interchangeable notations: x $Li_2MnO_3$·(1-x) $LiMO_2$ (two phase nanocomposite) and $Li_{1+x}M_{1-x}O_2$ (single phase solid solution). These observations provided some clues to address the current debate whether Li-excess 3dTM cathode material is composed of nanocomposite or a solid solution.[58-60] According to experimental result, structure of Li-excess 3dTM cathode material is closely related to the synthesis method. $Li_2MO_3$ structure domination (M

= Ni and Mn) (C2/m phase) in Li-excess 3dTM cathode material crystal structure increase structure stability upon excessive oxidation (de-lithiation process), resulting in significantly prolonging the cycle retention and mitigating the voltage decaying. According to the assertion of Thackeray et al, interactions between Ni and Mn ion preserve the average oxidation state of Mn ions at above 3+.[61, 62] Ni segregation at material surface weakens total Ni-Mn interactions, leading to unbalance of Mn oxidation number and reduction of Mn ions, resulting in severe voltage decaying. Improved Ni homogeneity in crystal structure enhances the Ni-Mn interactions and stabilizes the structure stability of $Li[Li_{0.2}Ni_{0.2}M_{0.6}]O_2$ material.

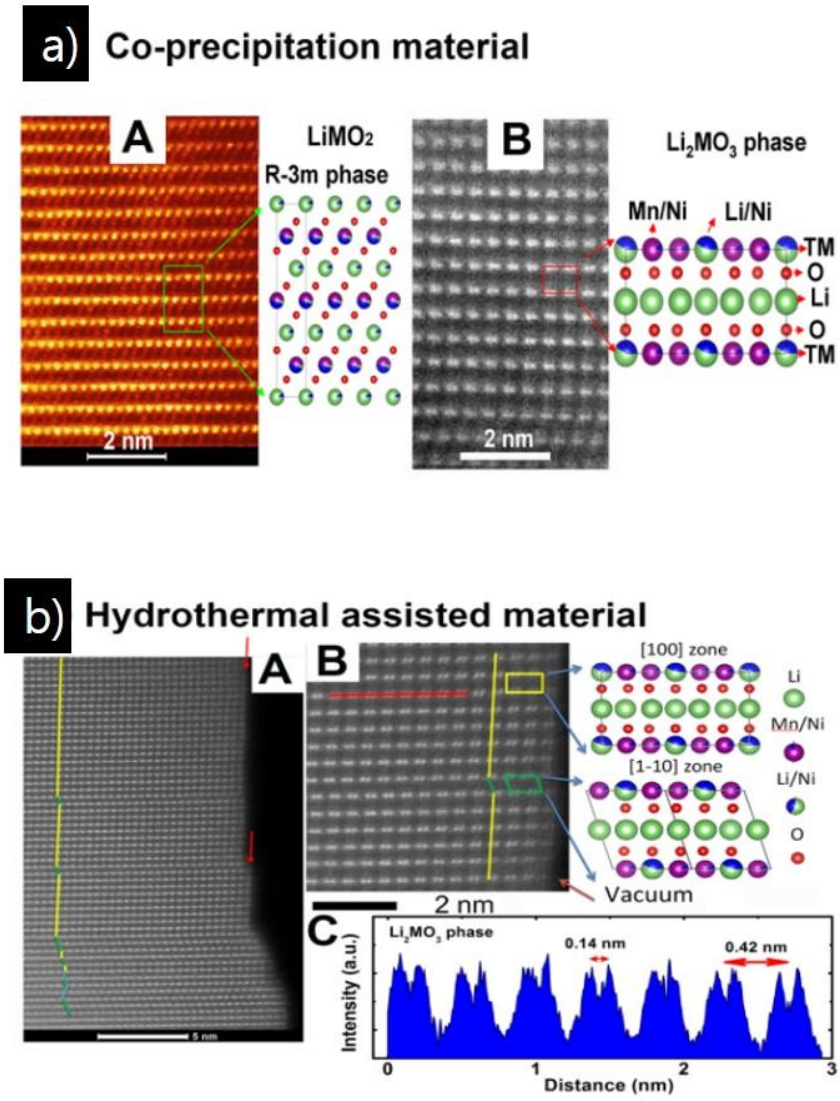


**Figure. 1-6** STEM imaging of (a) CP and (b) HA materials. In panel (a): (A) Crystal structure and atomic model of the R-3m phase along [310]mono zone-axis; (B) crystal structure and atomic model of the C2/m phase along [100]mono zone-axis.[48]

### 1.3.2 Mitigate Voltage Decaying by Atomic Transition-metal site substitution

For atomic site substitution, partial lattice doping of TM ions with Al,[50, 63] Ti,[64] Mo,[65] Ru,[66] Cr,[67, 68] Mg,[50, 69] in Li-excess 3dTM cathode material have been reported to improve structural stability and thus diminish the voltage decaying phenomenon. Previous cation substitution works are only focused on improving the long-term cycling retention and capacity rather than observing the average discharge voltage retention which is the important issues of Li-excess 3dTM cathode material for commercialization.

Recently, Nayak et al. reported that Al substituted Li-excess 3dTM cathode material $Li_{1.2}Ni_{0.16}Mn_{0.56-x}Al_xCo_{0.08}O_2$ increase the long-term cycling retention even though the slight reduced of discharge capacity (**Fig. 1-7**).[50] However, Al substitution alleviated the voltage decaying of Li-excess 3dTM cathode material by suppressing the structural degradation (phase transformation) from layered structure to spinel-like structure, which observed by charge/discharge voltage profiles during cycling (**Fig. 1-7c-f**).

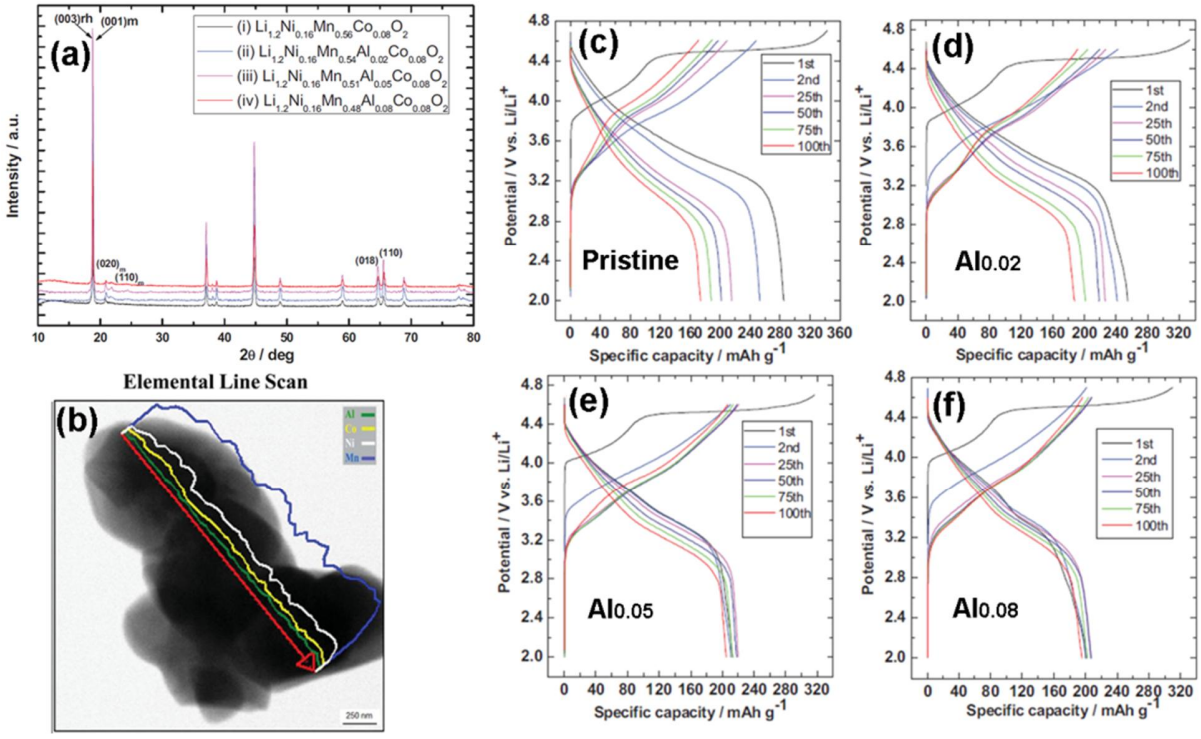


**Figure. 1-7** (a) XRD patterns of $Li_{1.2}Ni_{0.16}Mn_{0.56-x}Al_xCo_{0.08}O_2$. (b) EDS line scan profile of Al, Mn, Ni, and Co over the particles. Voltage profiles of (c) $Li_{1.2}Ni_{0.16}Mn_{0.56}Co_{0.08}O_2$, (d) $Li_{1.2}Ni_{0.16}Mn_{0.54}Al_{0.02}Co_{0.08}O_2$, (e) $Li_{1.2}Ni_{0.16}Mn_{0.51}Al_{0.05}Co_{0.08}O_2$, and (f) $Li_{1.2}Ni_{0.16}Mn_{0.48}Al_{0.08}Co_{0.08}O_2$ electrodes. All electrodes are operated in the potential range of 2.0–4.6 V at 25 mA $g^{-1}$ after formation process (2.0–4.7 V).[50]

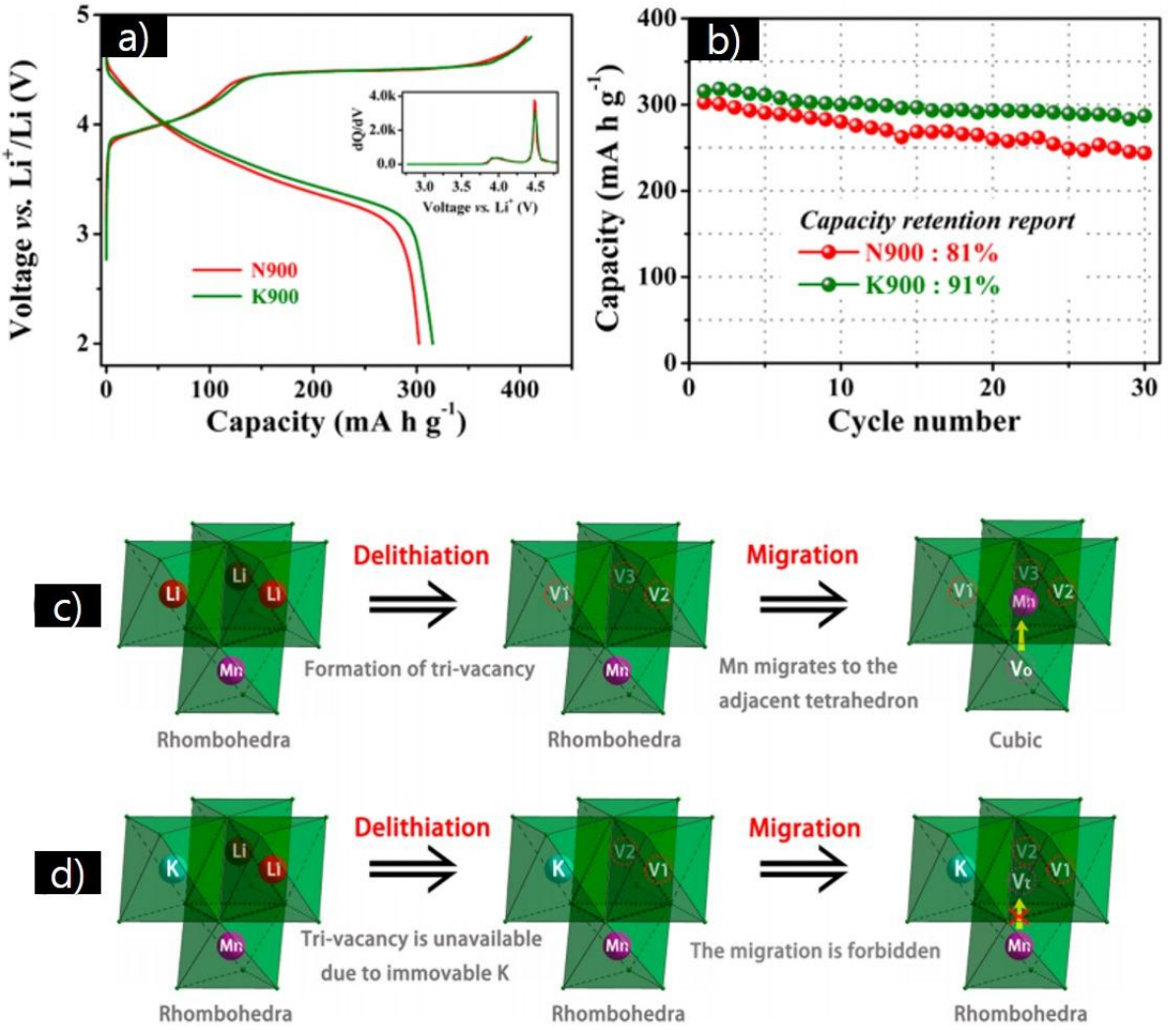


**Figure. 1-8** Comparison of $Li_{1.163}Ni_{0.138}Mn_{0.56}Co_{0.140}O_2$ and $K^+$ substituted $Li_{1.151}Ni_{0.145}Mn_{0.552}Co_{0.146}K_{0.013}O_2$. (a) initial voltage profiles; (b) cycle retention in the potential range of 2.0–4.6 V at 20mA $g^{-1}$ (c) Schematic illustration of the phase evolution sequence for $Li_{1.163}Ni_{0.138}Mn_{0.56}Co_{0.140}O_2$ and $Li_{1.151}Ni_{0.145}Mn_{0.552}Co_{0.146}K_{0.013}O_2$.[70]

Besides 3dTM site substitution, lithium site substitution with other alkali cations such as $Na^+$ and $K^+$ have been optimized to stabilize the layered structure of Li-excess 3dTM cathode material.[70-73] the fixed pillars in the Li layers via $Na^+$ and $K^+$ ions substitution in the lithium sites act as fixing pillars in the Li layers, improving the structural stability of Li-excess 3dTM cathode material during excessive oxidation (lithium ion re-/de-intercalation) (**Fig. 1-8**). $K^+$ ion substitution were proposed by Li et al. that the doped $K^+$ ions interfere the tri-vacancies formation in Li layer, which hinders the 3dTM ions migration from TM site to Li site in lithium layer.[70] Furthermore, partial anion substitution of $F^-$ (1.33 Å) for $O^{2-}$ (1.40 Å) has been conducted to enhance the structural stability and diminish the voltage decaying phenomenon in Li-excess 3dTM cathode material.[4, 74, 75] However, incorporation anion redox of F anion in the Li-excess 3dTM cathode material results in the discharge capacity decrease, which originate from the strong M-F/Li-F bonding interaction and increase of primary particle size.

### 1.3.3 Mitigate Voltage Decaying by Surface modification.

There are two representative reasons contributing to voltage decaying phenomenon of lithium ion battery system, which using Li-excess 3dTM cathode material as a cathode material. One is the intrinsic structural evolution during repeated cycling.[76, 77] Another reason is arisen from the electrode resistance increase originating from the polarization. At high voltage operating condition, rapid electrolyte decomposition and accumulation of a thick SEI layer at interface between the electrode and the electrolyte. The intrinsic reason of voltage decaying could be mitigated through enhance structural stability by designing material with increase homogeneity of atomic distribution and lattice substitution. Furthermore, the latter one, surface state dependent reason of voltage decaying can be significantly suppressed through stabilizing the interface between electrode and electrolyte by using proper electrolyte and surface modifications result in electrolyte stabilization. To stabilize the interface between electrode and electrolyte, surface coating with different type of inorganic[32] and organic materials such as metal-oxide: $Al_2O_3$[78,79], $TiO_2$[80] and $MnO_2$[81]; metal-fluoride: $AlF_3$[9, 28] metal-phosphate: Li-Ni-$PO_4$[82], $LiFePO_4$[83], Li-Mg-$PO_4$[84,85]; and polymer layer (polyimide[86] and polypyrrole[87]) have been used and effectively stabilize the electrode/electrolyte interface and improve the electrochemical performances of the Li-excess 3dTM cathode material.

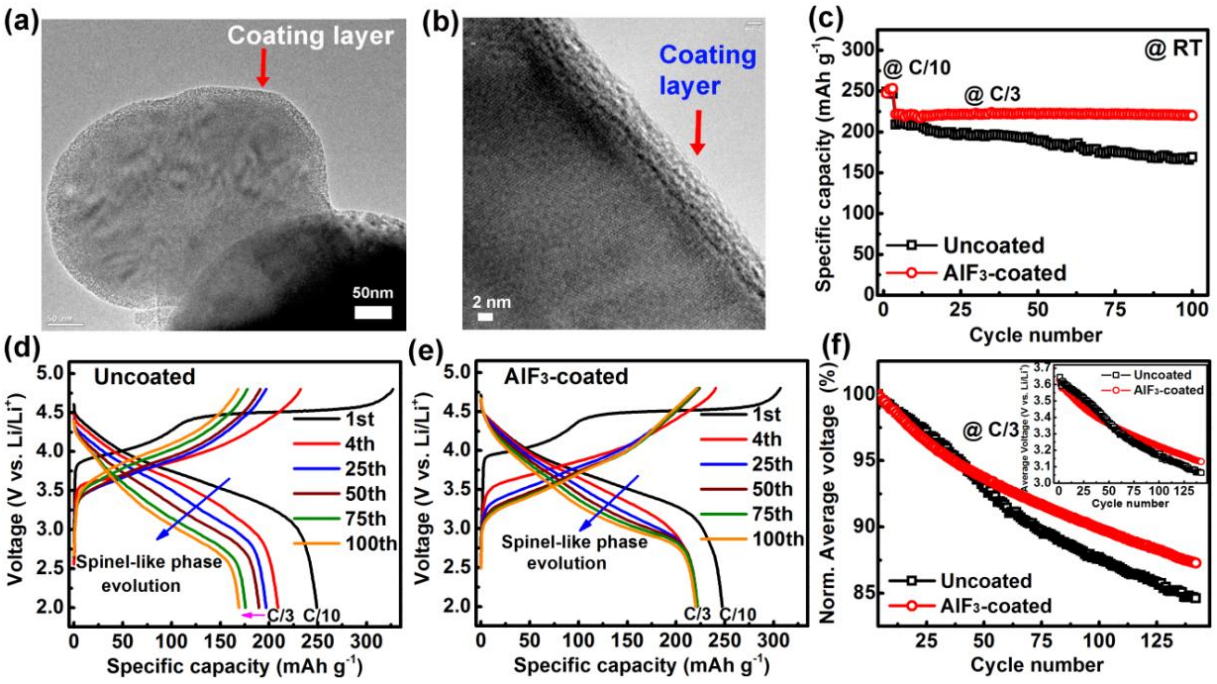


**Figure. 1-9** (a) HR-TEM image showing the $AlF_3$ coating on $Li_{1.2}Ni_{0.15}Co_{0.10}Mn_{0.55}O_2$ Li-excess 3dTM cathode material. (b) Magnified HR-TEM image showing the $AlF_3$ coating layer. (c) Cycling retention and corresponding voltage profile of (d) bare and (e) $AlF_3$-coated $Li_{1.2}Ni_{0.15}Co_{0.10}Mn_{0.55}O_2$ at C/3. (f) Normalized average discharge voltage of bare and $AlF_3$-coated $Li_{1.2}Ni_{0.15}Co_{0.10}Mn_{0.55}O_2$ materials; the inset shows the average discharge voltage value.[28]

$AlF_3$–coated $Li_{1.2}Ni_{0.15}Co_{0.10}Mn_{0.55}O_2$ Li-excess 3dTM cathode material and functioning mechanism were investigated by Zheng et al. in detail.[28] As a result, the amorphous $AlF_3$ coating layer, which is favorable for lithium ion diffusion, formed at cathode material surface (**Fig. 1-9a, b**). Due to the stabilized interfacial stability from the HF attack or electrolyte decomposition, the $AlF_3$-coated $Li_{1.2}Ni_{0.15}Co_{0.10}Mn_{0.55}O_2$ shows improved cycling retention. Also, $AlF_3$-coated $Li_{1.2}Ni_{0.15}Co_{0.10}Mn_{0.55}O_2$ shows mitigated voltage decaying compared during cycling to bare sample (**Fig. 1-9d, e**). Furthermore, the $AlF_3$-coated $Li_{1.2}Ni_{0.15}Co_{0.10}Mn_{0.55}O_2$ shows 10.1% decaying (=400 mV) compare to bare sample which shows 12.3% decaying (=470 mV) in average discharge voltage after 100 cycles. However, spinel-like phase is still observed on the surface. The stable surface coating layer alleviates or delays structural degradation by decreasing electrolyte decomposition and HF attack occurs at interface between material surface and electrolyte, but it could not completely eliminate this structural degradation. After surface $AlF_3$ coating modification, the structural stability cathode material surface exposed to electrolyte, the electrode/electrolyte interface are considerably stabilized, which blocks the electrolyte decomposition and guarantees the reversible $Li^+$ ion de-/re-intercalation processes in Li-excess 3dTM cathode material during cycling.

Liu et al. proposed a novel modification strategy to stabilize the $Li_{1.17}Ni_{0.17}Co_{0.17}Mn_{0.5}O_2$ surface with dual function surface protecting layer, which composed of $Mg^{2+}$ pillar effect at Li layer and $LiMgPO_4$ coating layer (**Fig. 1-10**).[84] The role of $Mg^{2+}$ pillar ion and Li-Mg-$PO_4$ layer is that prevent the irreversible structural degradation and suppresses the side reactions with electrolyte, respectively. Finally, these effects improves the interfacial stability, and consequent shows considerably improved cycling stability at 60 °C. (**Fig 1-10i**). Furthermore, 88.7% average discharge voltage retention also achieved, indicating that the structural degradation from layered to spinel-like phase resulting in voltage decaying phenomenon is unavoidable.

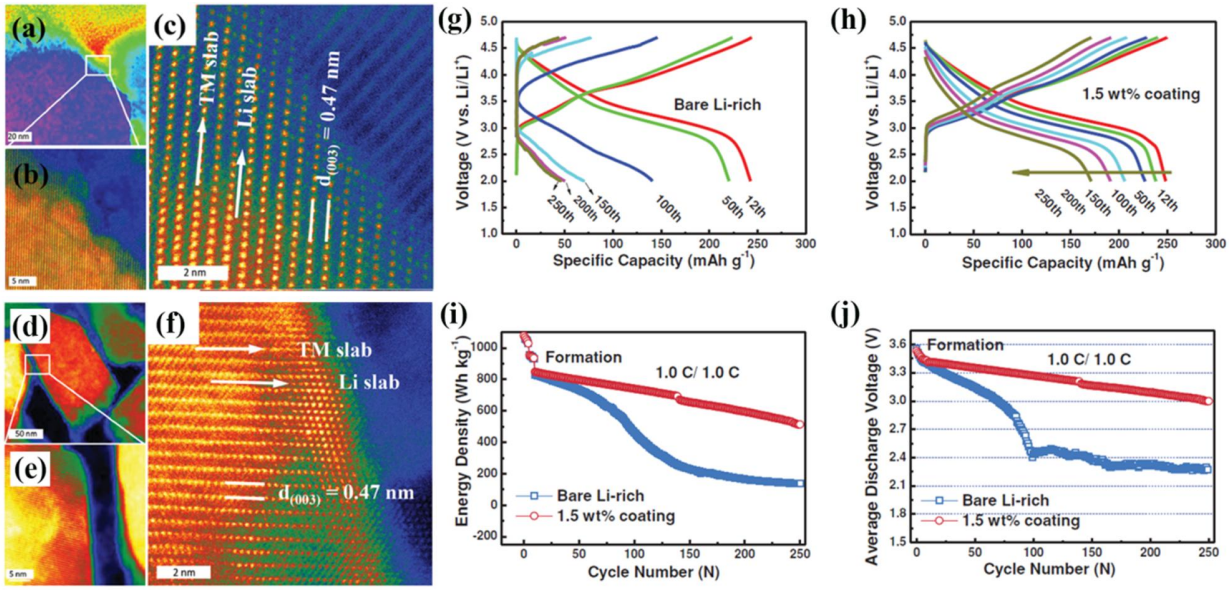


**Figure. 1-10** HAADF-STEM images of the (a-c) bare and (d-f) surface modified $Li_{1.17}Ni_{0.17}Co_{0.17}Mn_{0.5}O_2$ cathode material. The voltage profiles of the (g) bare and (h) surface modified $Li_{1.17}Ni_{0.17}Co_{0.17}Mn_{0.5}O_2$ at each cycle. (i) Energy density retention and (j) average discharge voltage retention of the bare and surface modified $Li_{1.17}Ni_{0.17}Co_{0.17}Mn_{0.5}O_2$ during cycling.[84]

### 1.3.4 Surface stabilization by suppressing the accumulation of SEI layer

Due to the operating of voltage of Li-excess 3dTM cathode material, over the 4.6-4.8 V to achieve the high reversible capacity over 250mAh/g, the electrolyte is decomposed by the generated active oxygen species through the activation of $Li_2MnO_3$ phase during high voltage charge process. The formation of passivation layer covers the entire cathode material surface and continuously increases the cell resistance. The increase of cell resistance during cycling accelerates the voltage decay of Li-excess 3dTM cathode material. Therefore, efficient electrolyte additives are critically important for stabilizing SEI layer on the cathode material surface and enhancing stability of interface between electrolyte and electrode. Many researchers have been proposed electrolyte additives to address the voltage fade issue of Li-excess 3dTM cathode material include borate,[88-90] phosphate,[91] nitrile-based,[92] ionic liquid,[93] and linear fluorinated carbonate.[94]

Zheng et al. proposed tris(pentafluorophenyl)borane (TPFPB) as an additional electrolyte additive to improve the cell resistance of $Li[Li_{0.2}Ni_{0.2}Mn_{0.6}]O_2$ by receipting the anion and mitigate voltage decaying during cycling.[28]. During the $Li_2MnO_3$ phase activation, oxygen is released from the lattice as highly reactive oxygen species (ROS) that readily oxidize the electrolyte.[95] Boron atom located in the center of TPFPB partially captured reactive oxygen species (ROS) instead of direct react with the electrolyte. As a result, by-products including LiF, $Li_2O_2$ and $Li_2O$.[96-99] derived from the side reaction between electrolyte and reactive oxygen species are substantially suppressed (**Fig. 1-11a**). The HR-TEM images shows that cycled $Li[Li_{0.2}Ni_{0.2}Mn_{0.6}]O_2$ in the electrolyte with the presence of TPFPB covered by a stable passivation layer with a thickness of 10-15 nm compared to cycled $Li[Li_{0.2}Ni_{0.2}Mn_{0.6}]O_2$ without TPFPB (**Fig. 1-11b**). Due to the stabilized interface between electrode and electrolyte, long-term cycling stability is significantly improved with addition of TPFPB. Furthermore, electrolytes with 0.1 M and 0.2 M TPFPB achieved 74.2 % and 76.8 % capacity retentions after 500 cycles for cathodes, respectively, much higher than reference electrolyte (33.5 %). Additionally, TPFPB additive also mitigated the voltage decaying during cycling because the accumulation of passivation film is reduced and the stabilized interfacial resistance (**Fig. 1-11d, e**).

Li et al. proposed tris(trimethylsilyl)borate (TMSB) as an additional electrolyte additive to improve the cell resistance of $Li_{1.2}Mn_{0.54}Ni_{0.13}Co_{0.13}O_2$ in electrolyte.[88] In article, by adding only 0.5 wt % of TMSB the cyclic stability of the $Li_{1.2}Mn_{0.54}Ni_{0.13}Co_{0.13}O_2$were significantly improved during cycling due to the improvement in interfacial stability between electrolyte and $Li[Li_{0.2}Mn_{0.54}Ni_{0.13}Co_{0.13}]O_2$ material surface. TMSB preferentially oxidizes and forms a protective SEI layer which protects $Li_{1.2}Mn_{0.54}Ni_{0.13}Co_{0.13}O_2$ from structure destruction instead of by-product generation derived from electrolyte decomposition (**Fig. 1-12**).

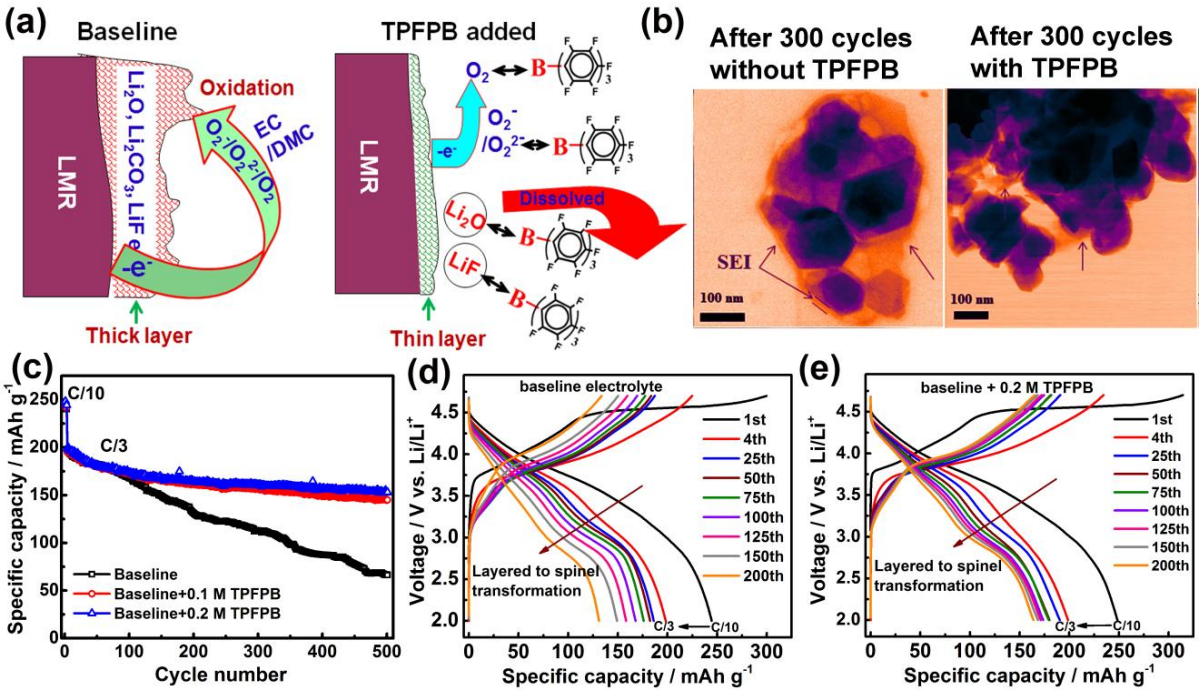


**Figure. 1-11** (a) Schematic view of the functioning mechanism of TPFPB. (b) TEM images of $Li[Li_{0.2}Ni_{0.2}Mn_{0.6}]O_2$ electrodes cycled in electrolytes without and with TPFPB additive after 300 cycles. (c) Cycling retention and voltage profile of $Li[Li_{0.2}Ni_{0.2}Mn_{0.6}]O_2$ cycled in electrolytes (d) without and (e) with TPFPB additive.[28]

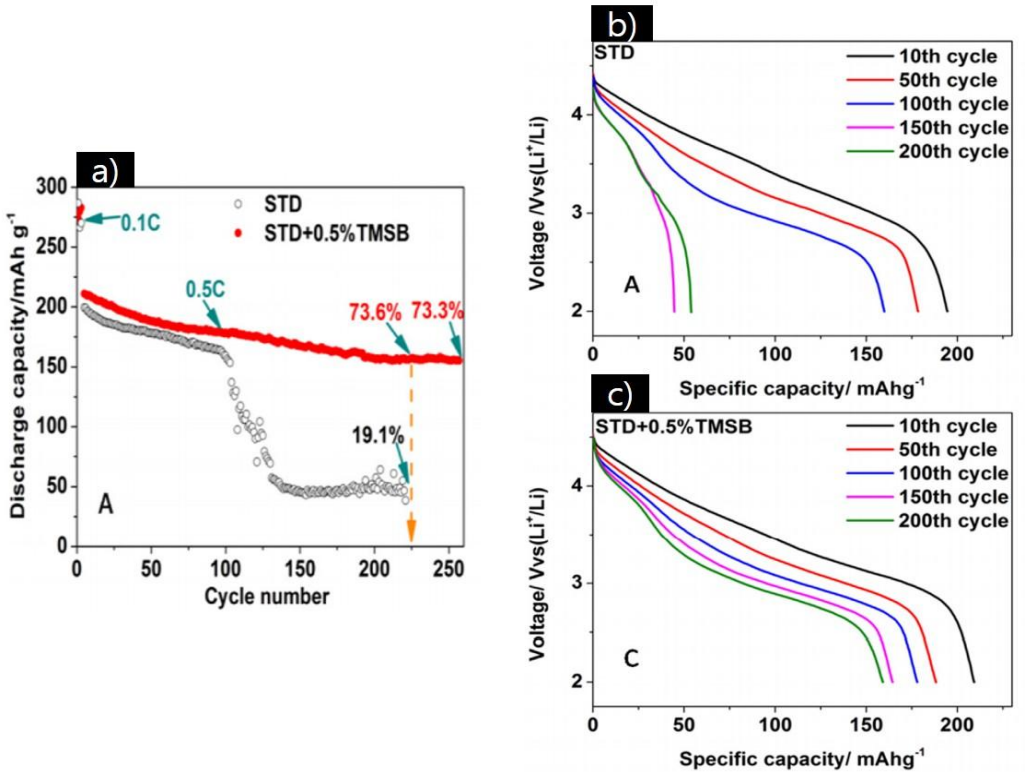


**Figure. 1-12** (a) Cycling retention and voltage profiles of $Li_{1.2}Mn_{0.54}Ni_{0.13}Co_{0.13}O_2$ cathode material cycled in electrolyte (b) without and (c) with TMSB.[88]

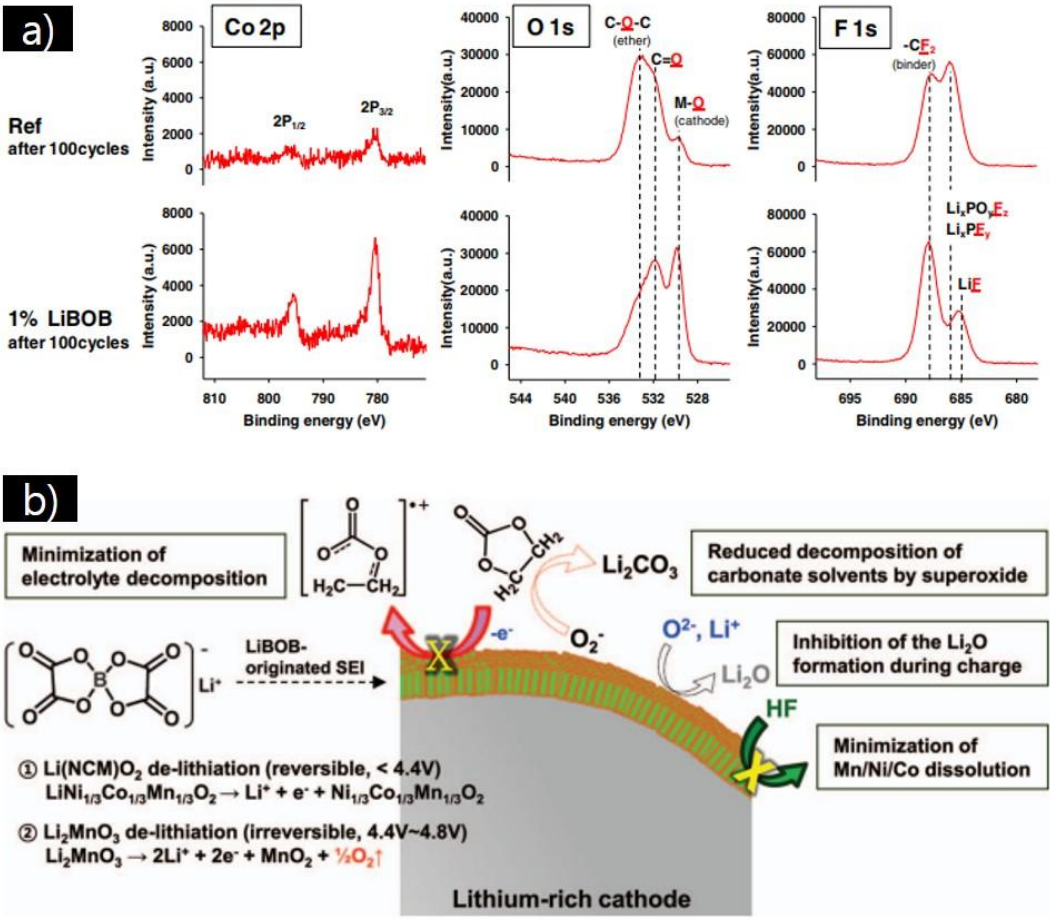


**Figure. 1-13** (a) Co2p, O1s, and F1s XPS spectra of 100th cycled $Li_{1.17}Ni_{0.17}Mn_{0.5}Co_{0.17}O_2$ material in the electrolyte with and without 1% of LiBOB. (b) Schematic view of functioning mechanism of LiBOB during cycling.[89]

The effect of the lithium bis(oxalato) borate (LiBOB) additive on the electrochemical performance of $Li_{1.17}Ni_{0.17}Mn_{0.5}Co_{0.17}O_2$ were studied by Choi et al (**Fig. 1-13**).[89] According to their SEM and XPS result, the thicker and unstable surface film were observed on $Li_{1.17}Ni_{0.17}Mn_{0.5}Co_{0.17}O_2$ electrode surface cycled in reference electrolyte. However, $Li_{1.17}Ni_{0.17}Mn_{0.5}Co_{0.17}O_2$ electrode surface cycled in LiBOB-added electrolyte shows thin surface film, indicating suppressed electrolyte decomposition. Therefore, enhanced rate performance and mitigated voltage decaying were achieved by $Li_{1.17}Ni_{0.17}Mn_{0.5}Co_{0.17}O_2$ electrode cycling with LiBOB-added electrolyte. Furthermore, Nayak et al. studied the additional effects of LIBOB additive on the structural evolution of $Li_{1.2}Ni_{0.16}Mn_{0.56}Co_{0.08}O_2$.[90] Despite the achievement of surface stabilization, discharge voltage profile decay still occur originating from the intrinsic phase transformation.

## 1.4 Scope and organization of this dissertation

The objective of this dissertation is the study of voltage decay in Li-excess 3d-transition-metal layered oxide.

The chapters are categorized as follows:

**Chapter 2** $Al(OH)_3$ Nanosheet Coating with complete coverage on Li-rich Cathode Materials via chemical Control of Coating Process.

**Chapter 3** Understanding of voltage decay in Li-excess layered cathode materials through oxygen-centred structural arrangement.

# Chapter 2

# $Al(OH)_3$ Nanosheet Coating with Complete Coverage on Li-rich Cathode Materials *via* Chemical Control of Coating Process

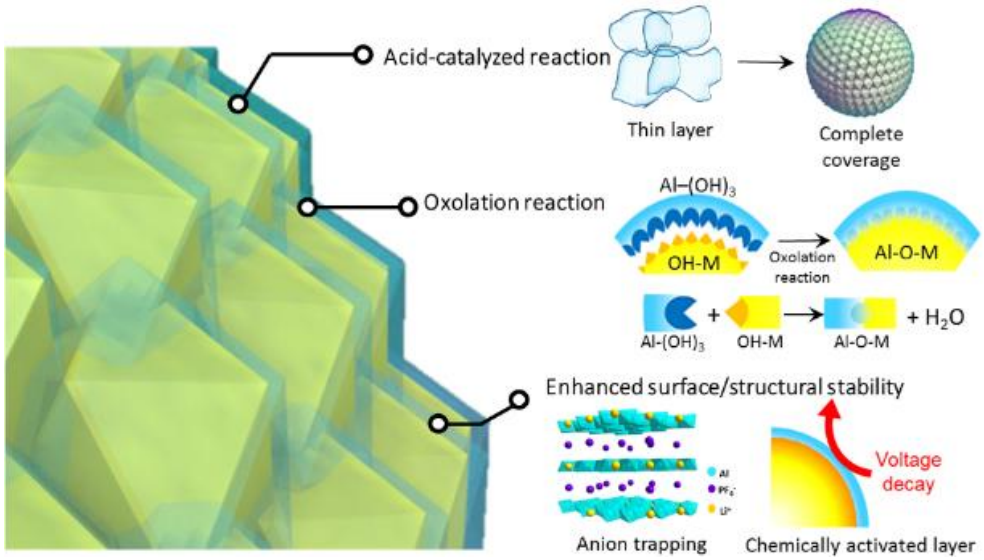


Li-rich layered oxide materials with high discharge capacities are promising positive electrode materials for high energy Li-ion batteries. However, they are facing some problems, such as surface instability issue, dramatic capacity drop at high temperature, voltage decay and poor power capabilities. In this study, we report a novel $Al(OH)_3$ nanosheet coating concept on $Li_{1.12}[Ni_{0.2}Co_{0.2}Mn_{0.6}]_{0.88}O_2$ through a delicately planned coating chemistry yielding a fully enveloping coating morphology with controlled thickness of 4 nm. This layer inhibits the continuous degradation mechanism, and retains surface structure by trapping $PF_6^-$ anions and protecting the surface from unstable side reactions. As a result, surface treated materials showed superior voltage retention as well as improved cycle/rate performances compared to conventional coating methods, both at 25 °C and 60 °C. This chemical engineering concept for new coating morphology enhances electrochemical performances of Li-rich materials, and opens a new prospect in the surface coating researches for all cathode materials.

**This chapter has not been published.**

## 2.1 Introduction

Nowadays, LIBs are being asked not only to succeed in the small battery fields, but also to behave as the large energy storage facility, which can be applied to electric vehicle (EV) and energy storage system (ESS). Following this trend, Li-/Mn-rich materials are drawing much attention as one of the most promising cathode materials for next generation LIBs,[100-104] due to their high reversible capacity and low price. However, these materials suffer from surface degradation, such as oxygen evolution from the surface,[105-107] and side reactions with electrolytes driven by the unstable electrochemical reaction of the $Li_2MnO_3$ phase activation process,[108, 109] and high voltage charge processes. Such surface deteriorations cause the accumulation of by-products,[8] metal dissolution into the electrolyte,[110, 111] electrolyte depletion,[112] and continuous structural collapse,[113-118] resulting in degradation of electrochemical properties. Furthermore, these problems not only remain as 'problems at the surface', but also propagate into the bulk part of the particles and cause structural deteriorations in the end. Therefore, many researches tried to protect the active materials' surface with stable coating layers, such as metal oxide and phosphate compounds, in order to avoid direct contact with corrosive electrolyte and resulting deterioration.[119-124]

In the past decade, numerous studies have focused on the surface modification, and they have shown many noticeable improvements on the cathode material fields, however, there were some limitations for these previous coating methods. [119-124] First, there were definite morphological weaknesses, such as restricted cover area and too thick coating layer thickness, which came from colloidal-shaped coating materials (**Fig. 2-1**). This island-type coating morphology leads to partial protection of the surface, irregular coating layer, and finally cause loss of stability at uncovered area during repeating electrochemical charge and discharge processes. Second, conventional coating materials only could act as a physical barrier against corrosive electrolyte and delay surface deterioration, but could not solve fundamental problems of side reactions, lithium salt $PF_6^-$ decomposition and following HF generation. Therefore, for previous coating approaches, it is not easy to endure long electrochemical cycles and severe conditions for electrolytes, such as high working temperature ($\geq 60°C$). Accordingly, for an ideal coating effect, not only morphological advances in both coverage and proper thickness of coating layers are needed, but also fundamental solution for continuous HF generation and side reactions are required.

Herein, we propose a complete coating concept, namely $Al(OH)_3$ nanosheet coating on $Li_{1.12}[Ni_{0.2}Co_{0.2}Mn_{0.6}]_{0.88}O_2$, making use of chemical control of coating process. Thanks to initial nanosheet morphology of $Al(OH)_3$ coating material and oxolation reaction between $OH^-$ functional group on active materials' surface and $Al(OH)_3$ coating material, these concurrent chemical reactions are so spontaneous and global that they enable the uniform 4 nm of nanosheet coating material to cover the Li-rich material completely. Furthermore, $Al(OH)_3$ coating layer can trap highly reactive $PF_6^-$ anion during the electrochemical cycle and stabilize electrolyte-active material interface, contrary to previously developed

coating materials that only could prevent direct contact between electrolyte and surface of active material. This surface stabilization induced by a systematic surface engineering leads to superior electrochemical properties, such as improved cycle/voltage retention at high temperature of 60°C compared to pristine and conventional $Al_2O_3$-coated cathodes.

## 2.2 Experimental detail

***Synthesis of CC-LNMC.*** 10 wt% Aluminum nitrate nonahydrate (ACS reagent, ≥98%, Aldrich) was dissolved in distilled water. The pre-prepared $Li_{1.12}[Ni_{0.2}Co_{0.2}Mn_{0.6}]_{0.88}O_2$ powders (Samsung Fine Chemicals Co. Ltd.) were then immersed in the aluminum nitrate nonahydrate solution at 25 °C, and 0.2 wt% of hydrazine monohydrate solution (reagent grade, $N_2H_4$ 50-60%, aldrich) was added as a precipitation agent, which causes an irreversible deprotonation reaction and subsequent hydrolysis/condensation with aluminum. The solution containing the resulting cathode material was stirred continuously at 90 °C for 1 h. The resulting material (denoted as CC-LNMC) was filtered, washed with distilled water, and dried overnight at 110 °C.

***Synthesis of PC-LNMC***. 10 wt% Aluminum nitrate nonahydrate (ACS reagent, ≥98%, Aldrich) was dissolved in distilled water. The pre-prepared $Li_{1.12}[Ni_{0.2}Co_{0.2}Mn_{0.6}]_{0.88}O_2$ powders were immersed in the aluminum nitrate nonahydrate solution at 25 °C, and ammonium hydroxide solution (ACS reagent, 28.0 - 30.0% $NH_3$ basis, Aldrich) was added slowly until PH = 7. The resulting material was filtered, washed with distilled water and annealed at 400 °C for 4 h in air.

***Structural characterization.*** To investigate differences in the crystalline phases of the samples, powder X-ray diffraction (XRD, D/MAX 2500V/PC) was carried out using CuKα radiation. The surface morphologies of the samples were observed by scanning electron microscopy (SEM, JSM 6400, JEOL) and Titan3 G2 60-300 microscope. A field-emission electron microscope (JEM-2100F, JEOL) was used to identify differences in the surface phases of pristine and $Al(OH)_3$-coated cathodes at atomic resolution.

***Electrochemical characterization.*** For preparation of the cathode, the pre-prepared powders were mixed with carbon black and polyvinylidene fluoride (8:1:1) in N-methylpyrrolidinone. The resulting slurry was cast onto Al foil with the active material loaded at 4.5 - 5.0 mg $cm^{-2}$, and the mixture roll-pressed. The electrodes were dried overnight at 110 °C in a dry oven. The electrochemical performances of the prepared pristine and CC-LNMC $Li_{1.12}[Ni_{0.2}Co_{0.2}Mn_{0.6}]_{0.88}O_2$ were measured in tests using 2032R coin-type cells, and used about 0.5 mL electrolytes for the test. The coin cells were assembled with Li metal as the counter and reference electrodes, and five identical cells were tested at the same time to ensure the data reliability per sample. A polypropylene separator (Celgard) was used in these studies, along with an electrolyte, which was composed of a solution of 1.3 M $LiPF_6$ in ethylene carbonate (EC)/diethyl carbonate (DEC) (3:7 vol%) with 10 wt% fluoroethylene carbonate (FEC) (Panatech, Korea). The galvanostatic charge-discharge cycle was carried out between 2.0 and 4.6 V (vs. $Li/Li^+$) at different C-rates, at temperatures of 25 °C and 60 °C. To obtain accurate data, 4 cells per sample were tested. Electrochemical impedance spectroscope (EIS) was performed in the 0.001-100 kHz frequency range using an electrochemical interface system (IVIUM) on 100 cycled coin-type half-cells at 4.3 V.

## 2.3 Results and discussion

**Chemistry of coating process.** Most of previous coating researches utilized sol-gel method and high-temperature heat treatment to synthesize coating layers.[119-124] In case of conventional sol-gel method,

nucleation process takes place under high-pH condition, so condensation process takes priority and colloidal-shaped coating materials are formed.[125] Furthermore, high-temperature heat treatment on colloidal-shaped coating material leads to typical island-type coating morphology with confined protection effect (**Fig. 2-1**).

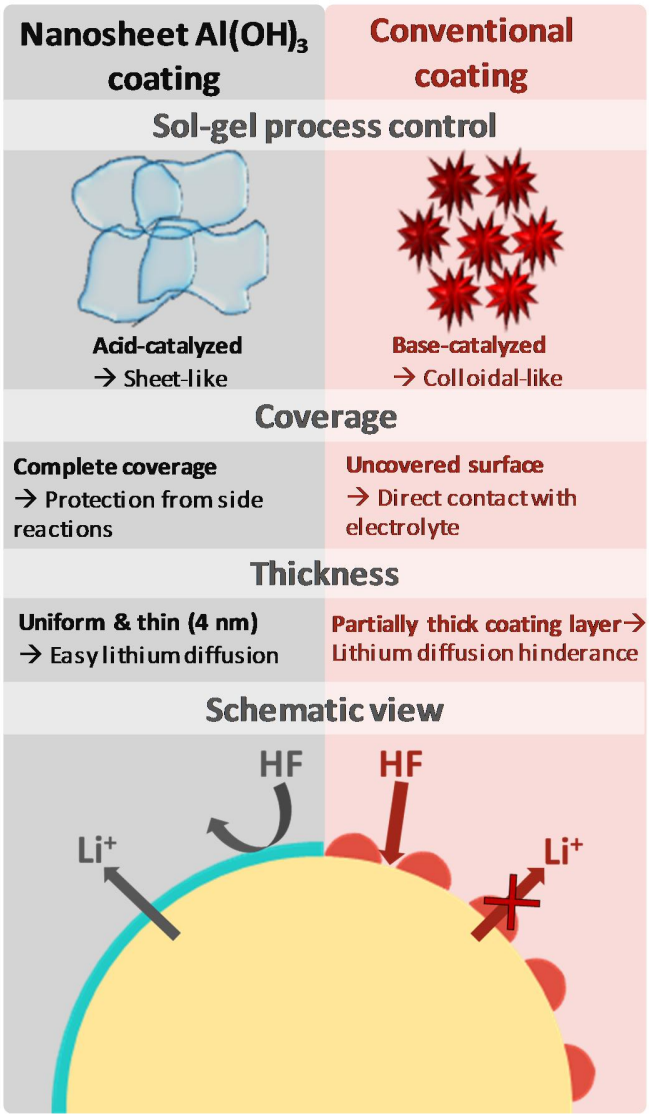


**Figure 2-1.** Morphology comparison between nanosheet $Al(OH)_3$ coating and conventional coating.

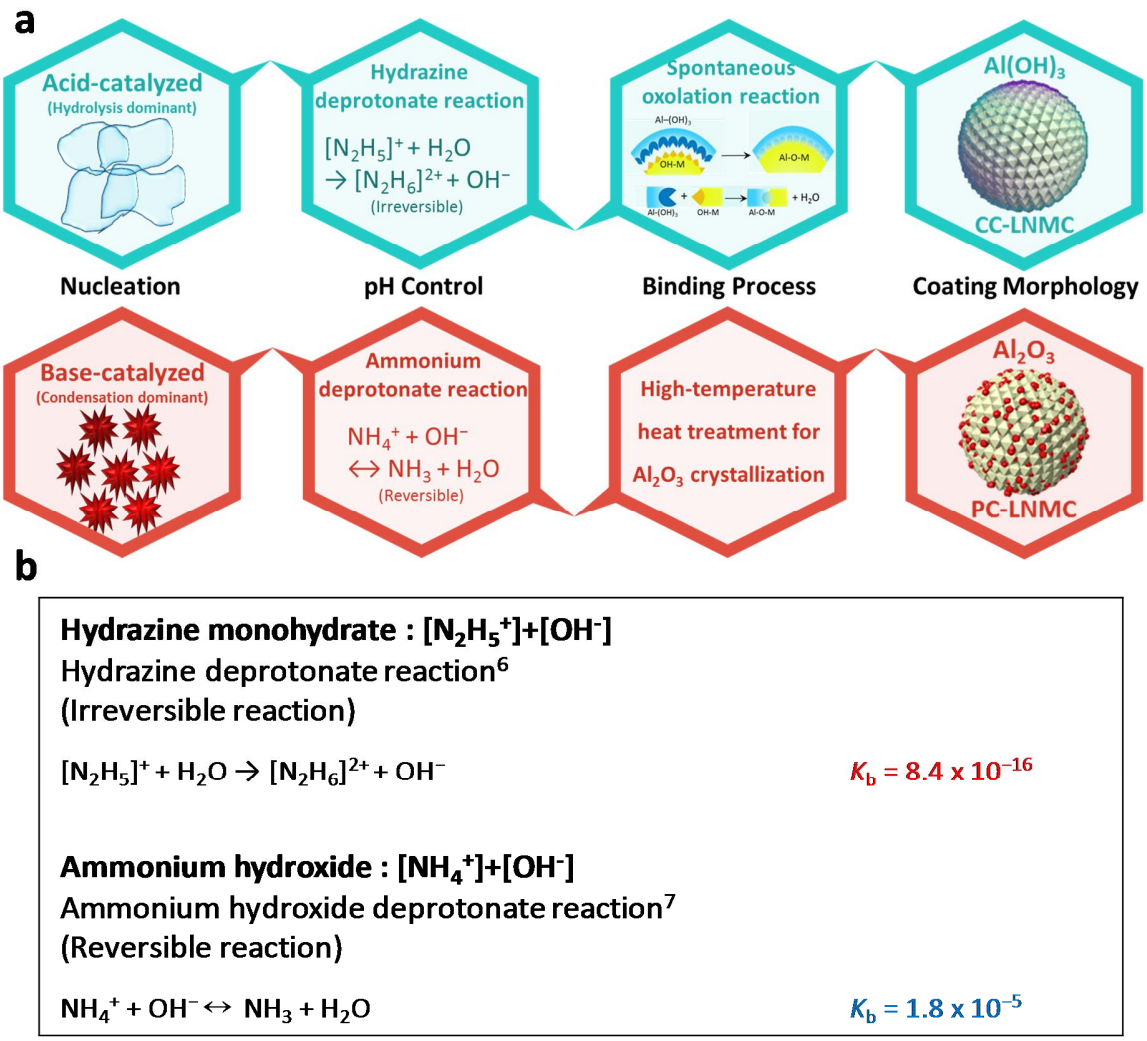


**Figure 2-2.** (a) Coating process comparison between CC-LNMC and PC-LNMC. (b) Deprotonate reactions of hydrazine monohydrate and ammonium hydroxide.

In this study, we designed a new coating morphology by controlling the sol-gel nucleation process and binding process between coating material and active material with deeper understanding about coating chemistry (**Fig. 2-2a**). Firstly, sol-gel process was controlled by replacing $OH^-$ donor ammonium hydroxide with hydrazine monohydrate. Due to an irreversible deprotonate reaction of hydrazine monohydrate (**Fig. 2-2b**), pH could remain acidic condition and resulted in formation of nanosheet-like polymeric gel $Al(OH)_3$ (**Fig. 2-3a**) coating material. [125] Secondly, synthesized coating material undergoes a dehydration reaction with hydroxyl groups at the surface of the active material and form an oxo-bridge. This reaction, also known as oxolation reaction, could be globally and favorably occurred due to sufficient quantity of hydroxyl groups at the surface of the active material[126-128] and thermodynamic preference.[129, 130] For these reasons, an ideal coating morphology, a combination of high surface coverage area, and nanoscale thickness of the coating layer could be achieved as the result of the coating chemistry control (**Fig. 2-1**).

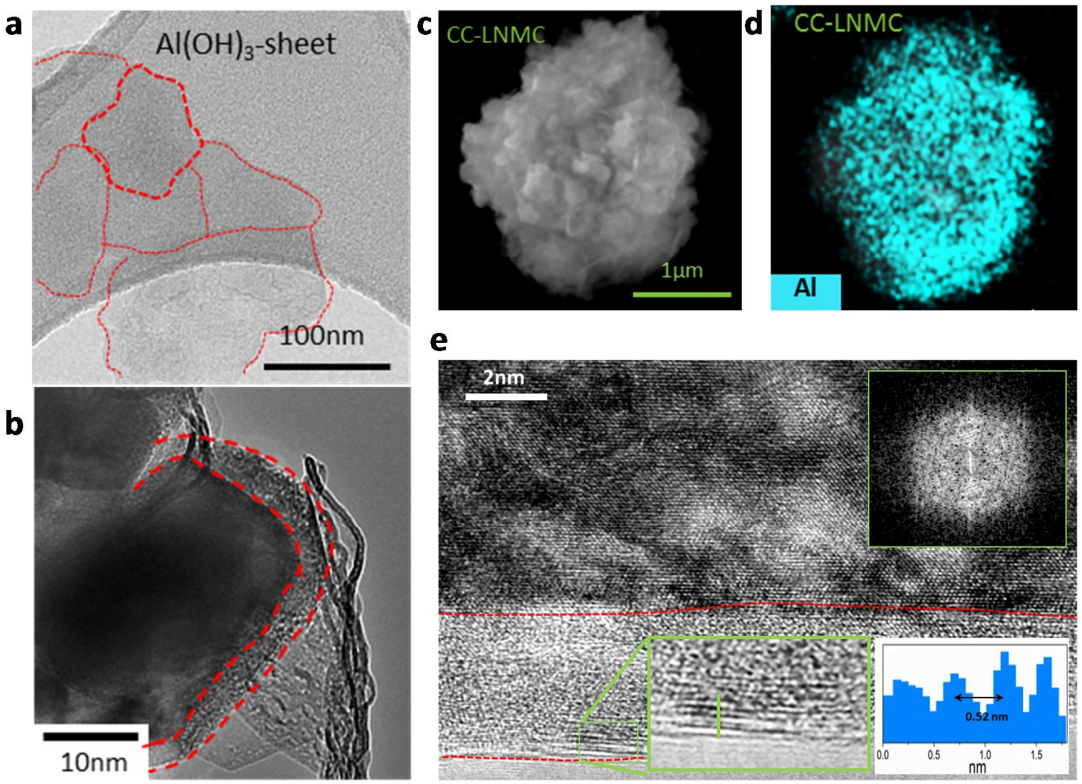


**Figure 2-3.** Coating morphology of CC-LNMC and PC-LNMC. (a) As-synthesized $Al(OH)_3$ nanosheets. (b) TEM image showing complete coverage of $Al(OH)_3$ coating layer on the surface of pristine material. (c) SEM image of CC-LNMC. (d) SEM-EDS mapping image that shows homogeneous aluminum dispersion on the surface of CC-LNMC. (e) TEM image of CC-LNMC. (The upper inset shows FFT pattern of amorphous coating layer, and the lower one shows interlayer distance of $Al(OH)_3$ coating layer.)

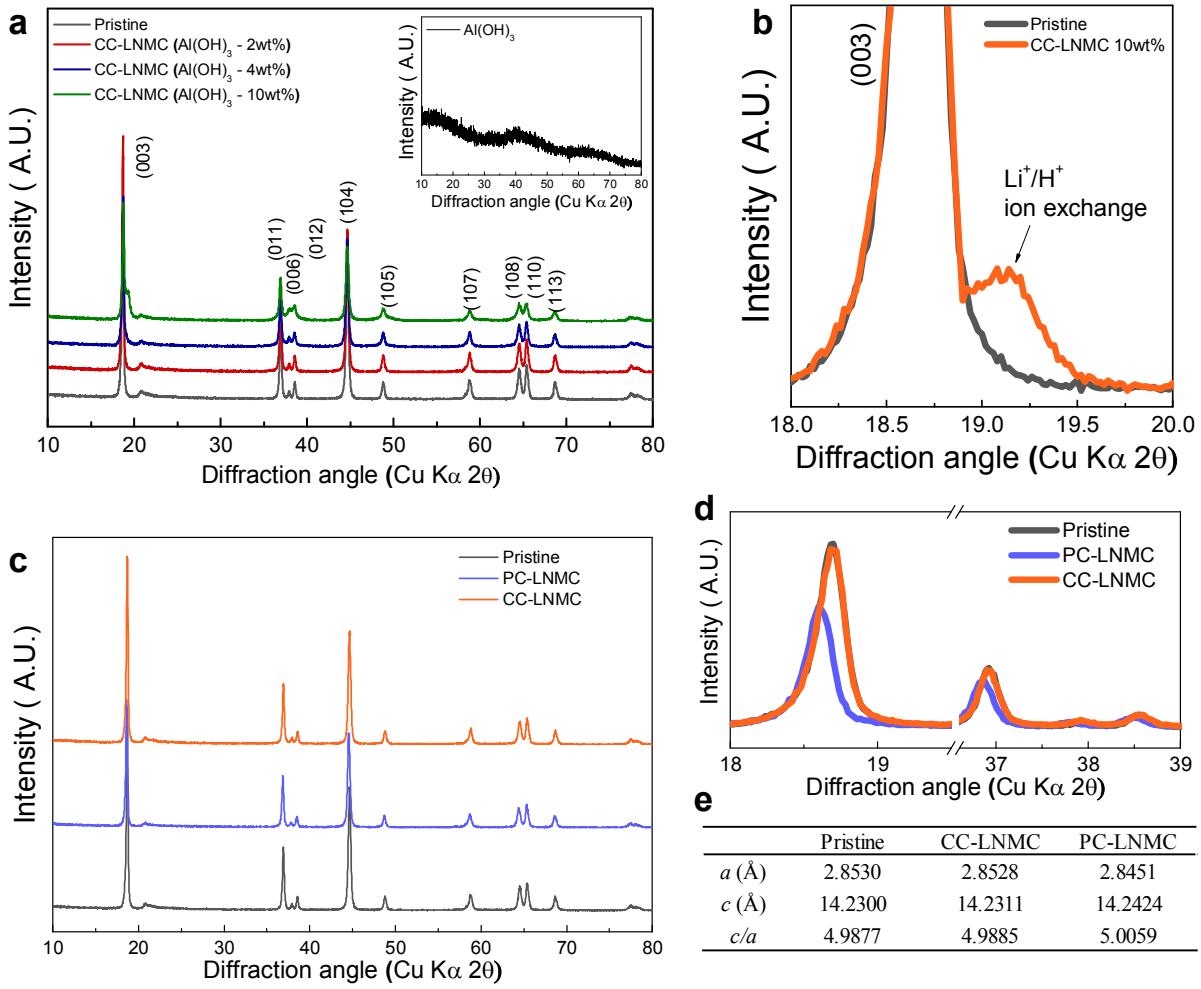


| | Pristine | CC-LNMC | PC-LNMC |
|---|---|---|---|
| *a* (Å) | 2.8530 | 2.8528 | 2.8451 |
| *c* (Å) | 14.2300 | 14.2311 | 14.2424 |
| *c*/*a* | 4.9877 | 4.9885 | 5.0059 |

**Figure 2-4.** Structural analysis *via* X-ray diffraction patterns. (a) Change of XRD patterns according to different amount of $Al(OH)_3$ coating material. (b) Appearance of $HCrO_2$ peak in case of excessive amount of $Al(OH)_3$ coating. (c-e) XRD patterns of pristine, PC-LNMC, and CC-LNMC.

**Morphological Characterization.** Comparison for XRD patterns of pristine material and coated material are shown in **Fig. 2-4**, and there is no significant change, such as peak shift or appearance of impurity peaks. When we put an excess amount of coating material (10 wt%), a new peak is appeared right next to (0 0 3)$_{hexagonal}$ peak (**Fig. 2-4b**). This peak is identified as $HCrO_2$ peak,[1] and this structure is came from $Li^+/H^+$ ion exchange, which is caused by hydrazine added as precipitation agent. From this result, it is expected that chemically activated phase is formed near the surface after $Al(OH)_3$ coating. In order to prove coating coverage and uniformity, morphological characterization with scanning electron microscope (SEM) and transmission electron microscope (TEM) was carried out on pristine and two kinds of coated samples ($Al(OH)_3$ and $Al_2O_3$). **Fig. 2-3c** and **Fig. 2-5c** show the scanning electron micrographs of the $Al(OH)_3$-coated and $Al_2O_3$-coated samples (denoted as CC-LNMC and PC-LNMC) prepared by the acid-catalyzed reaction and base-catalyzed reaction, respectively. Pristine, 4 μm-sized secondary particles composed of primary particles with diameters in the range of 50-100 nm, shows an uneven surface morphology (**Fig. 2-5a**). After the coating process, a transparent $Al(OH)_3$ layer covers the surface of pristine completely, giving a smooth surface morphology. Moreover, sheet-like $Al(OH)_3$ homogeneously and completely coated majority of pristine particles as shown in **Fig. 2-3b**. **Figure. 2-3d** and **Fig. 2-5d** shows scanning electron microscopy-energy dispersive X-ray spectroscopy (SEM-EDS) mapping images of the CC-LNMC and PC-LNMC particles. While both samples show the same Al content of 0.66 wt% (**Fig. 2-6**), CC-LNMC displayed uniform aluminum dispersion of completely covered $Al(OH)_3$ coating layer, contrasting with the typical island-type coating morphology of PC-LNMC.

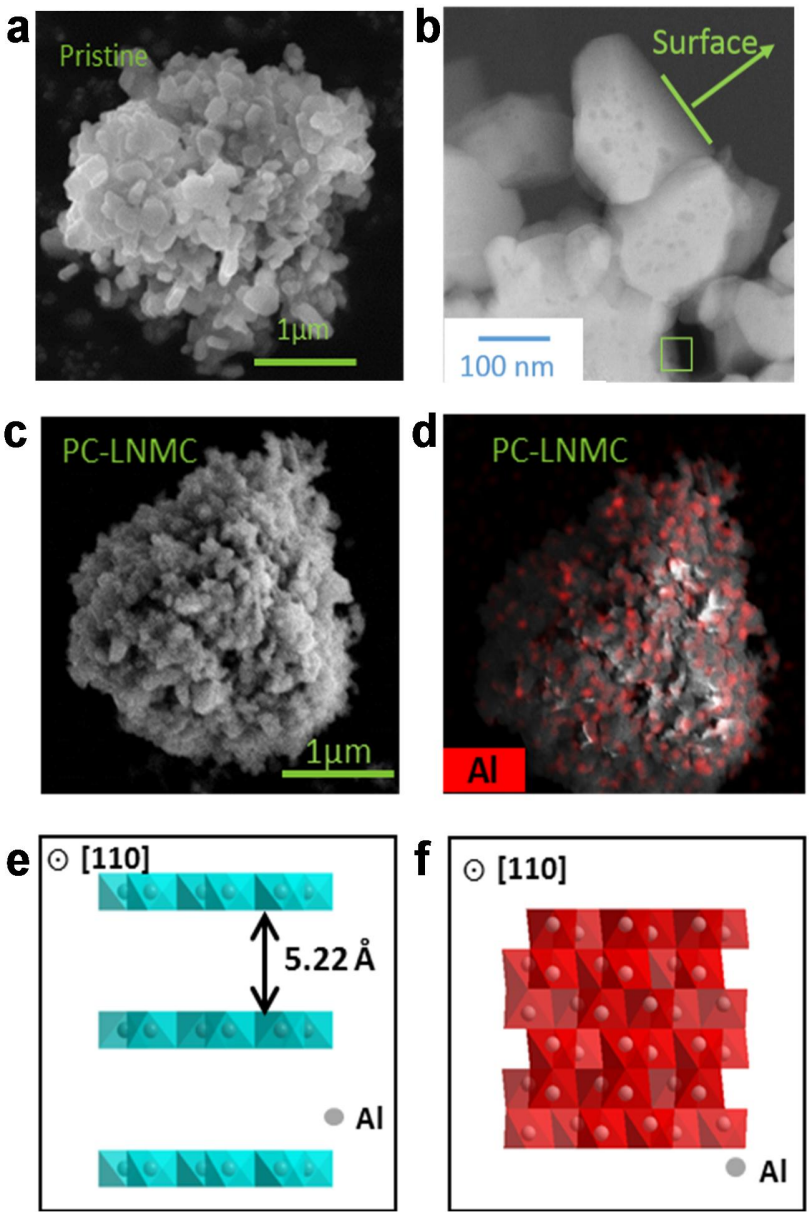


**Figure 2-5.** Morphology comparison for pristine, CC-LNMC, and PC-LNMC. SEM images of (a) Pristine, (b) CC-LNMC, and (c) PC-LNMC. (d) SEM-EDS mapping image of PC-LNMC. (e,f) Simulated structure of $Al(OH)_3$ and $Al_2O_3$ coating material, respectively.

| Samples | Al wt% |
|---|---|
| Pristine | 0 |
| PC-LNMC | 0.66 |
| CC-LNMC | 0.66 |

**Figure. 2-6.** Inductively coupled plasma-atomic emission spectroscopy (ICP-AES) data of pristine, PC-LNMC, and CC-LNMC. ICP data shows the same amount of Al (0.66 wt%) was used for both $Al_2O_3$ and $Al(OH)_3$ coating.

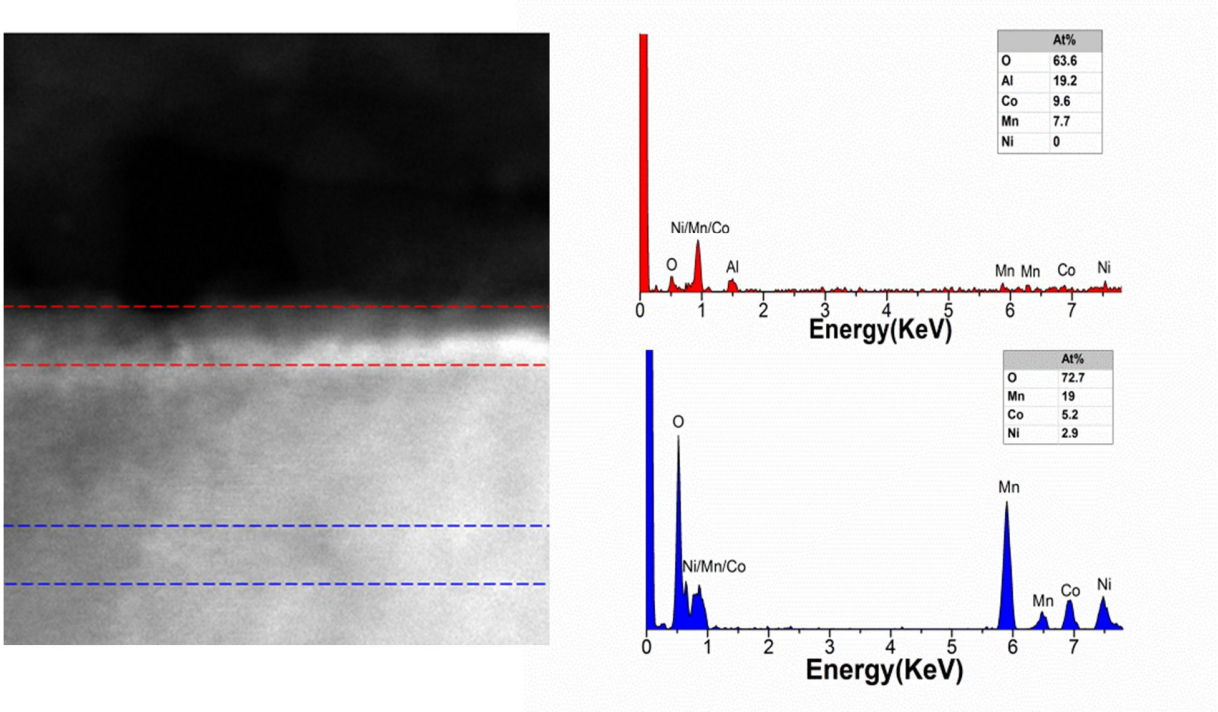


**Figure. 2-7.** Chemical composition analysis with HRTEM-EDS.

**Figure 2-3e** shows high-resolution transmission electron microscopy (HRTEM) image of CC-LNMC. The transparent sheet-like $Al(OH)_3$ coated the surface of $Li_{1.12}(Ni_{0.2}Co_{0.2}Mn_{0.6})_{0.88}O_2$ particles with uniform layer of approximately 4 nm thickness. The coating layer represented by a red dashed line in **Fig. 2-3e** shows the short-range order of the $Al(OH)_3$ layer, displaying amorphous FFT patterns (the upper inset of **Fig. 2-3e**). In addition, interlayer distance of $Al(OH)_3$ coating material was confirmed as 0.52 nm, which is similar to simulated interlayer distance between layers of γ-$Al(OH)_3$ (**Fig. 2-4e**). Morphology of $Al(OH)_3$ coating layer was confirmed by means of SEM, TEM and EDS. Sheet-like $Al(OH)_3$ layer was successfully covered the whole surface of the Li-rich material, and this is considered as ideal morphology for conventional coating methods preventing direct contact between electrolyte and active material (**Fig. 2-7**). HRTEM-EDS analysis for both surface layer and bulk part of a primary particle determined the atomic percentages of aluminum and oxygen. At the surface layer, atomic percentage of Al and O is 19.2 At% and 63.6 At%, respectively. This is corresponds with the theoretical atomic ratio of $Al(OH)_3$ (Al/O = 1:3), however, aluminum was not found at bulk part of a primary particle. Thus, HRTEM-EDS result supporting the assumption that a sheet-like $Al(OH)_3$ layer formed as a coating on the Li-rich surface.

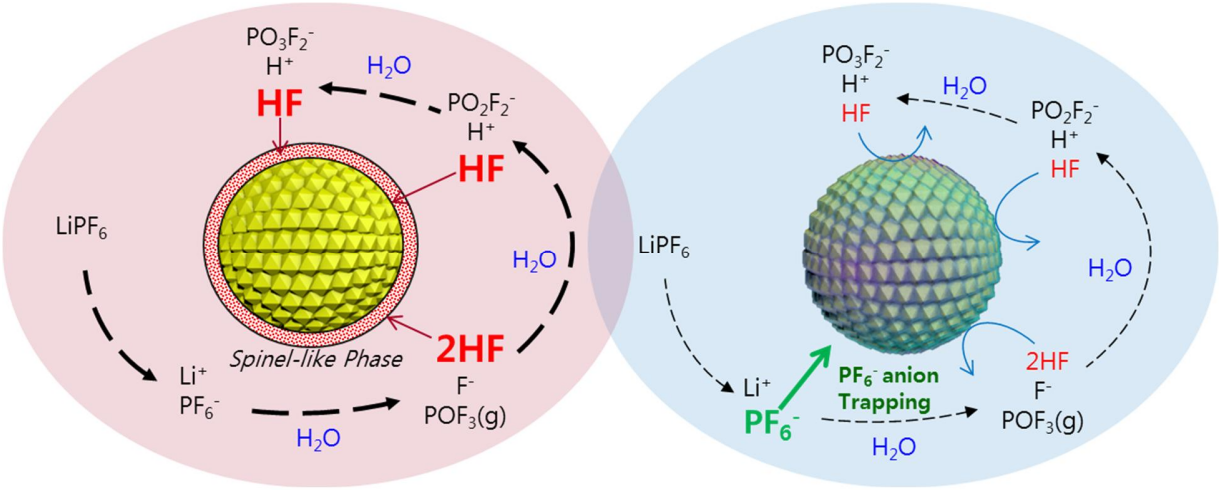


**HF generation reaction**

$PF_6^- + H_2O \leftrightarrow F^- + POF_3 + 2HF$ (1)

$POF_3 + H_2O \leftrightarrow PO_2F^{2-} + HF + H^+$ (2)

$POF_3 + ne^- + nLi^+ \rightarrow LiF + Li_xPO_yF_z$ (3)

$PO_2F^{2-} + H_2O \leftrightarrow PO_3F^{2-} + HF + H^+$ (4)

**Figure 2-8.** HF generation mechanism in lithium ion battery and anion trapping mechanism of $Al(OH)_3$ coating layer.

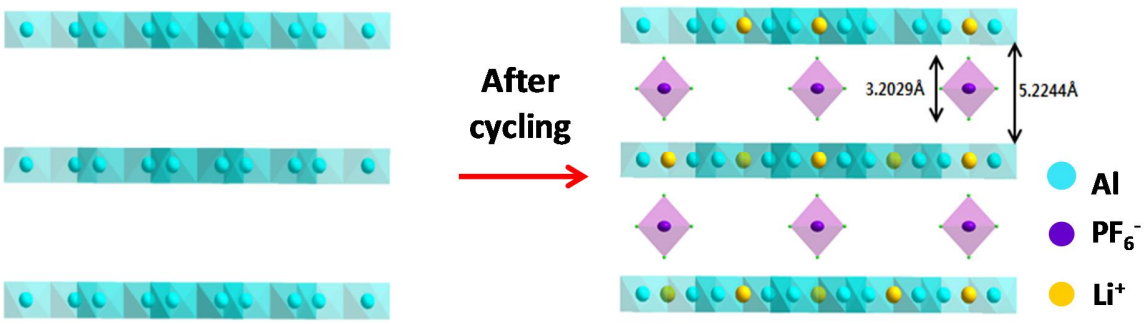


**Figure 2-9.** Schematic view for anion trapping mechanism of $Al(OH)_3$ coating layer.

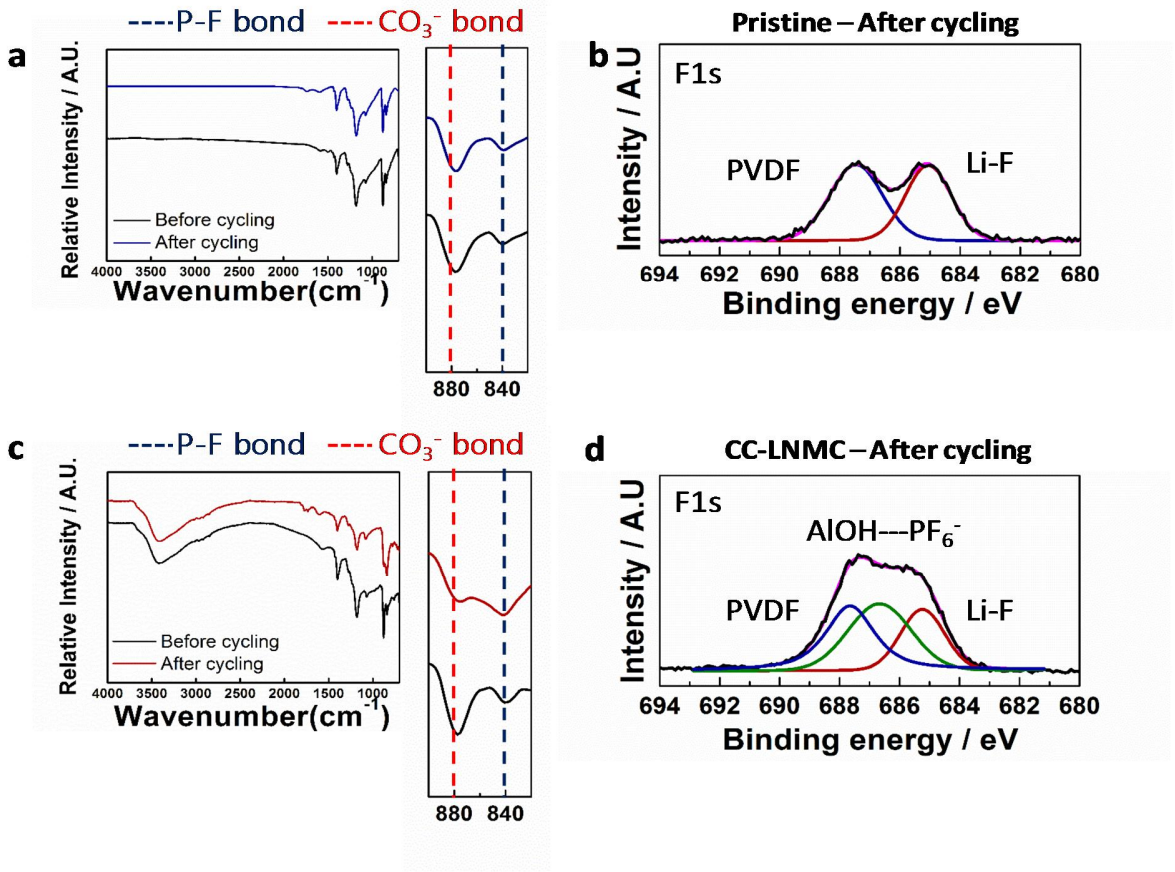


**Figure 2-10.** Anion trapping mechanism of $Al(OH)_3$ coating layer. (a) FTIR-ATR analysis of pristine, before and after cycling. (b) XPS analysis for F1s of CC-LNMC after cycling. (c) FTIR-ATR analysis of pristine, before and after cycling. (d) XPS analysis for F1s of CC-LNMC after cycling.

**Role of the $Al(OH)_3$ coating layer.** This newly developed coating layer is designed to have another functionality as well as ideal coating morphology. $Al(OH)_3$ has been reported to have a special property, trapping of the $PF_6^-$ anion between layers of hydroxide groups. Interestingly, thanks to the large size of empty 2a-site (5.22 Å diameter) between the Al layers, it was proposed that the $PF_6^-$ anions (3.20 Å diameter)[131] dissociated from the $LiPF_6$ salt (**Fig. 2-8**) could be trapped in the 2a-sites. Then, free $Li^+$ ions could locate in octahedral holes of the Al layer for charge neutrality (**Fig. 2-9**). In order to confirm the $PF_6^-$ trapping hypothesis, *ex-situ* Fourier transform infrared spectroscopy-attenuated total reflectance (FTIR-ATR) mode analysis (**Fig. 2-10a, c**) and X-ray photoelectron spectroscopy (XPS) were performed on electrodes after 20 cycles (**Fig. 2-10b, d**). Absorption characteristics of PVDF binder (1400, 1271, 1170, 1070, 877, and 840 $cm^{-1}$) are dominantly observed the spectra in all samples, as a result of FTIR-ATR

analysis. Comparison with previous studies confirmed that the peaks in the FTIR spectra at 3430 $cm^{-1}$ and 842 $cm^{-1}$ correspond to the IR-active modes of O-H and $PF_6^-$ respectively.[132] For pristine sample, no signal was observed at 3430 $cm^{-1}$, and 842 $cm^{-1}$ until a number of charge-discharge cycles had been completed (**Fig. 2-10a**). In contrast, the O-H and $PF_6^-$ reference signals at 3430 $cm^{-1}$ and 842 $cm^{-1}$ were observed for CC-LNMC (**Fig. 2-10c**), supporting the hypothesis of $PF_6^-$ anion intercalation into the $Al(OH)_3$ coating layer during the cycle. Furthermore, results from XPS analysis (**Fig. 2-10b, d**) support the FTIR data. F1s XPS spectra obtained from the charged and discharged pristine sample have only two types of fluorine, fluorine bonded to carbon of PVDF (C-F at 687 eV) and fluorine bonded to lithium (LiF at 685 eV).[133, 134] In case of CC-LNMC material at the charged and discharged states, additional peak assigned to Al(OH)---$PF_6^-$ appeared at 687 eV (**Fig. 2-10d**). In addition, the intensity of the $PF_6^-$ signal at 842 $cm^{-1}$ in the FTIR spectra, and that of the Al(OH)---$PF_6^-$ signal from XPS analysis increased after discharging and decreased after charging. From these results, we could conclude that this amorphous $Al(OH)_3$ not only protects surface of the active material, but also successfully traps $PF_6^-$ anions.

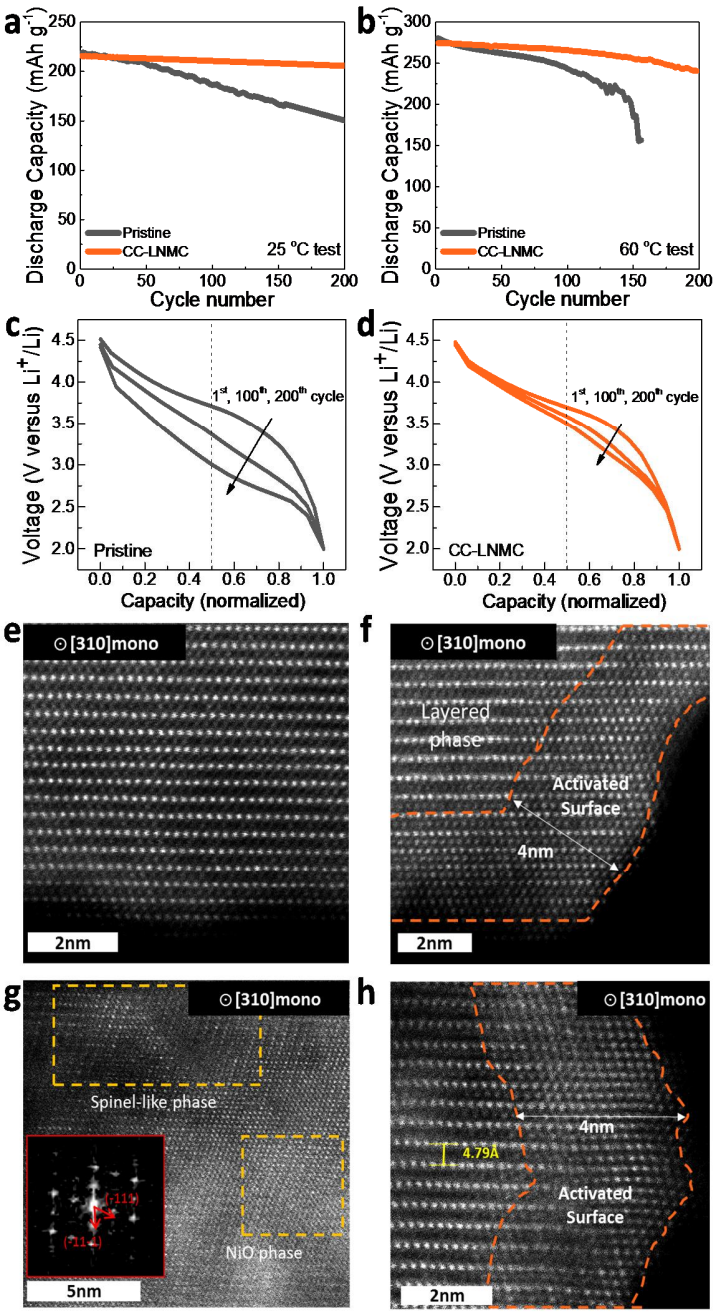


**Figure 2-11.** Comparison of electrochemical performances and structural analysis *via* TEM. (a) Comparison of 0.5C cycle retention at 25 °C. (b) Comparison of 0.5C cycle retention at 60 °C. (c) Voltage profile change of pristine during 0.5C cycle at 25 °C. (d) Voltage profile change of CC-LNMC during 0.5C cycle at 25 °C. (e) TEM image of pristine before cycling. (f) TEM image of CC-LNMC before cycling. (g) TEM image of pristine after cycling. (h) TEM image of CC-LNMC after cycling. All TEM images are obtained along $[3\ 1\ 0]_{monoclinic}$ zone axis.

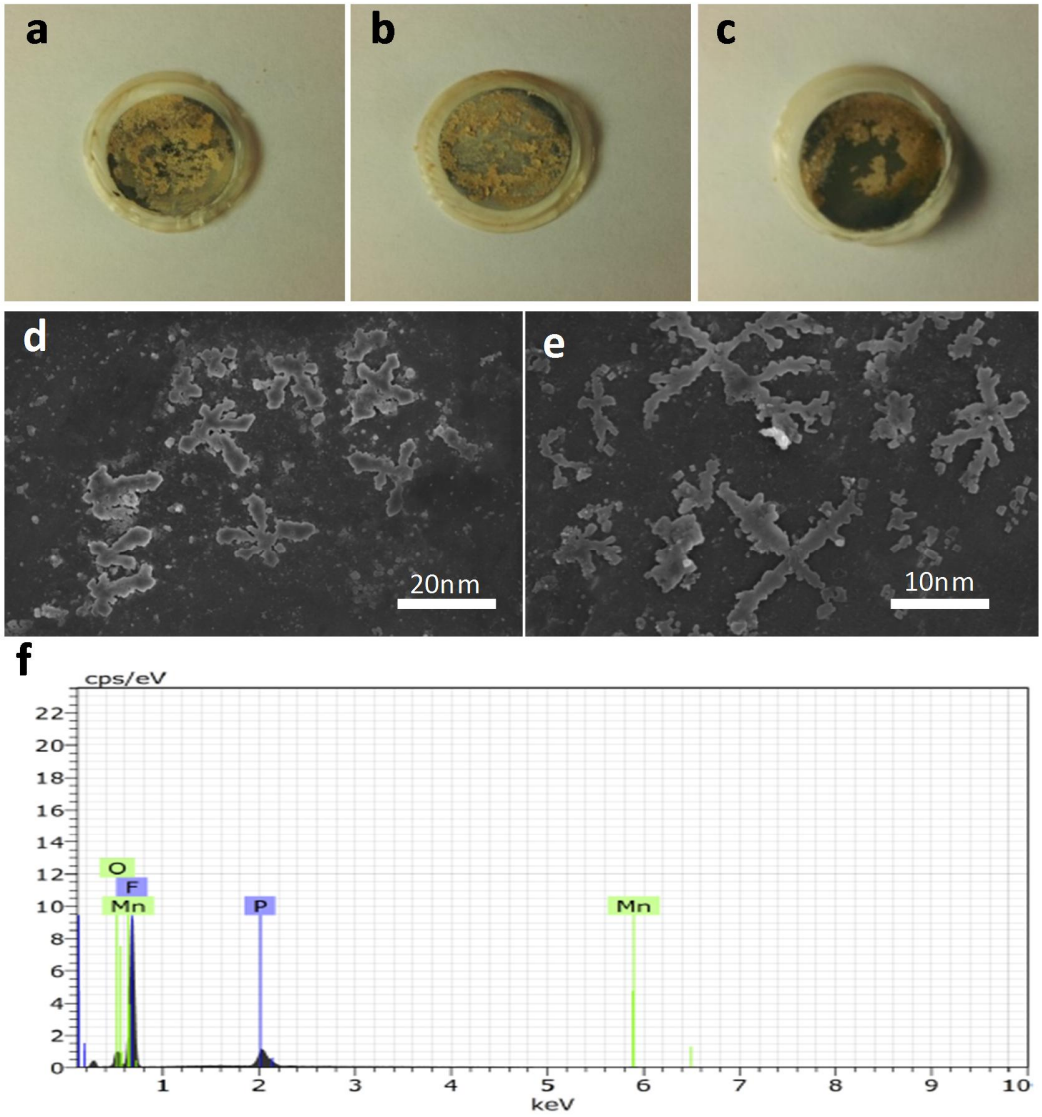


**Figure 2-12.** Separator from disassembled half-cell of (a) pristine, (b) PC-LNMC, (c) CC-LNMC after 100 cycles between 2.0 - 4.6 V at 60℃. (d,e) SEM images showing by-product particles on the separator. (f) Energy dispersive X-ray spectroscopy (EDS) spectrum of a particle attached to the separator, indicating that the particles are composed of F, P and O (82 : 7.5 : 10).

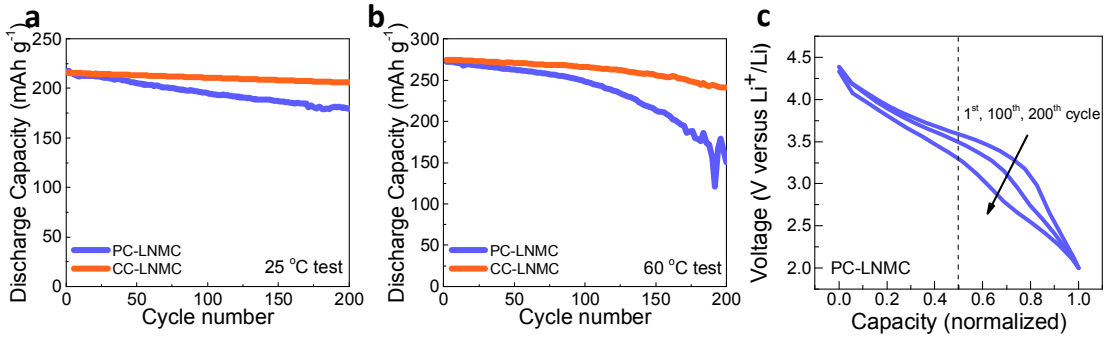


**Figure 2-13.** Comparison of electrochemical performances between PC-LNMC and CC-LNMC. Cycle retention test at (a) 25 °C, and (b) 60 °C. (c) Voltage profile change of PC-LNMC during 0.5C cycle at 25 °C.

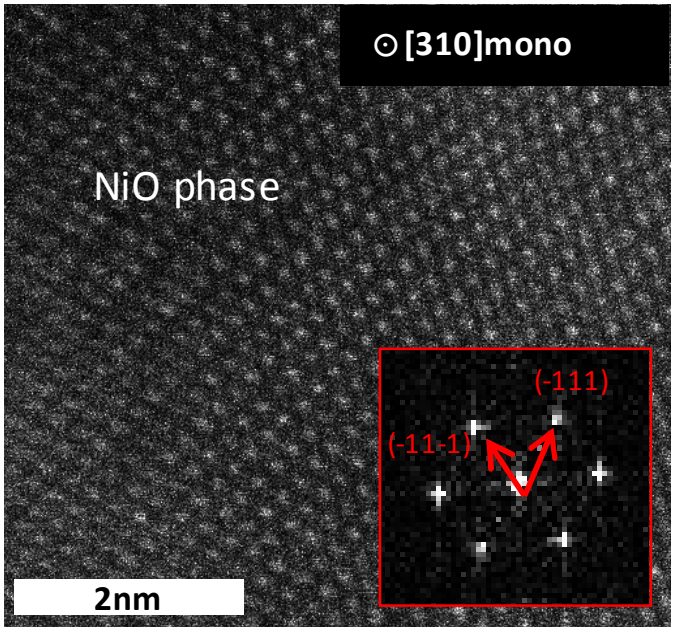


**Figure 2-14.** TEM image of pristine material after cycling.

**Relationship between electrochemical performance and structural stability.** Thanks to surface protection and anion trapping effect of completely covered and multifunctional $Al(OH)_3$ coating layer, CC-LNMC material could achieve superior capacity retention of 86% after 200$^{th}$ cycle at 25 °C (**Fig. 2-10a**), contrary to significant capacity fading of pristine material (68%). With more severe condition, such as high temperature of 60 °C, pristine material shows a sudden and rapid capacity drop after 120$^{th}$ cycle, however, CC-LNMC maintains its constant decreasing slope until 200$^{th}$ cycle (**Fig. 2-11b**). It is generally known that elevated temperature accelerates side reactions and formation of by-products, such as $Li_xPO_yF_x$, $POF_3$ and LiF, at the surface of active material.[135-137] These by-products are accumulated on the surface of separator (**Fig. 2-12a, b**) and they hinder lithium ion transfer between cathode and anode, finally it led to the sudden and rapid capacity drop. However, in the case of CC-LNMC, only a little amount of by-products are observed after cycles (**Fig. 2-12c**).

For Li-rich cathode materials, it has been considered as vital to alleviate voltage decay as much as capacity fading, so we have conducted analyses focused on this trend. Voltage decaying, one of the most unique properties of Li-rich material, is occurred by structural transformation from layered to spinel-like phase and increased over-potential originating from an electrochemically inactive SEI layer and by-products on the surface of active material. **Fig. 2-11c** and **2-11d** plot the working voltage of pristine and CC-LNMC based on **Fig. 2-11a**. While the CC-LNMC material shows superior voltage retention (3.70 V to 3.49 V) during the 200 cycles, the working voltage of pristine material reduced drastically from 3.71 V to 3.00 V. In addition, the voltage of the PC-LNMC dropped from 3.60 V to 3.25 V after 200 cycles as shown in **Fig. 2-13**. Voltage retention of CC-LNMC during the electrochemical charge and discharge process is enhanced by formation of chemically activated layer at the surface of the active material. It is already reported that hydrazine can act as a chemical activator for $Li_2MnO_3$ phase forming an artificially cation-mixed phase and inhibit voltage decay phenomenon of Li-rich materials.

To verify the effect of surface coating on the bulk structural retention in detail, atomic structural analysis *via* TEM analysis was investigated on pristine and CC-LNMC electrodes along $[310]_{monoclinic}$ direction (=$[110]_{cubic}$). **Fig. 2-11e and 4f** show TEM images of the atomic scale structures of pristine and CC-LNMC electrodes before cycling. Pristine material shows a highly ordered layered structure with a d-spacing value of 4.79 Å along $[003]_{hexagonal}$ direction and an absence of transition metal disordering between transition metal slab and lithium slab (**Fig. 2-11e**). Interestingly, CC-LNMC material, on the other hand, has a surface layer of cubic rock-salt phase with a thickness of approximately 4 nm (**Fig. 2-11f**). After 100 cycles, pristine material displays a large amount of the spinel-like phase and rock-salt phase over its surface (**Fig. 2-11g and Fig. 2-13**). Furthermore, fast Fourier transform (FFT) pattern of pristine clearly shows the presence of the cubic rock-salt and spinel-like phase patterns (inset of **Fig. 2-11g** and **Fig. 2-14**). An increase

in the spinel-like and rock salt phases during the cycles is directly related to the capacity decaying and voltage decay, due to the electrochemically inactive characteristics of the cation mixed phases. In contrast to the drastic structural degradation observed for pristine after 100 cycles, the CC-LNMC material retains the atomic arrangement of the layered structure with a small amount activated surface (**Fig. 2-11h**). This structural advantage in the CC-LNMC material could attribute to the superior working voltage retention at high charge voltage condition of 4.6V compared to both pristine material and PC-LNMC.

For a deeper understanding about the different voltage decaying tendencies of pristine, PC-LNMC, and CC-LNMC materials, dQ/dV plots were prepared based on 0.5C cycle test at room temperature (**Fig. 2-15**). Charge peak shift toward higher voltage and discharge peak shift toward lower voltage are interpreted as result of increased over-potential caused by surface side reactions. However, appearance of a new discharge peak below 3.0 V is considered as an evidence of 'layered-to-spinel' phase transition. In case of pristine material, both shift of charge/discharge peaks and appearance of the new discharge peak are observed, contrary to CC-LNMC, which retained its initial dQ/dV graph shape even after 200 cycles. From these interpretations of dQ/dV plots, we could understand how surface and structural stabilization effect of amorphous $Al(OH)_3$ coating layer get connected with electrochemical performances, such as cycle and voltage retention.

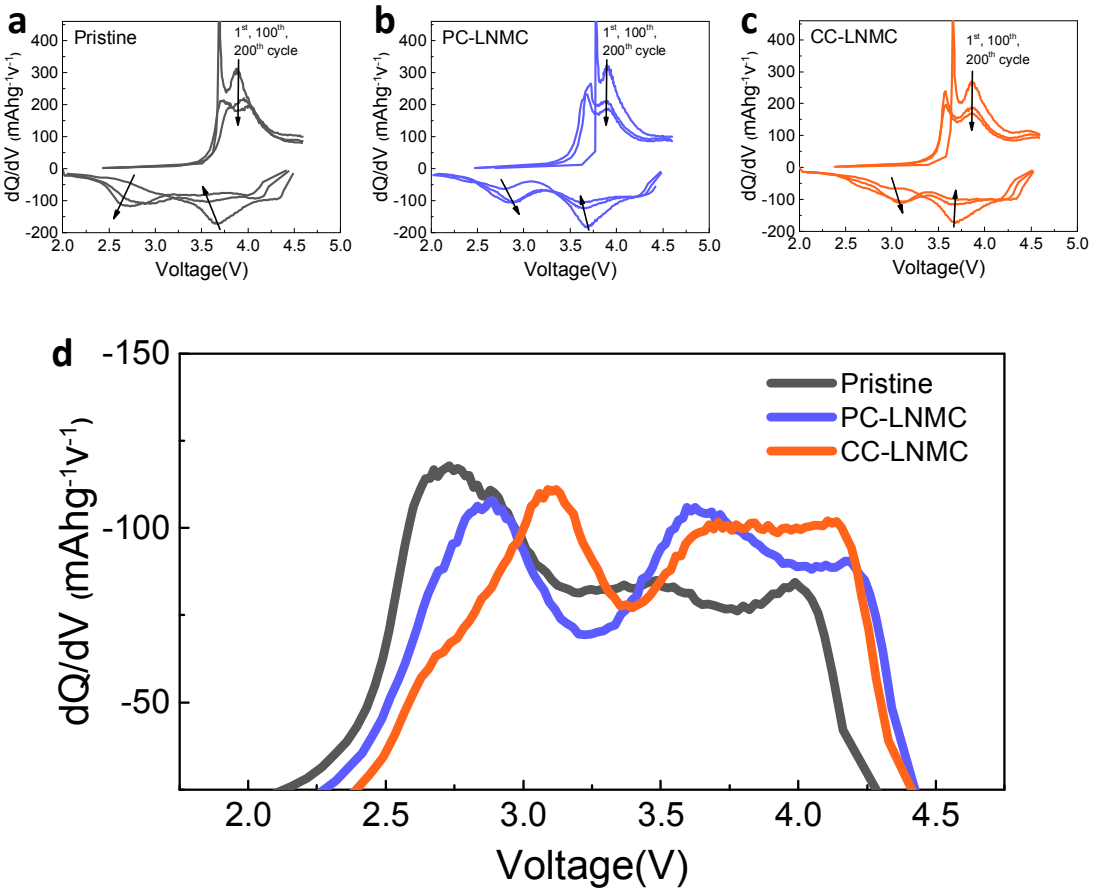


**Figure 2-15.** Changes in dQ/dV plots of (a) Pristine, (b) PC-LNMC, and (c) CC-LNMC during 0.5C cycle retention test at 25 °C. (d) Comparison of dQ/dV plots after 200 cycles.

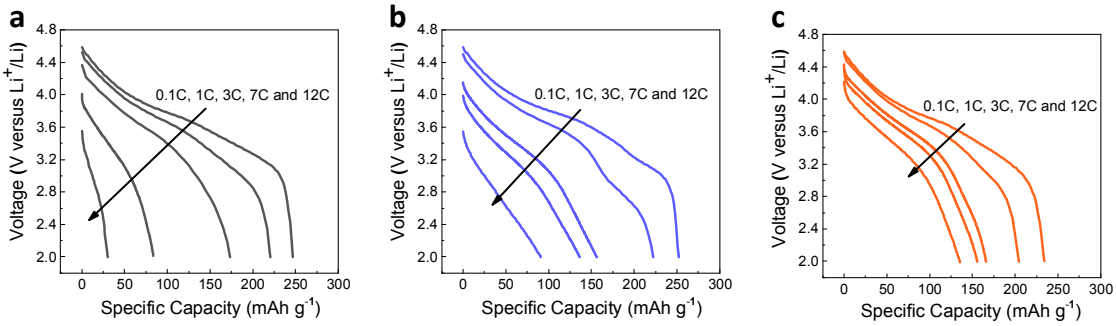


**Figure 2-16.** Change of discharge profile of (a) Pristine, (b) PC-LNMC, and (c) CC-LNMC at different C-rate.

In addition, surface and structural stabilization also critically affect the rate capability of the Li-rich material as determined by lithium ion diffusion. **Fig. 2-16** shows discharge capacity changes for pristine, PC-LNMC and CC-LNMC materials at different C-rates. All samples have a similar rate capability at current densities of below 1C, but their rate capabilities are clearly distinguishable at current densities above 3C, with CC-LNMC exhibiting a superior rate performance of 150 mAh $g^{-1}$ at 12C.

| Gravimetric Energy density (Wh $kg^{-1}$) | $LiNi_{0.8}Co_{0.15}Al_{0.05}O_2$ (3.0 – 4.3 V) | CC-LNMC (2.0 – 4.6 V) |
|---|---|---|
| 1st cycle | 693 | 780 |
| 200th cycle | 630 (90%) | 680 (87%) |

**Figure 2-17.** Gravimetric energy density comparison at 0.5C between CC-LNMC and $LiNi_{0.8}Co_{0.15}Al_{0.05}O_2$.

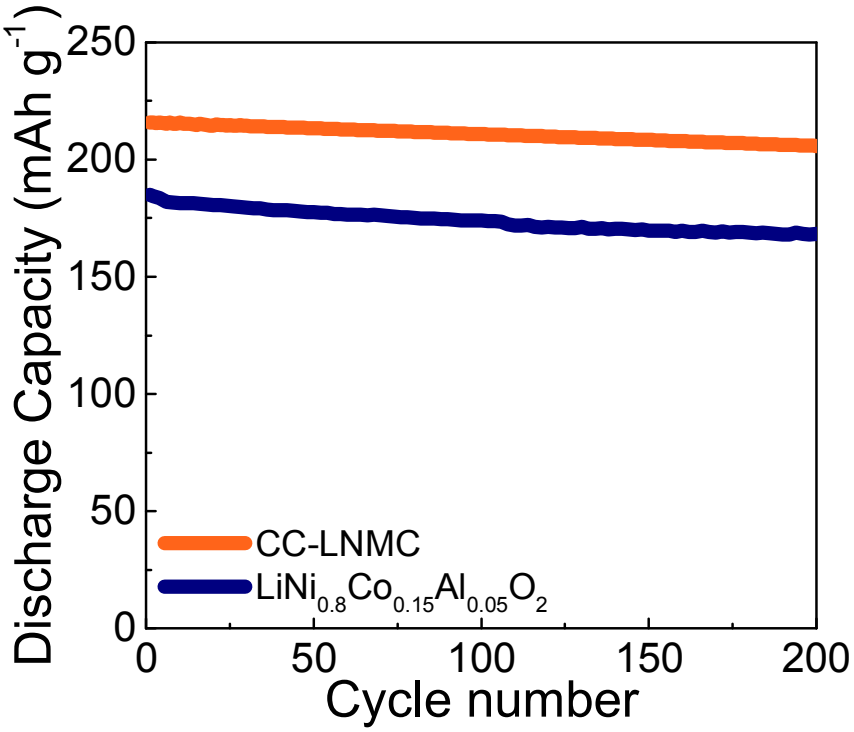


**Figure 2-18.** Cycle retention comparison between CC-LNMC and $LiNi_{0.8}Co_{0.15}Al_{0.05}O_2$ at room temperature.

## 2.4 Conclusion

In this study, we realized ideal coating morphology *via* pH control and spontaneous oxolation reaction with fundamental discernment about sol-gel coating mechanism. As a result, completely covered and multifunctional $Al(OH)_3$ coating layer enhanced electrochemical properties of Li-rich material in terms of voltage retention and high capacity retention at room temperature and 60 °C. This achievement is not only comparable to previous coating researches on Li-rich materials, but also comparable to high-nickel cathode materials (**Fig. 2-17 and 2-18**), which are considered as one of the most promising candidates for high-energy density cathode material. Consequently, this article provides a promising perspective for coating morphology and Li-rich materials.

# Chapter 3

## Understanding of voltage decay in Li-excess layered cathode materials through oxygen-centred structural arrangement

(With the support of Dr. Kim for XAS analysis)

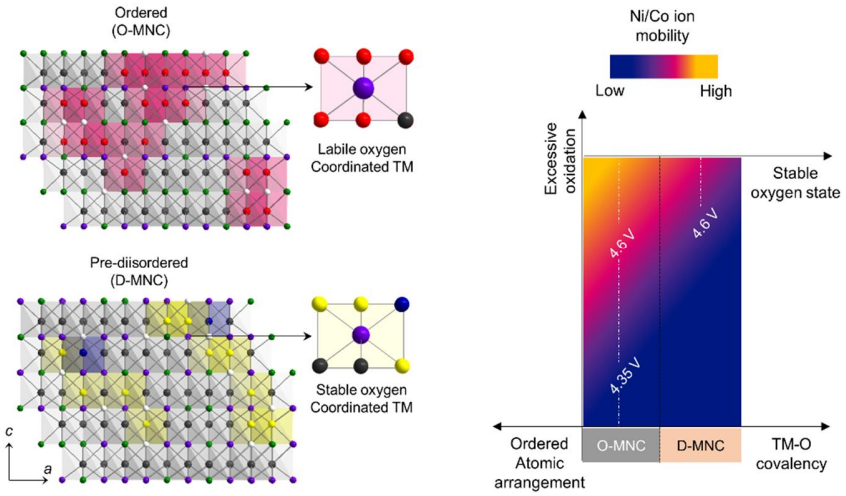


Li-excess 3*d*-transition-metal (3*d*TM) layered oxides ($Li_{1+x}Ni_yCo_zMn_{1-x-y-z}O_2$, > 250 mAh $g^{-1}$) suffer from severe voltage decay upon cycling, which decreases energy density and hinders further research and development. Nevertheless, lack of understanding on chemical and structural uniqueness of the material prevents the interpretation of internal degradation chemistry. Here, we discover a fundamental reason of the voltage decay phenomenon by comparing ordered and pre-disordered materials with a combination of X-ray absorption spectroscopy and transmission electron microscopy studies. The cation arrangement determines the TM-O covalency and structural reversibility related to voltage decay. The identification of structural arrangement with de-lithiated oxygen-centred octahedron ($M_4O$) and interactions between $M_4O$ octahedrons affecting the oxygen stability and TM mobility of transition-metal oxide provides a new insight into the degradation chemistry of cathode materials and a way to develop high-energy density electrodes.

**This chapter has not been published.**

## 3.1 Introduction

Despite the success of rechargeable lithium-ion batteries in Information Technology(IT) devices, many challenges still remain for large scale energy storage systems such as electric vehicles(EV) especially in terms of high-energy density and low cost.[138-140] High-capacity Li-excess 3*d*TM layered oxides ($Li_{1+x}Mn_yNi_zCo_{1-x-y-z}O_2$) are considered as a realistic candidate material for the approaching battery era owing to their high reversible capacities exceeding 250 mAh $g^{-1}$ and cost competitiveness because of inexpensive manganese.[141, 142] Nevertheless, industrial application is challenging due to their poor rate capability and severe discharge voltage decay.[40, 104, 143-146] Among these drawbacks, voltage decay phenomenon, which is not observed in other layered oxides, is an unique and delicate issue for researchers. Previous studies with cation-focused analysis interpreted this phenomenon as 'layered-to-spinel' phase transition and suggested 'surface doping' as a solution for the voltage decay.[113, 115, 147-158] Furthermore, 4d and 5d transition-metal (TM) oxides having a pure C2/m monoclinic structure, such as $Li_2Ru_{1-y}M_yO_3$ (M=Ti, Mn, Sn), were introduced to reveal origin of the voltage decay.[132]

However, Li-excess materials with 3*d*TM show structural uniqueness ($R\bar{3}m$ + $C2/m$) and no true $O_2^{2-}$ species on oxide oxidation, which is different from those of the heavier TM oxides.[107, 159] Recent important studies on Li-excess materials mainly focused on elucidating oxygen redox chemistry based on oxygen-centred octahedron ($M_6O$).[107, 160, 161] For instance, Ceder et al. suggested a useful participation of new Li-O-Li configuration in the oxygen redox activity for various Li-excess materials. Bruce et al. described electron-hole localization on oxygen surrounded by $Mn^{4+}/Li^+$ cations (O-$Mn^{4+}/Li^+$) to explain the oxygen chemistry in $Li_{1.2}Ni_{0.13}Co_{0.13}Mn_{0.54}O_2$. Despite such a reasonable local structural approaches, the voltage decay phenomenon can be still open issue, owing to a lack of consideration for long-range arrangement of de-lithiated $M_6O$ (M = transition metal or Li cation) octahedron and interactions affecting the overall oxygen stability. Therefore, multilateral and macroscopic analysis reflecting oxygen characteristics in a long-range structural arrangement is required to understand the voltage decay.

In this study, we focus on ordered and pre-disordered Li-excess 3*d*TM layered oxides showing significantly different degree of voltage decay. *Operando* atomic-selective X-ray absorption spectroscopic (XAS) analysis was conducted by synchronizing with dQ/dV plots to obtain a direct evidence of the voltage decay phenomenon. By combining spectroscopic and microscopic techniques, we observed the different gradation in TM-O covalency and atomic rearrangement considering structural uniqueness. Furthermore, different variation in specific TM-O bonding and TM ion migration depending on cycles, which can be a crucial parameter determining the degree of voltage decay, were revealed during cycling. Furthermore, we identify long-range structural arrangement with three types of de-lithiated oxygen-centred octahedron

($M_4O$) to discover a fundamental reason how atomic arrangement affects structural stability of Li-excess 3*d*TM layered oxides and the degree of voltage decay.

## 2.2 Experimental detail

***Sample preparation.*** $Li_{1.15}Mn_{0.51}Co_{0.17}Ni_{0.17}O_2$ (denoted as O-MNC) and $Li_{1.09}Mn_{0.55}Ni_{0.32}Co_{0.043}O_2$ (denoted as D-MNC), were prepared by co-precipitation method. Stoichiometric amounts of $MnSO_4 \cdot 5H_2O$ (99.0 %, JUNSEI), $NiSO_4 \cdot\cdot 6H_2O$ (98.5~102%, SAMCHUN) and $CoSO_4 \cdot\cdot 7H_2O$ (98.0 %, SAMCHUN) were used as the starting materials. An aqueous solution of the reagents at a concentration of 3.0 mol $L^{-1}$ was pumped into a continuously stirred tank reactor (CSTR; 4 L) under a nitrogen atmosphere. The pH was adjusted to 10.5 with a 3.0 mol $L^{-1}$ solution of NaOH, and a desired amount of a solution of $NH_4OH$ (4 mol $L^{-1}$) as a chelating agent was also separately fed into the reactor. The obtained solid was filtered, washed many times with distilled water, and then dried at 110°C for 12 h. The dried powder was thoroughly mixed with $LiOH \cdot H_2O$. (98.0 %, Sigma-Aldrich) and calcined at 900 °C for 10 h. To analyze the material characteristics, pristines and electrodes recovered in the discharged state at ~2.00 V after 10 and 100 cycles, respectively,

***Structural characterization.*** Structural characterization of the samples was carried out using SEM (Verios 460, FEI). HR-TEM (JEM-2100F, FEI) was conducted for detailed analysis. EDS was utilized in HR-TEM (EDS, Aztec, Oxford). XRD (D/Max2000, Rigaku) was carried out for the powder analysis using Cu-Ka radiation, a scan range of 10°–90°, a step size of 0.005°, and a counting time of 5 min. Rietveld profile refinements were performed using the GSAS suite of programs. HAADF-STEM images were obtained with aberration-corrected JEM-2100F electron microscopes operated at 160 kV using a convergence semi-angle of 22 mrad. The HAADF inner and outer collection semi-angle was 54 mrad and 220 mrad, respectively. Simulated HAADF/ABF-STEM image and FFT pattern were obtained by using Dr.probe and CrysTbox program.

***Operando X-ray Absorption Spectroscopy (XAS).*** *Operando* transition metal (TM = Mn, Ni, Co) K-edge X-ray absorption fine structure (XAFS), X-ray absorption near edge structure (XANES) and extended X-ray absorption fine structure (EXAFS), were collected on the BL10C beam line (WEXAFS) at the Pohang light source (PLS-II) with top-up mode operation under a ring current of 360 mA at 3.0 GeV. From the high-intensity X-ray photons of the multipole wiggler source, monochromatic X-ray beams could be obtained using a liquid-nitrogen-cooled double-crystal monochromator (Bruker ASC) with available *in situ* exchange in vacuum between a Si(111) and Si(311) crystal pair. The Si(111) crystal pair was used for TM K-edge XAFS measurements. Real-time TM K-edge X-ray absorption spectroscopic data during

discharging and charging processes were recorded for $10^{th}$-cycled OL-MNC, $10^{th}/100^{th}$-cycled OH-MNC, and $10^{th}/100^{th}$-cycled D-MNC electrodes assembled in a home-made *in situ* electrochemical cell with polyimide film windows (Swagelok-type cell), in transmittance mode using $N_2$ gas-filled ionization chambers (IC-SPEC, FMB Oxford) for the incident and transmitted X-ray photons. Higher-order harmonic contaminations were eliminated by detuning to reduce the incident X-ray intensity by ~30%. Energy calibration was simultaneously carried out for each measurement with reference TM foils placed in front of the third ion chamber. All XAFS data were measured using on-the-fly mode with scanning time of 1 minute for one spectrum per every 5 minutes. Under the 0.5 C-rate charging and 1C-rate discharging, XAFS spectra above 20 scans in charging and above 10 scans in discharging have been acquired independently for all electrodes. The data reductions of the experimental spectra to normalized XANES and Fourier-transformed radial distribution functions (RDFs) were performed through the standard XAFS procedure. Using AUTOBK and FEFFIT modules in UWXAFS package[1-3], the $k^3$-weighted TM K-edge EXAFS spectra, $k^3\chi(k)$, have been obtained through background removal and normalization processes on the edge jump. In order to present effective radial distribution functions (RDF) for each sample during charge-discharge, the $k^3\chi(k)$ spectra have been Fourier-transformed (FT) in the $k$ range between 2.5 and 12.0 $Å^{-1}$.

***Scanning Transmission X-ray Microscopy (STXM).*** STXM images and Soft X-ray absorption spectroscopy (SXAS) data were obtained at the Pohang Light Source (10A beam line) using the monochromatic soft X-rays of the synchrotron source. To obtain XAS spectra at the O K-edge, stacks of STXM images were obtained by changing the incident photon energy, while keeping the focal position at the sample plane, and then spectroscopic data from a specific point or area (in the lateral plane) were collected from the stack images through the aXis2000 software package. A monochromator resolution of 0.1 eV was used for recording SXAS spectra. Image stacks were acquired at 520–560 eV (O *K*-edge) to extract the X-ray absorption spectra from the surface region of samples.

***Electrochemical characterization.*** For fabrication of the cathode electrode, the prepared powders were mixed with carbon black and polyvinylidene fluoride (8:1:1) in N-methylpyrrolidinon. The obtained slurry was casted onto Al foil with active material loaded at 4.5-5.0 mg $cm^{-2}$ and roll-pressed. The electrodes were dried overnight at 110 °C in dry oven. The electrochemical performances of the prepared O-MNC and D-MNC were measured in tests using 2032 coin-type cells. The coin cells were assembled with Li metal as the counter and reference electrodes. In order to assemble the cell, CR2032 (half-cell) cell were utilized in argon-filled glove box. The electrolyte was a solution of 1.3 M $LiPF_6$ in ethylene carbonate (EC)/

ethylmethyl carbonate (EMC)/ diethyl carbonate (DEC)/ (2/5/3, by volume) with 5.0% of fluoroethylene carbonate, 0.5% of vinylene carbonate and 1.0% of tris(trimethylsilyl) phosphite. As a separator, microporous polyethylene (Celgard) was used. The galvanostatic charge-discharge cycling was carried out between 2.0 and 4.6 V(vs. Li/Li+) at 25°C temperature. To obtain accurate data, 4 cells per sample were tested.

## 2.3 Results and discussion

**Voltage decay phenomenon during cycling.** The Li-excess 3*d*TM layered oxides with different TM compositions, ordered $Li_{1.15}Mn_{0.51}Co_{0.17}Ni_{0.17}O_2$ (denoted as O-MNC) and pre-disordered $Li_{1.09}Mn_{0.55}Ni_{0.32}Co_{0.043}O_2$ (denoted as D-MNC), were prepared by co-precipitation method. Morphology and crystal structure were confirmed by scanning electron microscopy (SEM) and X-ray diffraction (XRD) (**Fig. 3-1,2 and 3**). O-MNC and D-MNC show initial discharge capacities over 250 mAh $g^{-1}$ with coulombic efficiency over 90%. For an exact comparison of voltage decay, we considered the 1$^{st}$ cycle reversible capacity because the amount of extracted lithium ion from the cathode material is directly related to structural degradation, and thus, voltage decay. Long-term cycling test of O-MNC were conducted with two different voltage cut-off conditions, 2.00–4.35 V (denoted as OL-MNC) and 2.00–4.60 V (denoted as OH-MNC) with 0.5 C and 1.0 C charge and discharge C-rates, respectively. Thereafter, we confirmed the discharge capacity from the 1$^{st}$ cycle: 150 mAh $g^{-1}$ for OL-MNC and 200 mAh $g^{-1}$ for OH-MNC. In addition, the D-MNC half-cell exhibited 200 mAh $g^{-1}$ at the 1$^{st}$ cycle in the voltage window of 2.00–4.60 V. All samples showed capacity retention of almost 93 % after 100 cycles (**Fig. 3-4 and 3-5**). The coloured regions in **Fig. 3-6a and b** show the difference in the degree of voltage decay from the 10$^{th}$ to 100$^{th}$ cycle for samples. The average voltages of OL-MNC and OH-MNC decreased by 31.6 mV and 317.0 mV during cycling, respectively (**Fig. 3-6a**); however, D-MNC shows only 56.0 mV of voltage decay (**Fig. 3-6b and 3-7**). This tendency is definitely recognized with dQ/dV plots shown in **Fig. 3-6c**. OH-MNC significantly exhibited both a disappearance of reduction peak at around 3.70 V and the new development of reduction peak at around 2.80 V during cycling, while OL-MNC retained its original profile even after 100$^{th}$ cycle. In case of D-MNC, the overall change in reduction peaks is suppressed despite the same electrochemical testing condition with OH-MNC.

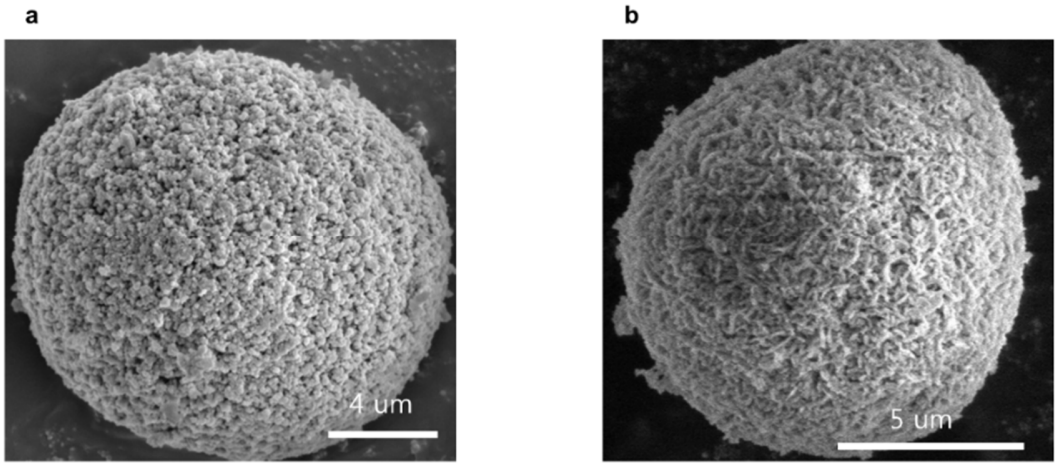


**Figure 3-1. SEM image of samples.** a) O-MNC and b) D-MNC.

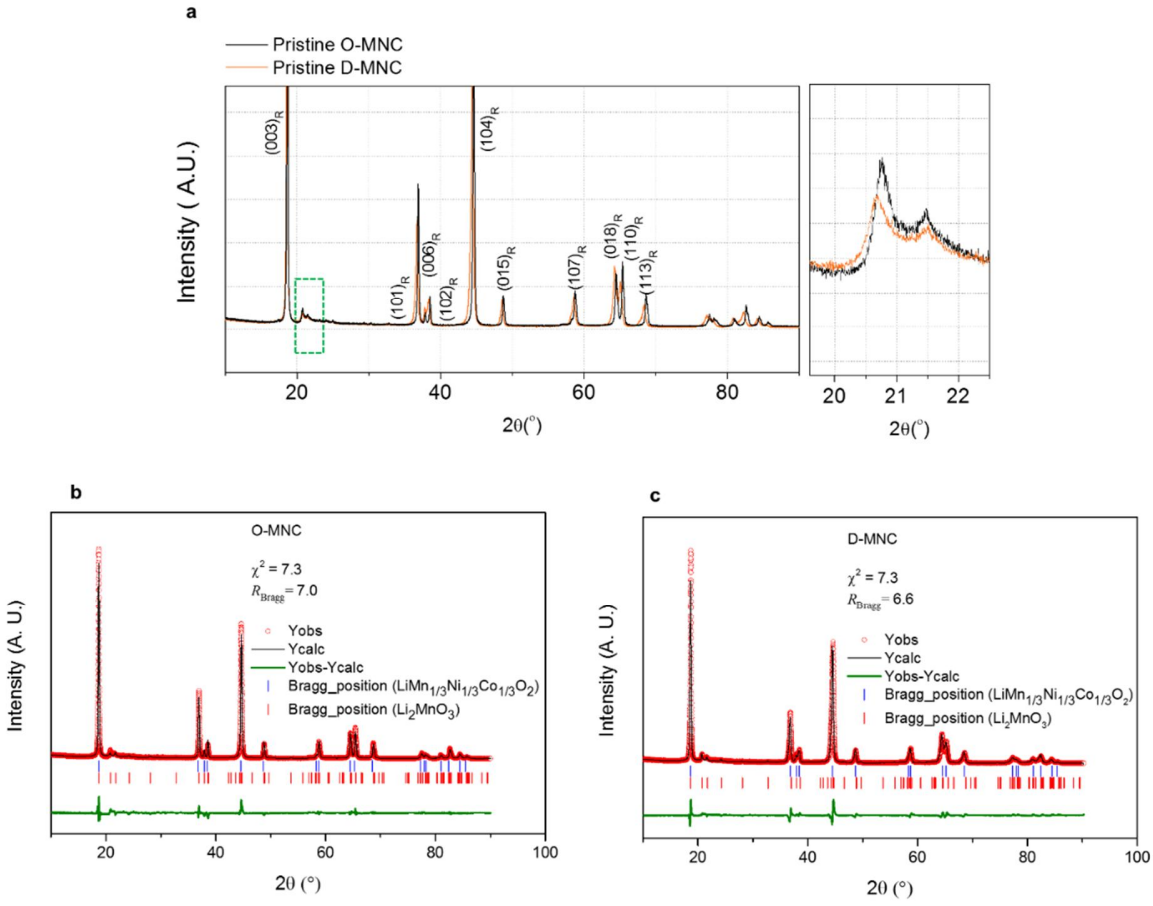


**Figure 3-2. X-ray diffraction (XRD) pattern analysis of O-MNC and D-MNC** a) comparison of XRD profiles of O-MNC and D-MNC. Rietveld refined XRD profiles of b) O-MNC and c) D-MNC. The

reference phases (C2/m phase, R3m phase) and differences of fitness are also presented in figures. Interestingly, almost all XRD peak of D-MNC shows broad and blunt indicating the low crystalline structure compared to O-MNC. The green rectangle in **a** shows the reflections from Li-TM-TM ordering within the $Li_2MnO_3$-like structure.

| | | O-MNC | D-MNC |
|---|---|---|---|
| R-3m phase | a- value ( Å ) | 2.8517 | 2.8714 |
| | c- value ( Å ) | 14.2356 | 14.2611 |
| C2/m phase | a- value ( Å ) | 4.9433 | 4.9561 |
| | b- value ( Å ) | 8.5571 | 8.5667 |
| | c- value ( Å ) | 5.0371 | 5.0364 |

**Figure 3-3. Crystallographic parameters for O-MNC and D-MNC.** As the Li-excess 3*d*-transition metal oxide is the mixture $Li_2MnO_3$ and $LiMO_2$ (M=Mn, Ni and Co) components, the Rietveld refined XRD patterns have been analyzed based on $Li_2MnO_3$ ($C2/m$) and $LiMn_{1/3}Ni_{1/3}Co_{1/3}O_2$ ($R\bar{3}m$) for both O-MNC and D-MNC. From the refinement result, the cell parameters of O-MNC and D-MNC based on $R\bar{3}m$ space group are (a=2.8517, c=14.2356) and (a=2.8714, c=14.2611), respectively.

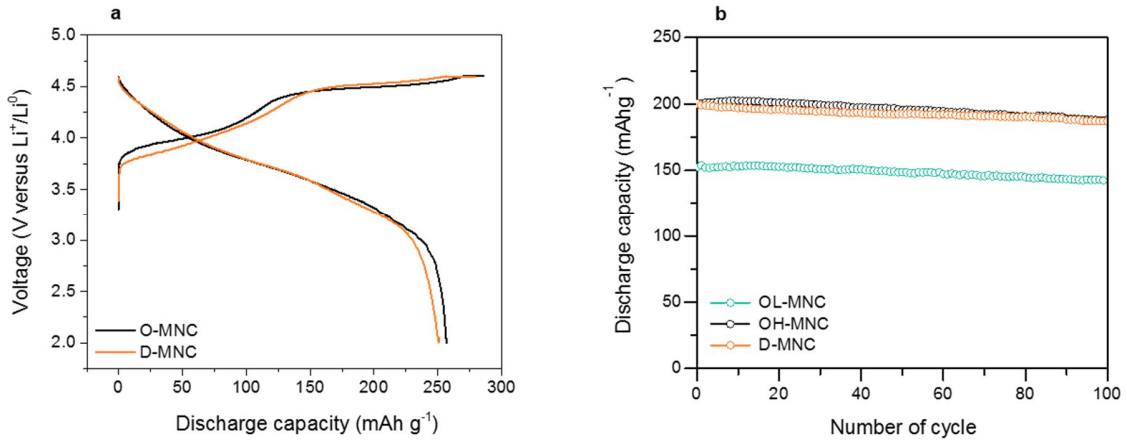


**Figure 3-4.** a) Initial charge-discharge curves for O-MNC and D-MNC in the 2.00-4.60 V (versus Li-metal) potential region; 0.1 C-rate charge 0.1 C-rate discharge condition; b) cycle plot of OL-MNC, OH-MNC and D-MNC

| Sample | 0.1C-rate Discharge capacity (mAh $g^{-1}$) 2.0 – 4.6 V (versus. Li-metal) 1C=200mA $g^{-1}$ | Coulumbic efficiency (%) | 1.0 C-rate Discharge capacity (mAh $g^{-1}$) | Cycle retention (%) |
|---|---|---|---|---|
| OL-MNC | 256 | 90 | 150 (1C = 256mA $g^{-1}$) | 93.5% |
| OH-MNC | 256 | 90 | 200 (1C = 256mA $g^{-1}$) | 93.8% |
| D-MNC | 250 | 93 | 200 (1C = 250mA $g^{-1}$) | 93.3% |

**Figure 3-5.** Electrochemical performances of the a) OL-MNC, OH-MNC and b) D-MNC.

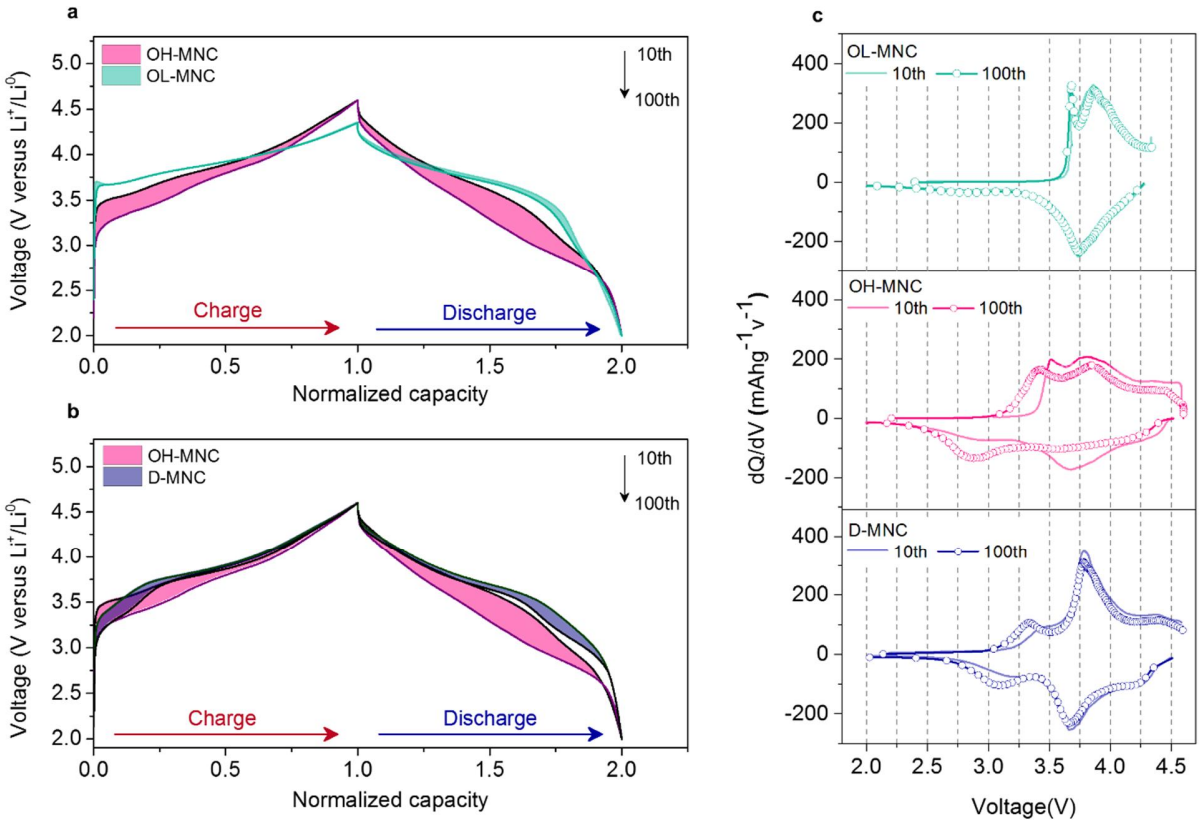


**Figure 3-6. Cycle behaviuor of O-MNC and D-MNC with a view towards voltage decay.** Normalized voltage profile variation for O-MNC and D-MNC from 10$^{th}$ to 100$^{th}$ cycles; Voltage profile variation of (**a**) O-MNC in the 2.00–4.35 V and 2.00–4.60 V (versus Li-metal) potential region.(**b**) O-MNC and D-MNC in the 2.00–4.60 V (versus Li-metal) potential region; 0.5 C-rate charge 1.0 C-rate discharge condition. The capacity normalization was performed by taking the maximum capacity in the corresponding cycle as unity. (**c**) dQ/dV plots for the O-MNC and D-MNC obtained from voltage profiles in **Fig. 3-6a and b.**

| Sample | Average voltage (V) | | | | | Voltage decay (V) |
|---|---|---|---|---|---|---|
| | 10cyc | 25cyc | 50cyc | 75cyc | 100cyc | V(100)-V(10) |
| OL-MNC | 3.722 | 3.718 | 3.707 | 3.696 | 3.690 | 0.0316 |
| OH-MNC | 3.599 | 3.513 | 3.422 | 3.335 | 3.282 | 0.317 |
| D-MNC | 3.694 | 3.668 | 3.655 | 3.647 | 3.637 | 0.056 |

**Figure 3-7.** Average discharge voltage values of the OL-MNC, OH-MNC and D-MNC at each cycle.

**Comparison of redox mechanism variation.** To elucidate the different redox reactions observed in dQ/dV plot during cycling, o*perando* Mn, Ni, and Co K-edges XANES spectra were collected for the $10^{th}$ and $100^{th}$ electrodes using the on-the-fly scan mode under the same electrochemical test condition above (**Fig. 3-8a-d**). The oxidation states of TMs in initial, charged, and discharged states at the $10^{th}$ and $100^{th}$ cycle were obtained from least-square method (**Fig. 3-9, 10, 11 and 12**).[31, 32] At the $10^{th}$ cycle, OH-MNC shows a wide variation range of oxidation state (ΔOx) and reduction state (ΔRed) towards higher oxidation states at the charged state due to a high cut-off voltage ($Mn^{3.65+}$/ $Ni^{3.08+}$/ $Co^{2.98+}$). In particularly, irreversible redox behaviour is observed at Mn state (ΔOx: 0.46/ ΔRed: 0.35). This contrasts with the redox reactions of D-MNC, which resulted in narrow ΔOx/ΔRed, lower oxidation states ($Mn^{3.53+}$/ $Ni^{2.88+}$/ $Co^{2.85+}$), and relatively reversible Mn redox (ΔOx: 0.34/ ΔRed: 0.29). This feature indicates that charged TM ion in D-MNC form relatively covalent bond with surrounded oxygen compare to that of OH-MNC. During the $100^{th}$ cycle, wider ΔOx/ΔRed was commonly observed in all TMs of D-MNC however, almost same oxidation states of Mn ion at $100^{th}$ charged states with $10^{th}$ charged states were observed in both OH-MNC and D-MNC.

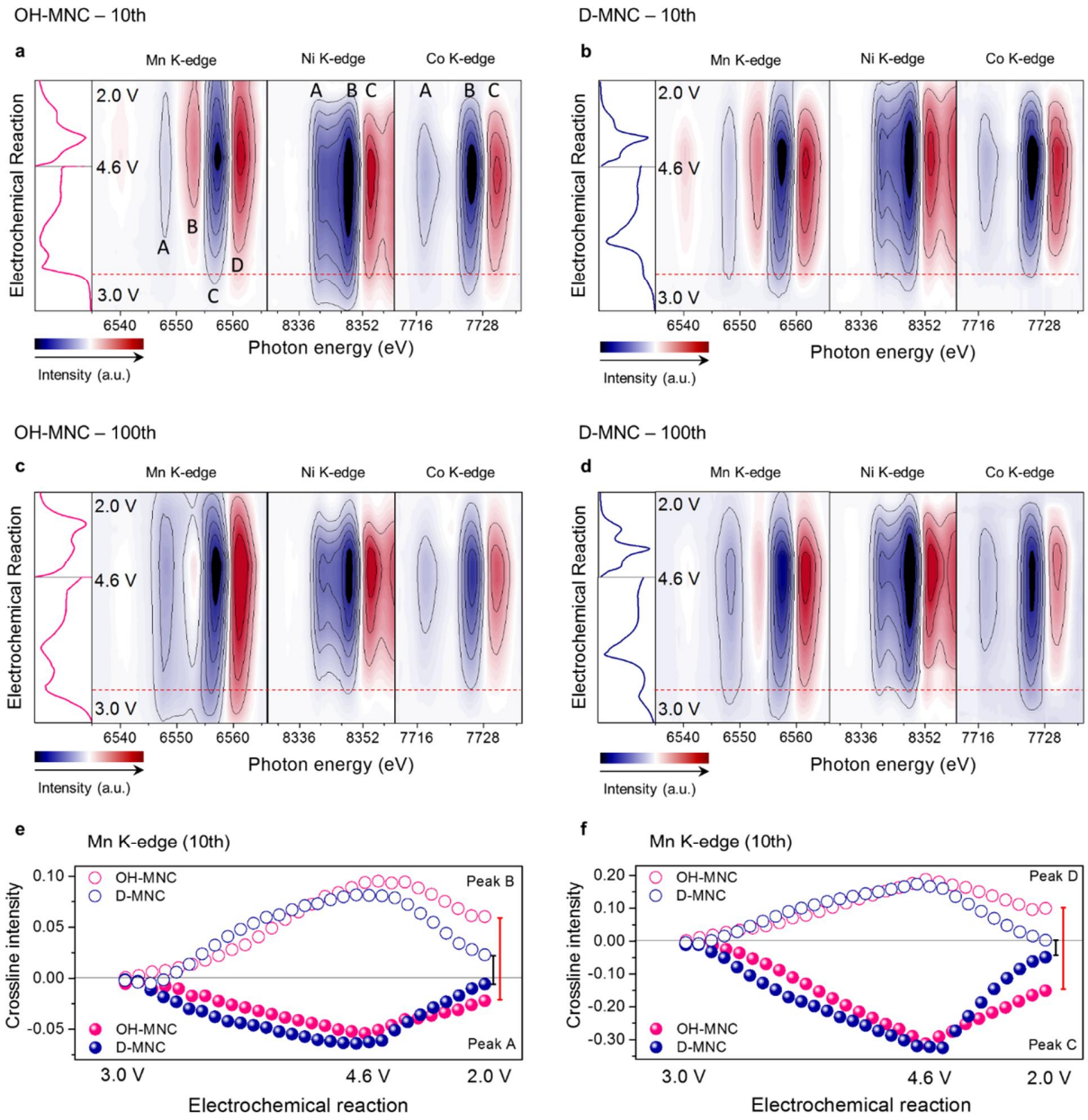


**Figure 3-8. Transition-metal K-edge *operando* XANES variation during cycling.** Mn, Ni, and Co K-edge o*perando* XANES spectra (2D contour plot) and voltage profiles of (**a**) OH-MNC 10$^{th}$, (**b**) D-MNC 10$^{th}$ , (**c**) OH-MNC 100$^{th}$, and (**d**) D-MNC 100$^{th}$**;** Crossline intensity of Mn K-edge *operando* XANES spectra peaks (**e**) A and B; (**f**) C and D during 10$^{th}$ cycle; Electrodes were cycled at 0.5C-rate charge 1.0C-rate discharge condition.

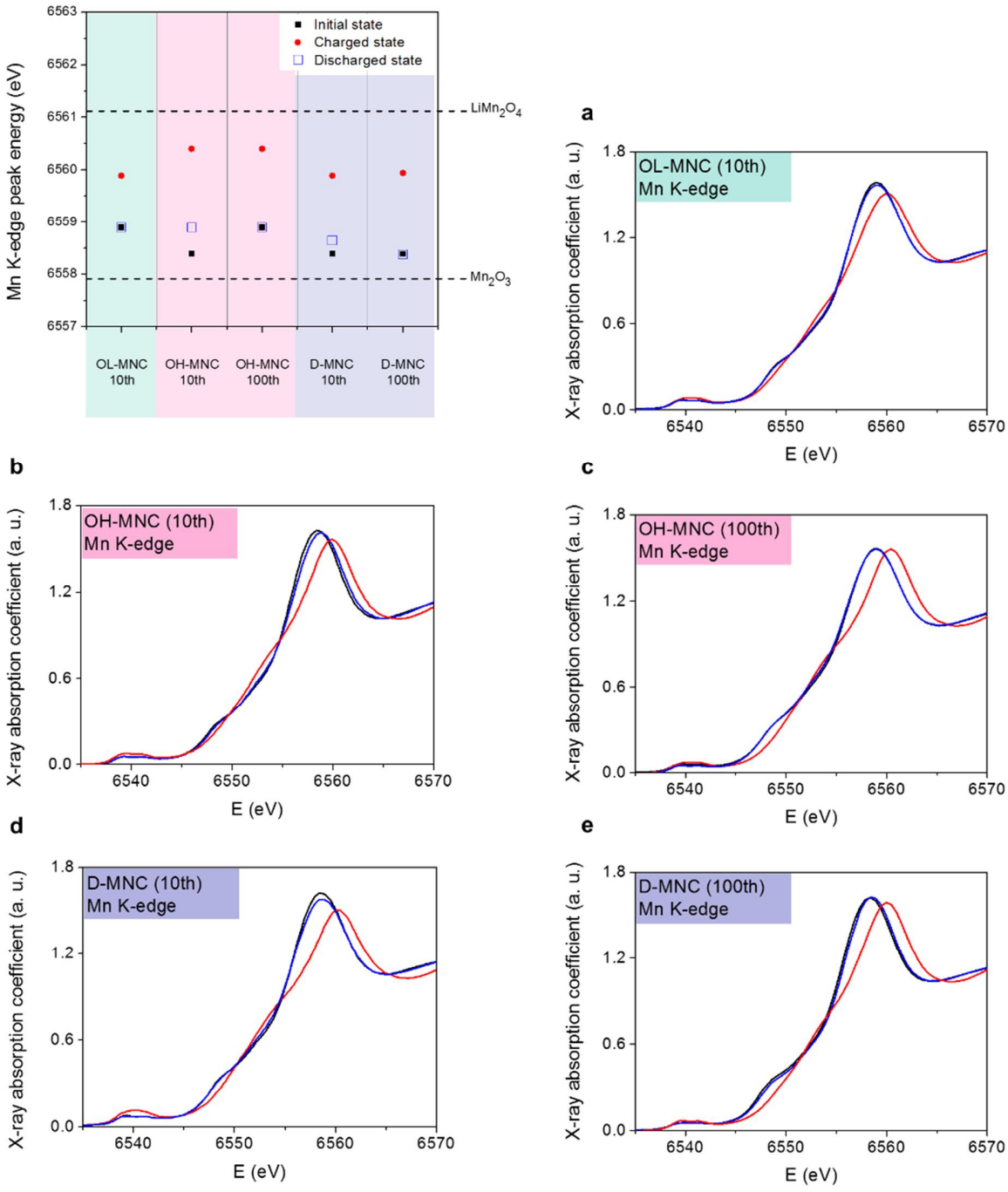


**Figure 3-9. Oxidation state variation of Mn ion for OL-MNC, OH-MNC and D-MNC during cycling.** Mn K-edge spectra of a) OL-MNC on 10$^{th}$ cycling b) OH-MNC on 10$^{th}$ cycling c) OH-MNC on 100$^{th}$ cycling d) D-MNC on 10$^{th}$ cycling e) D-MNC on 100$^{th}$ cycling.

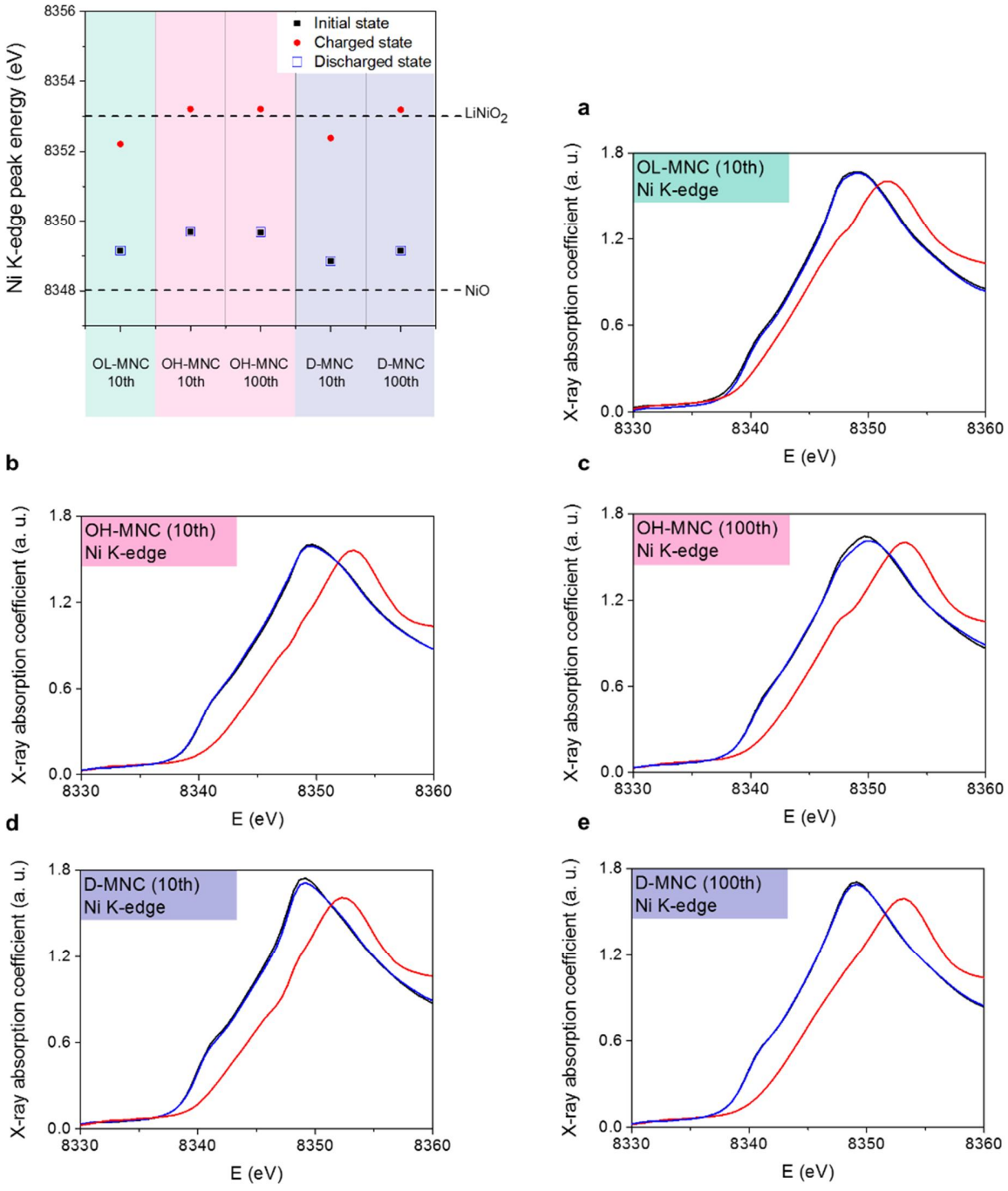


**Figure 3-10. Oxidation state variation of Ni ion for OL-MNC, OH-MNC and D-MNC during cycling.** Ni K-edge spectra of a) OL-MNC on 10$^{th}$ cycling b) OH-MNC on 10$^{th}$ cycling c) OH-MNC on 100$^{th}$ cycling d) D-MNC on 10$^{th}$ cycling e) D-MNC on 100$^{th}$ cycling.

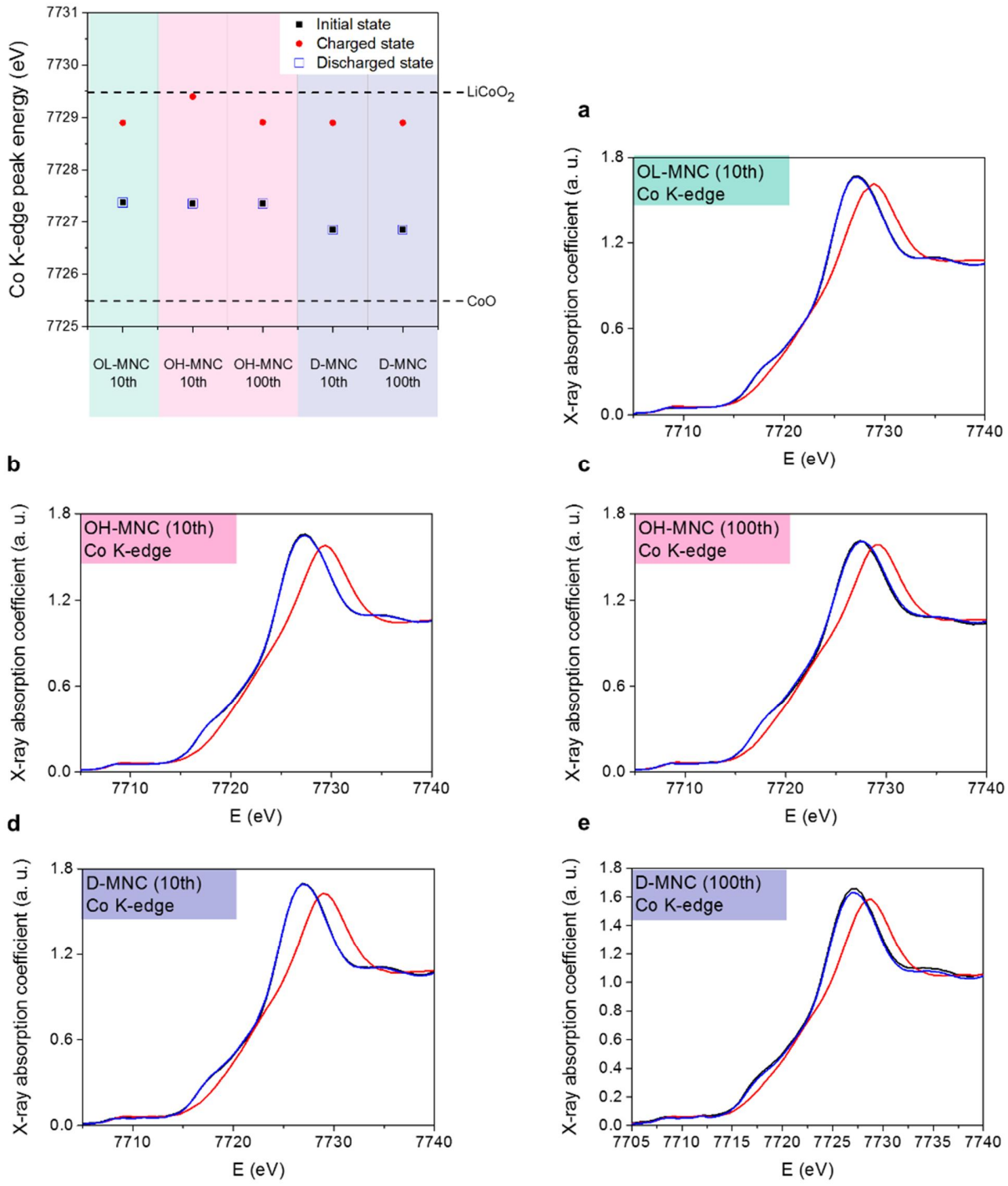


**Figure 3-11. Oxidation state variation of Co ion for OL-MNC, OH-MNC and D-MNC during cycling.** Co K-edge spectra of a) OL-MNC on 10$^{th}$ cycling b) OH-MNC on 10$^{th}$ cycling c) OH-MNC on 100$^{th}$ cycling d) D-MNC on 10$^{th}$ cycling e) D-MNC on 100$^{th}$ cycling.

| OL-MNC 10th | Initial state (eV) | ΔOx | Charged state (eV) | ΔRed | Discharged state (eV) | References (eV) |
|---|---|---|---|---|---|---|
| Mn K-edge | 6558.89 (3.30+) | 0.23 | 6559.89 (3.53+) | 0.23 | 6558.89 (3.30+) | 6558.00 ($Mn_2O_3$) 6561.00 ($MnO_2$) |
| Ni K-edge | 8349.15 (2.23+) | 0.61 | 8352.21 (2.84+) | 0.61 | 8349.15 (2.23+) | 8348.00 (NiO) 8353.00 ($LiNiO_2$) 8355.50 ($NiO_2$) |
| Co K-edge | 7727.38 (2.47+) | 0.38 | 7728.90 (2.85+) | 0.38 | 7727.38 (2.47+) | 7725.50 (CoO) 7729.50 ($LiCoO_2$) |

| OH-MNC 10th | Initial state (eV) | ΔOx | Charged state (eV) | ΔRed | Discharged state (eV) | References (eV) |
|---|---|---|---|---|---|---|
| Mn K-edge | 6558.39 (3.19+) | 0.46 | 6560.40 (3.65+) | 0.35 | 6558.89 (3.30+) | 6558.00 ($Mn_2O_3$) 6561.00 ($MnO_2$) |
| Ni K-edge | 8349.68 (2.34+) | 0.73 | 8353.21 (3.08+) | 0.73 | 8349.68 (2.34+) | 8348.00 (NiO) 8353.00 ($LiNiO_2$) 8355.50 ($NiO_2$) |
| Co K-edge | 7727.36 (2.47+) | 0.51 | 7729.40 (2.98+) | 0.51 | 7727.36 (2.47+) | 7725.50 (CoO) 7729.50 ($LiCoO_2$) |
| | | | | | | |
| D-MNC 10th | Initial state (eV) | ΔOx | Charged state (eV) | ΔRed | Discharged state (eV) | References (eV) |
| Mn K-edge | 6558.39 (3.19+) | 0.34 | 6559.89 (3.53+) | 0.29 | 6558.64 (3.24+) | 6558.00 ($Mn_2O_3$) 6561.00 ($MnO_2$) |
| Ni K-edge | 8348.85 (2.17+) | 0.71 | 8352.38 (2.88+) | 0.71 | 8348.85 (2.17+) | 8348.00 (NiO) 8353.00 ($LiNiO_2$) 8355.50 ($NiO_2$) |
| Co K-edge | 7726.85 (2.34+) | 0.51 | 7728.90 (2.85+) | 0.51 | 7726.85 (2.34+) | 7725.50 (CoO) 7729.50 ($LiCoO_2$) |

| OH-MNC 100th | Initial state (eV) | ΔOx | Charged state (eV) | ΔRed | Discharged state (eV) | References (eV) |
|---|---|---|---|---|---|---|
| Mn K-edge | 6558.89 (3.30+) | 0.35 | 6560.40 (3.65+) | 0.35 | 6558.89 (3.30+) | 6558.00 ($Mn_2O_3$) 6561.00 ($MnO_2$) |
| Ni K-edge | 8350.16 (2.33+) | 0.75 | 8353.21 (3.08+) | 0.75 | 8350.16 (2.33+) | 8348.00 (NiO) 8353.00 ($LiNiO_2$) 8355.50 ($NiO_2$) |
| Co K-edge | 7727.36 (2.47+) | 0.38 | 7728.91 (2.85+) | 0.38 | 7727.36 (2.47+) | 7725.50 (CoO) 7729.50 ($LiCoO_2$) |
| | | | | | | |
| D-MNC 100th | Initial state (eV) | ΔOx | Charged state (eV) | ΔRed | Discharged state (eV) | References (eV) |
| Mn K-edge | 6558.38 (3.18+) | 0.37 | 6559.94 (3.55+) | 0.37 | 6558.38 (3.18+) | 6558.00 ($Mn_2O_3$) 6561.00 ($MnO_2$) |
| Ni K-edge | 8349.15 (2.23+) | 0.85 | 8353.19 (3.08+) | 0.85 | 8349.15 (2.23+) | 8348.00 (NiO) 8353.00 ($LiNiO_2$) 8355.50 ($NiO_2$) |
| Co K-edge | 7726.85 (2.34+) | 0.51 | 7728.90 (2.85+) | 0.51 | 7726.85 (2.34+) | 7725.50 (CoO) 7729.50 ($LiCoO_2$) |

**Figure 3-12. XANES peak energy values of the OL-MNC, OH-MNC and D-MNC at Initial, charged and discharged state.**

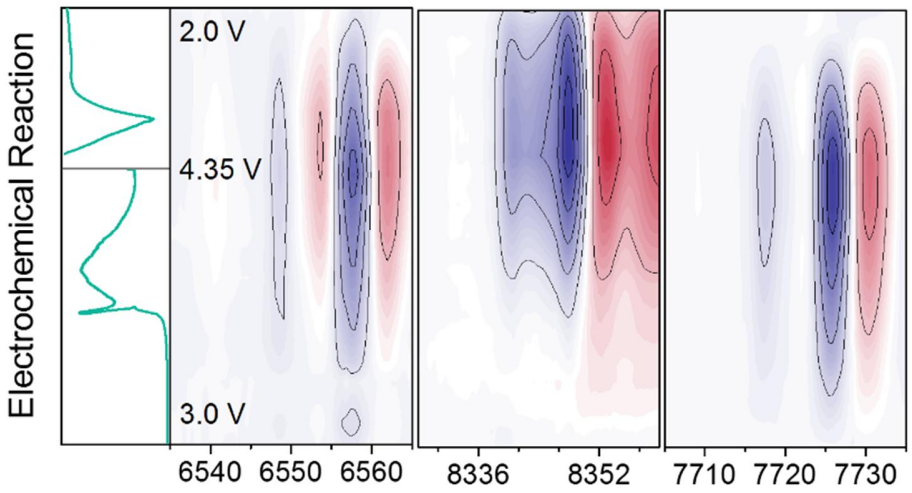


**Figure 3-13. *Operando* XANES characterization of the OL-MNC during cycling.** Normalized Mn, Ni and Co K-edge *operando* XANES spectra (2D contour plot) and voltage profiles of OL-MNC on 10$^{th}$ cycling.

In order to elucidate real-time redox reaction depending on the voltage decay during 10$^{th}$ and 100$^{th}$ cycle, differentiated XANES spectra ($\chi_i$ - $\chi_{pristine}$) were presented with 2D-contour map by synchronizing with dQ/dV plots in **Fig. 3-8a-d** and **3-13**. In the crossline intensities of each peak during the cycle, Mn K-edge XANES of OH-MNC is significantly more irreversible than that of D-MNC (**Fig. 3-8e and 3-8f**), while reversible behaviour of Ni and Co is observed in both OH-MNC and D-MNC (**Fig. 3-14 and 3-15**).

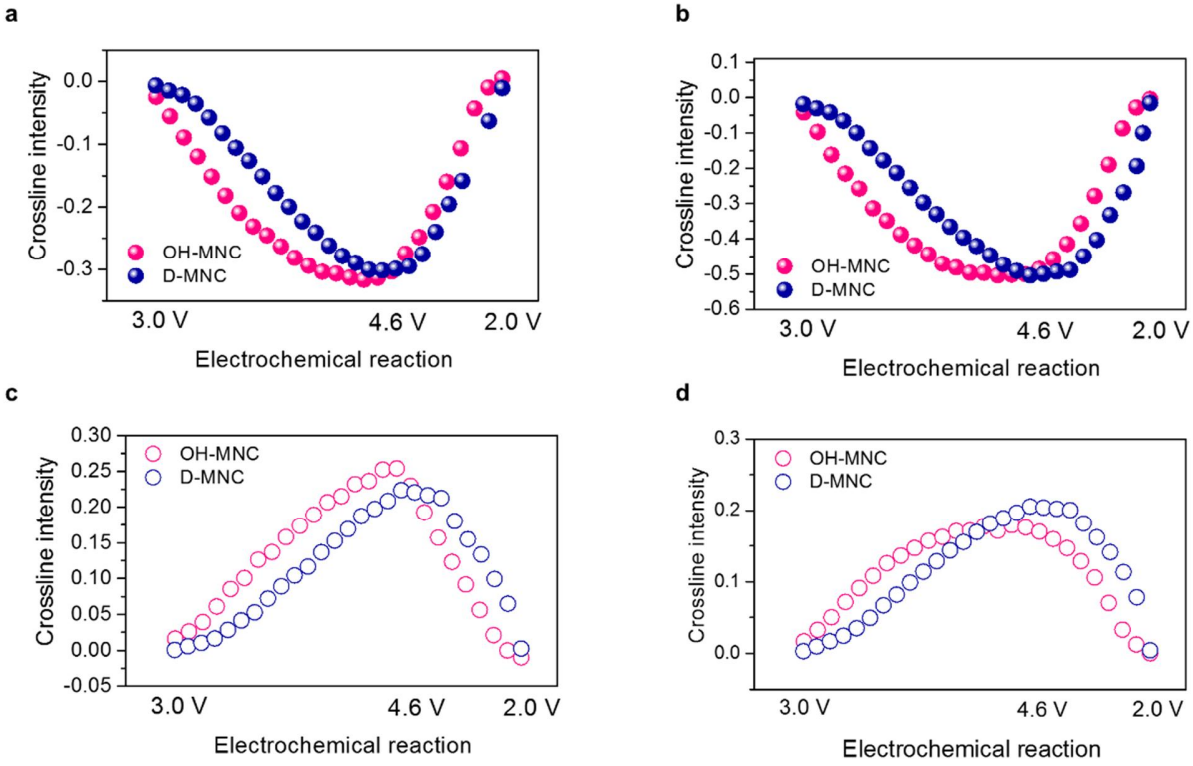


**Figure 3-14. Crossline intensity of Ni K-edge *operando* XANES spectra during 10$^{th}$ cycle.** Crossline intensity of a) peak A; b) peak B; c) peak; C d) peak D

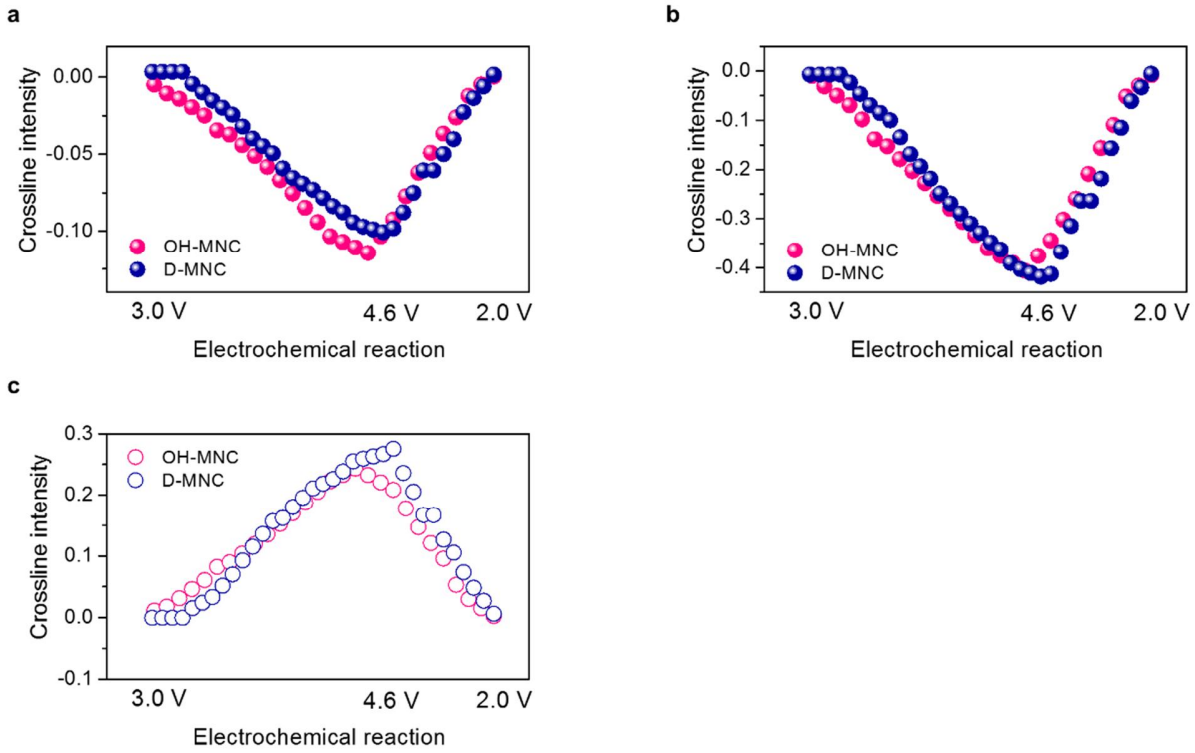


**Figure 3-15. Crossline intensity of Co K-edge *operando* XANES spectra during 10$^{th}$ cycle.** Crossline intensity of a) peak A; b) peak B; and c) peak C

During the 100$^{th}$ cycle, D-MNC not only retains the overall patterns of TM K-edges, but also shows more solidified peak features (**Fig. 3-8d**). However, the 100$^{th}$ OH-MNC shows different 2D contour map pattern from 10$^{th}$ cycle (**Fig. 3-8c**) in which overall peak intensity of patterns are gradually diminished at Ni and Co K-edge. Furthermore, Mn K-edge of 100$^{th}$ cycle shows very different overall peak features contrast to that of 10$^{th}$ cycle. Consequently, it can be expected that the structural instability associated with irreversible Mn ion redox at 10$^{th}$ cycle is a critical factor causing the abnormal behaviour in redox activities of Ni/Co and Mn ions during cycling, resulting in the noticeable peak decrease at around 3.70 V and peak increase at around 2.80 V in dQ/dV plot.

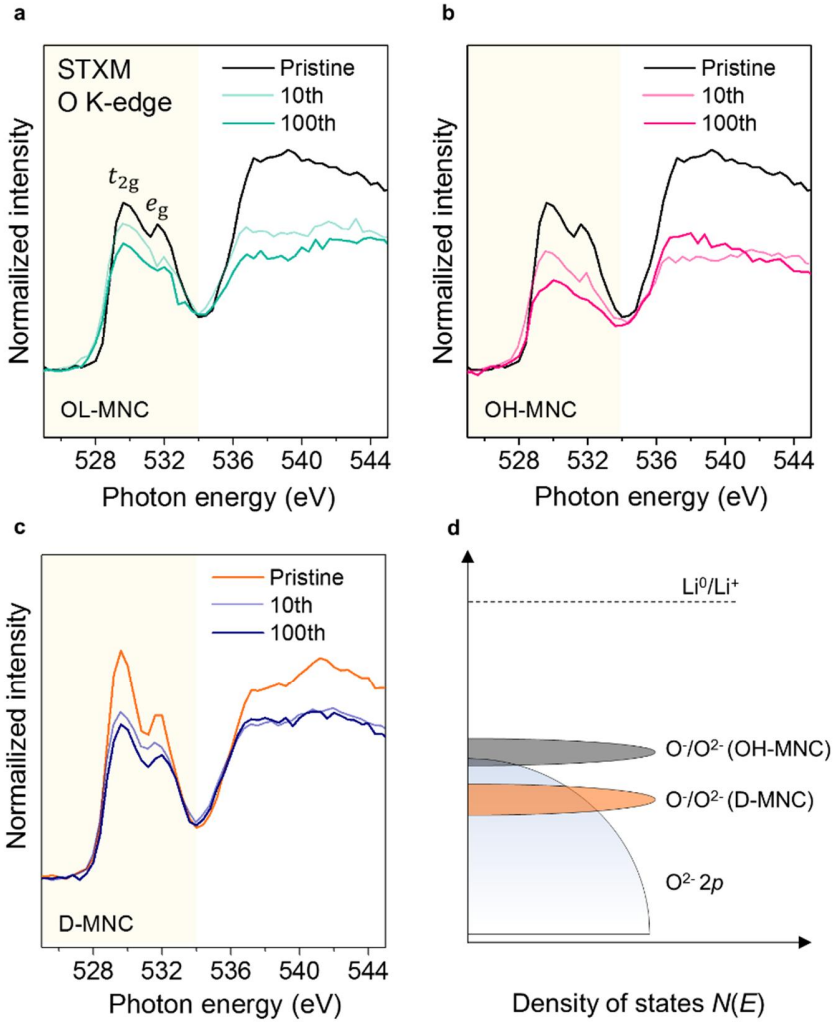


**Figure 3-16. Oxygen stability of TM-O bonding and electron hole localization on oxygen.** Oxygen K-edge SXAS spectrum of (**a**) OL-MNC (**b**) OH-MNC (**c**) D-MNC; the spectra collected on Pristine, 10$^{th}$ cycled and 100$^{th}$ cycled particle. (**d**) Schematic diagram of the possible $O^-/O^{2-}$ redox couple position base on TM-O covalency variation observed in O K-edge SXAS.

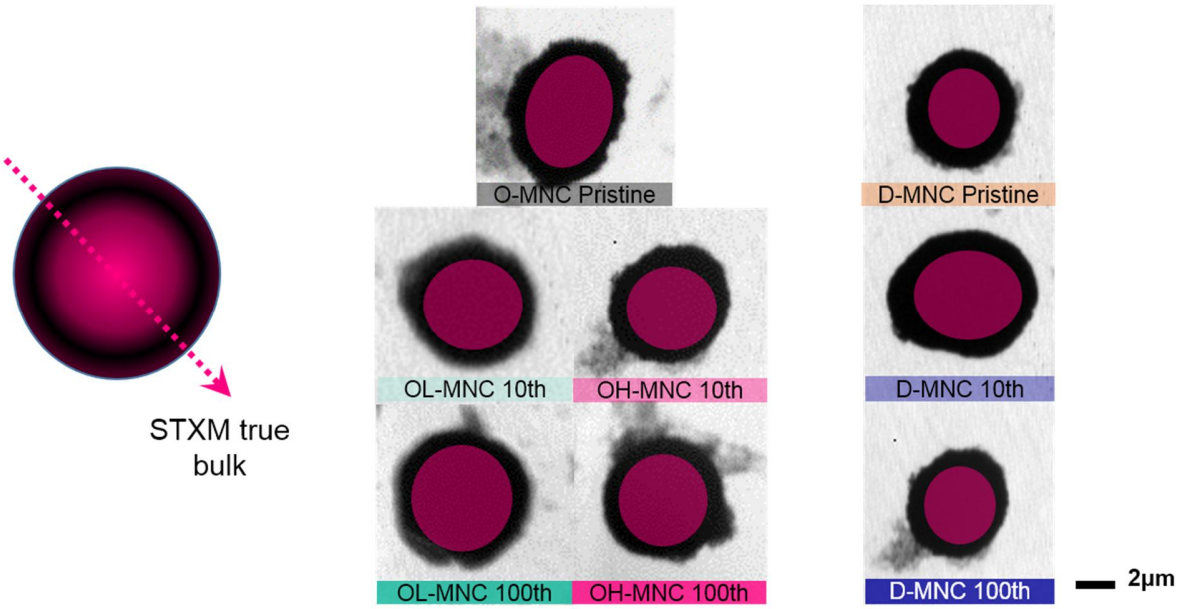


**Figure 3-17.** STXM images of pristine O-MNC, D-MNC and cycled samples (10th and 100th cycled OL-MNC, OH-MNC and D-MNC)

**Electronic structure of TM-O bonding.** The electron-hole state in TM-O bonding is closely related to structural stability, resulting in TM redox activity variation; thus, scanning transmission X-ray microscopy (STXM) was performed to reveal the oxygen state in materials, which undergo both TM and oxygen redox during electrochemical reactions. **Figure 3-16a–c** shows the O K-edge soft X-ray absorption spectroscopy (Soft-XAS) data of free standing pristine and cycled OL-MNC, OH-MNC, and D-MNC single particles chosen by microscopy imaging (**Fig. 3-17**). Firstly, the broad main peak of the O K-edge spectra above 534.0 eV corresponds to transition from O1*s* to the hybridized state of O2*p* and TM4*sp* orbitals. Secondly, the shaded area below 534.0 eV in **Fig. 3-16** indicates the hybridized state of

O2*p* and TM3*d* orbitals (O2*p*–TM3*d*). The distinct doublet peak feature in the pre-edge region (peak A at ~529.5 eV and peak B ~531.0 eV) are associated with the transition of O1*s* electron to the hybridized state of O*2p* with TM$3dt_{2g}$ and TM$3de_g$ states, respectively.[107, 164, 165]

The intensity of peak A in the pristine O-MNC is remarkably lower than that in D-MNC, implying that the electrons originating from oxygen vacancy ($O_O = V''_O + 2e^- + 0.5O_2$) occupy the TM3$d\ t_{2g}$ states. Therefore, higher intensity in D-MNC means more covalent interaction on O*2p*–TM3$d\ t_{2g}$ hybridized orbital. After the 10$^{th}$ and 100$^{th}$ cycles, the integrated intensity of the pre-edge peak (area of the shaded region in **Fig. 3-16a**), which is directly related to the degree of TM-O covalency, gradually decreased by ~0.82%/~2.62% for OL-MNC and dramatically decreased by ~3.54%/~16.22% for OH-MNC. In contrast, D-MNC still shows obvious pre-edge peaks, whose intensities gradually decrease by ~2.46%/~6.86% (**Fig. 3-16c and 18**).[27-29] Decrease in integrated intensity of the pre-edge peak until 10$^{th}$ and 100$^{th}$ cycle is dominantly correlated with activation of $Li_2MnO_3$ accompanying oxygen loss and overall structural degradation, respectively.

On oxidation (lithium extraction) of OH-MNC and D-MNC, electrons are removed from the TM orbital and electron transfer from the O2*p* band to the TM band occurs to compensate charge neutrality with hole creation in the O2*p* band. [164, 165,] Therefore, repeated charge-discharge process with high voltage condition leads to excessive hole creation in the O*2p* orbital and labile oxygen state. Consequently, the conservation of pre-edge peak intensities in D-MNC after 10$^{th}$ and 100$^{th}$ cycle means that the covalent bonding character of O-3*d*TM loses less oxygen from the lattice during cycling even at a high voltage, which originated from more covalent and high possibility of hole-delocalization on $Mn^{3.53+}$-O bonding in contrast to $Mn^{3.65+}$-O bonding of OH-MNC (**Fig. 3-16d**). [107, 166]

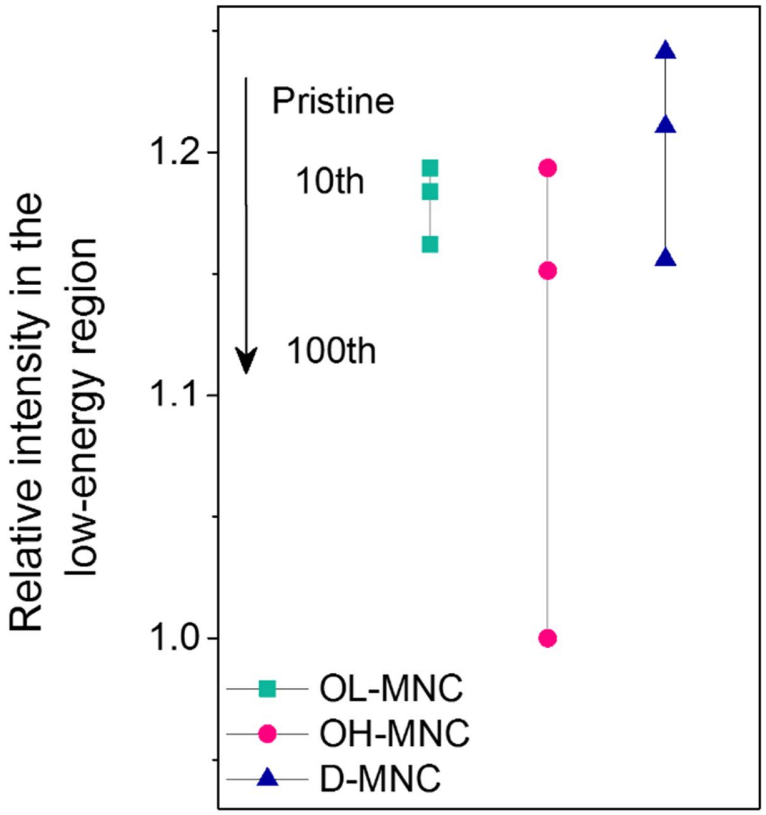


**Figure 3-18.** Variation of the integrated intensity in the pre-edge peak region (shaded region in **Fig. 3-16a-c**) for O K-edge SXAS.

**Microscopy atomic arrangement analysis.** A combination of high-angle annular dark-field scanning transmission electron microscopy (HAADF-STEM) and energy dispersive X-ray spectroscopy (EDS) reveals the correlation between oxygen stability and structural arrangement. To accurately study the structure, phase transitions along the $[310]_{mono}$ and $[100]_{mono}$ zone axes, which distinguishes from $R\bar{3}m$ layered oxides were investigated. Pristine O-MNC features a well-ordered layered structure without cation disordering within the Li layer along the $[100]_{mono}$ and $[310]_{mono}$ directions. Both TM-TM-TM arrangement of $LiTMO_2$ structure and Li-TM-TM of the $Li_2TMO_3$ structure coexisted in O-MNC along the $[100]_{mono}$ direction. Additionally, a spot-streak in the FFT pattern of pristine O-MNC resulting from the coexistence of $Li_2TMO_3$ structure along $[100]_{mono}$, $[\bar{1}\bar{1}0]_{mono}$, and $[\bar{1}10]_{mono}$ indicates stacking faults in O-MNC.[167] In contrast, cation disordering within the Li layer were observed in pristine D-MNC along $[310]_{mono}$ and $[100]_{mono}$ directions (**Fig. 3-19a, 3-19b and Fig. 3-20**).[167-171]

After 100 cycles, OH-MNC shows severe phase transition along both $[310]_{mono}$ and $[100]_{mono}$ directions, originating from the cation migration between the TM ($LiTMO_2$ phase) / LiTM ($Li_2TMO_3$ phase) layers and Li layers (denoted as $O_{TM}$, $O_{LiTM}$, and $O_{Li}$) (**Fig. 3-19c and 3-19d**). Migration of cations from $O_{TM}$ and $O_{LiTM}$ to $O_{Li}$ causes propagation of Domain B ($LiTM_3O_4$ phase) into the internal structure during cycling. Continuous Li intercalation and oxygen loss leads to additional cation migration from octahedral site to tetrahedral site, resulting in Domain A ($TM_3O_4$ phase) at the outer surface of OH-MNC which directly contacted with electrolyte (**Fig. 3-21 and 3-22**). These structures match well with the simulated HAADF/ABF-STEM image of I41 structure model along both $[310]_{mono}$ and $[100]_{mono}$ directions.

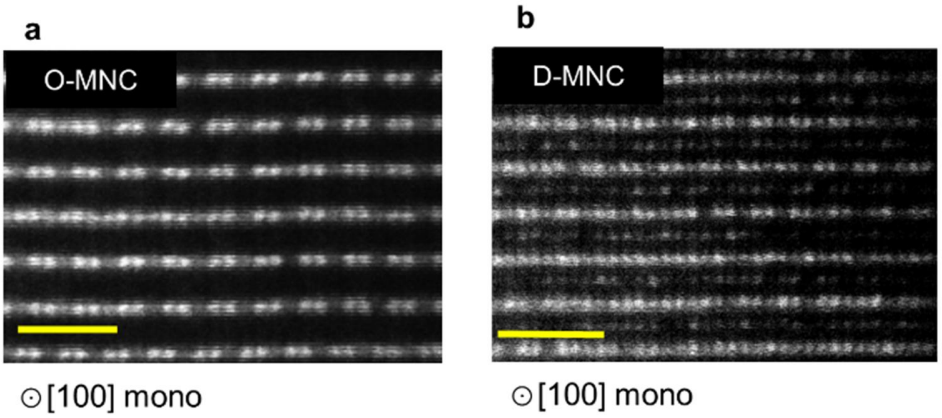

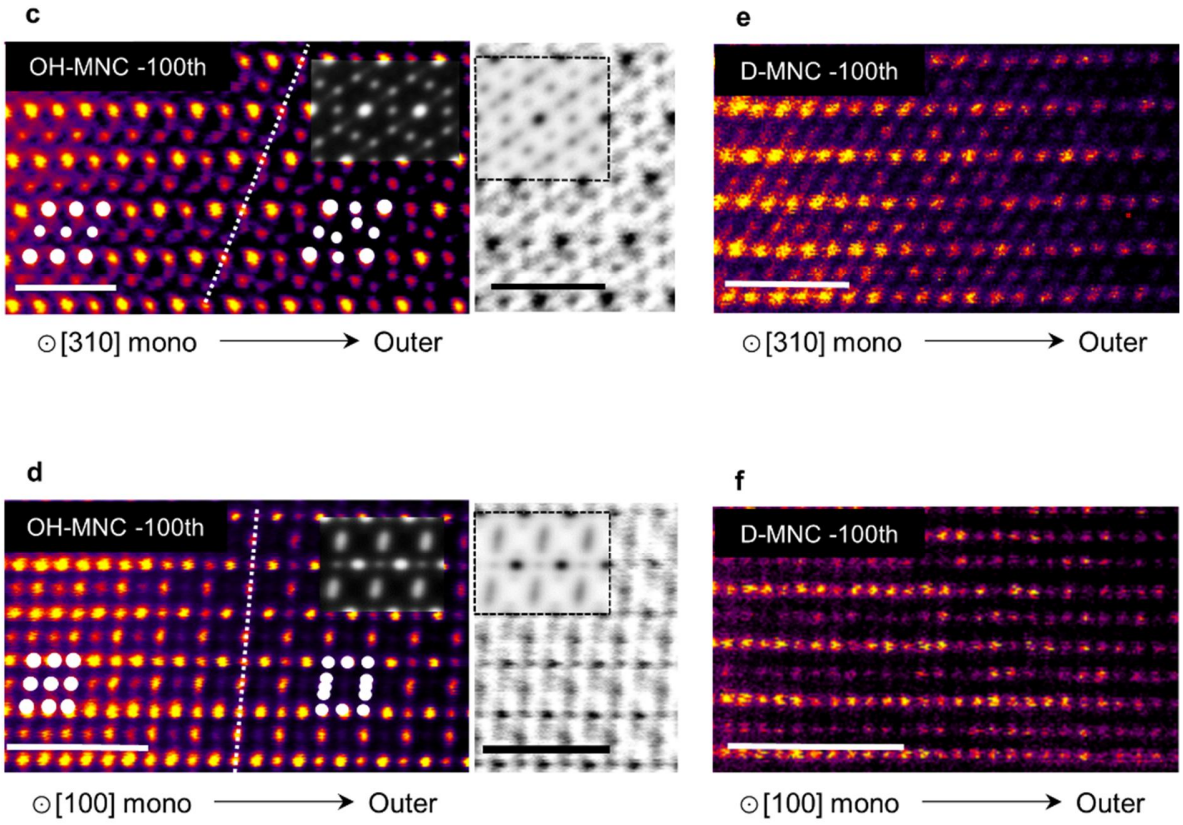


**Figure 3-19. Evolution of atomic structure.** HAADF-STEM image of the (**a**) $[100]_{mono}$ Pristine O-MNC (**b**) $[100]_{mono}$ Pristine O-MNC (**c**) $[310]_{mono}$ OH-MNC, (**d**) $[100]_{mono}$ OH-MNC**,** (**e**) $[310]_{mono}$ D-MNC and (**f**) $[100]_{mono}$ D-MNC particle after 100 charge-discharge cycles. Enlarged HAADF/ABF-STEM images of the surface region in images **c** and **d** with simulate HAADF/ABF-STEM images (in the inset) are presented; Scale bar denote 1nm.

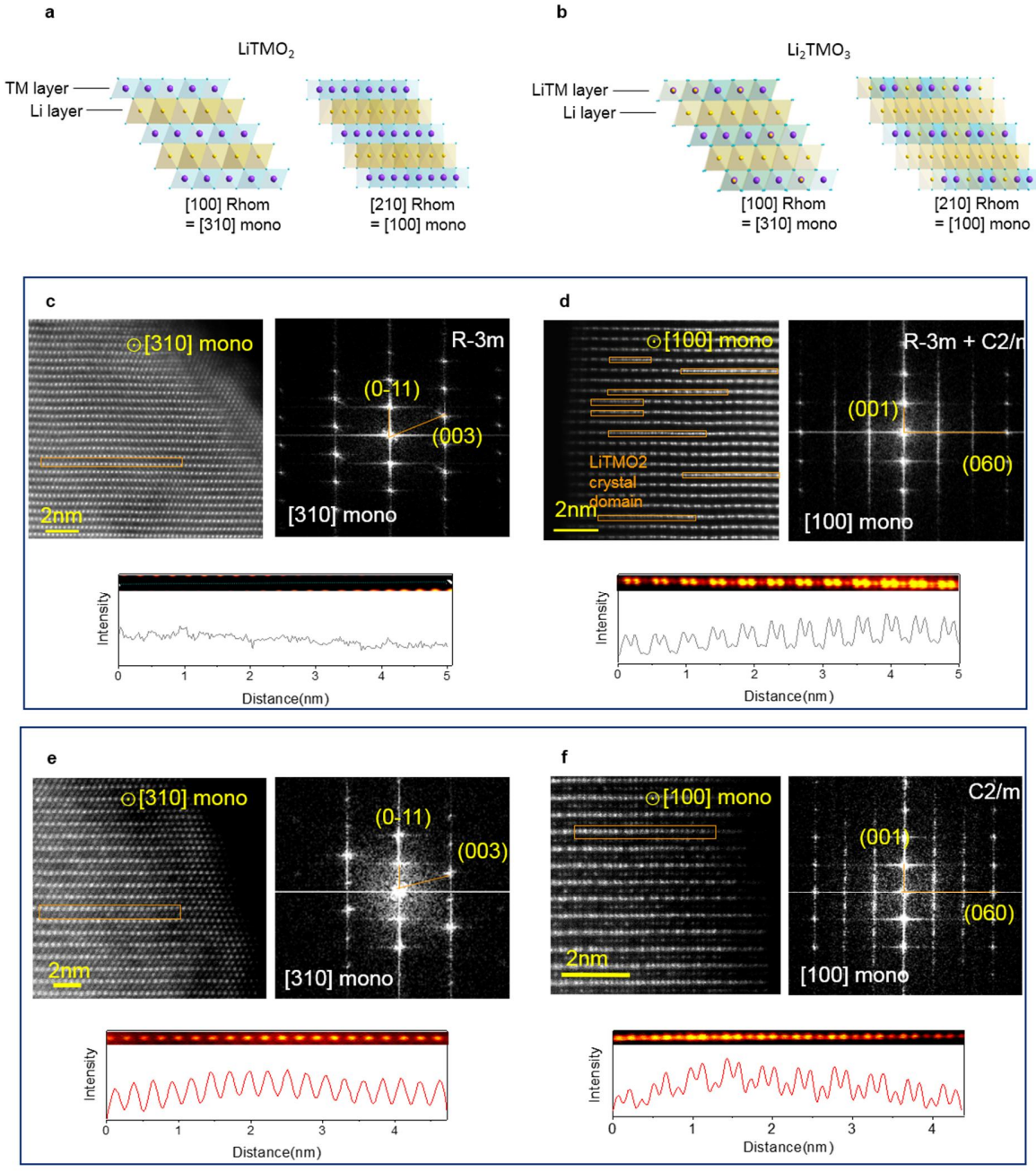


**Figure 3-20. Structure model of $LiTMO_2$ and $Li_2TMO_3$ phase which consist of Li-excess 3*d*-transition-metal oxide** a) $LiTMO_2$ phase b) $Li_2TMO_3$ phase along [310]mono and [100]mono zone axis**; HAADF-STEM images, FFT patterns and signal profile of pristine O-MNC and D-MNC samples along [310]mono and [100]mono zone axis.** c) O-MNC [310]mono d) O-MNC [100]mono e) D-MNC [310]mono f) D-MNC [100]mono.

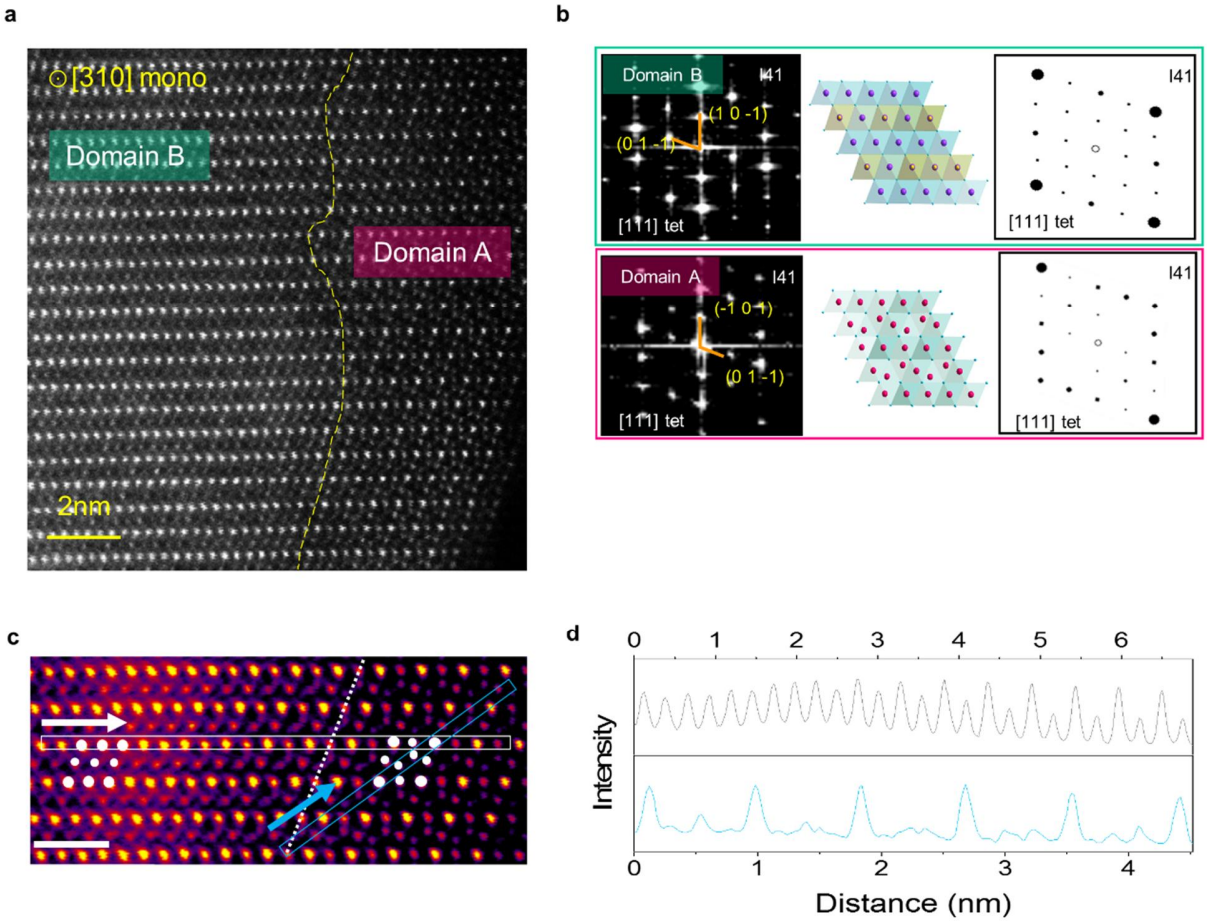


**Figure 3-21. Atomic structure analysis and identifying.** a) $[310]_{mono}$ direction HAADF-STEM image of $100^{th}$ cycled OH-MNC and b) collected FFT patterns were matched with simulated atomic structure model and simulated FFT pattern, respectively. c) Magnified HAADF-STEM image containing domain boundary. d) Signal profile of the region marked in grey and blue in image.

In order to clarify the crystal structure of domain A and B, FFT patterns and HAADF-STEM signal profile fitting revealing atomic distance were matched with simulated result by using atomic structure model. Domain A and B collected along $[310]_{mono}$ direction is well matched with simulated FFT patterns of tetragonal structure $LiMn_3O_4$ spinel-like phase and $Mn_3O_4$ spinel phase with I41 space group along $[111]_{tet}$ direction, respectively.

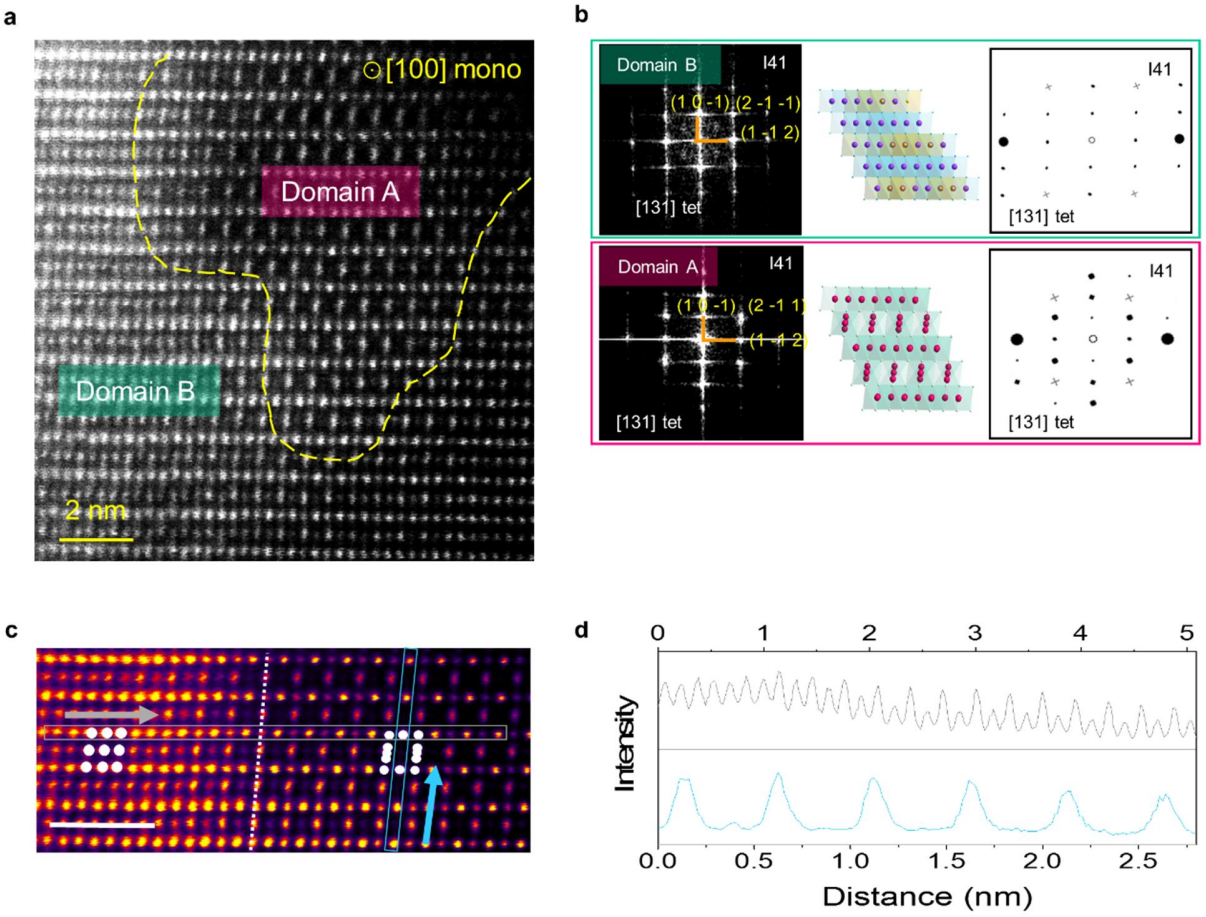


**Figure 3-22. Atomic structure analysis and identifying.** a) $[100]_{mono}$ direction HAADF-STEM image of $100^{th}$ cycled OH-MNC and b) collected FFT patterns were matched with simulated atomic structure model and simulated FFT pattern, respectively. c) Magnified HAADF-STEM image containing domain boundary. d) Signal profile of the region marked in grey and blue in image.

Simulated FFT patterns along $[131]_{tet}$ direction of $LiMn_3O_4$ spinel-like phase and $Mn_3O_4$ spinel phase is also well matched with collected FFT patterns of Domain A and Domain B which collected from HAADF-STEM image along $[100]_{mono}$ direction. HAADF-STEM signal peak of the region marked in grey and blue also well-matched with atomic distance of structure model.

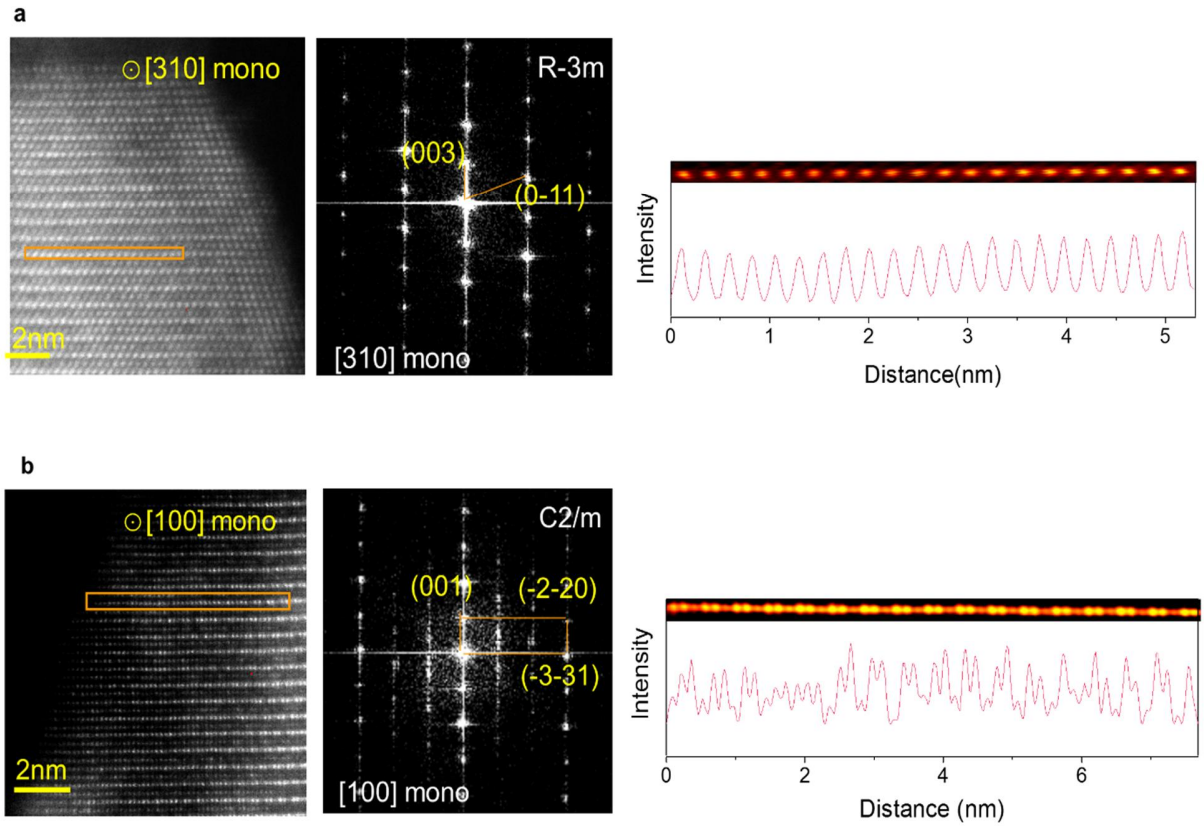


**Figure 3-23. HAADF-STEM images, FFT patterns and signal profile of 100th cycled D-MNC samples along [310]mono and [100]mono zone axis.** a) D-MNC [310]mono b) D-MNC [100]mono.

Interestingly, the pre-disordered structure of D-MNC is preserved without further phase transition even after 100 cycles compared to OH-MNC (**Fig. 3-19c, 3-19d and 3-23**). Furthermore, EDS analysis reveals the oxygen deficiency according to the distance from the outer surface (**Fig. 3-24 and 3-25**). O/TM ratio below 1.33 indicating $TM_3O_4$ phase was detected at a distance of ~23 nm from the surface of OH-MNC and within ~5 nm for D-MNC, consistent with the results of STXM. Continuous oxygen loss and consequent cation migration ($O_{TM}$ / $O_{LiTM} \rightarrow O_{Li} \rightarrow$ tetrahedral site) resulting in a three-step phase transition (Layered $\rightarrow$ $LiTM_3O_4$ phase $\rightarrow$ $TM_3O_4$ phase) in both $[310]_{mono}$ and $[100]_{mono}$ directions (**Fig. 3-26**). High efficient EDS spectrometer analysis were conducted to reveal the correlation between phase transition and oxygen deficiency. Comparing with the O/TM atomic ratio of pristine O-MNC and D-MNC according to the area mapping, the average ratio of pristine O-MNC and D-MNC are 2.238 and 2.145. These experimental values are remarkably similar to theoretical values calculated from O-MNC = $0.35(Li_2MnO_3)$-$0.65(LiMn_{0.38}Ni_{0.31}Co_{0.31}O_2)$ and D-MNC = $0.2(Li_2MnO_3)$-$0.8(LiMn_{0.5}Ni_{0.44}Co_{0.063}O_2)$ are 2.35 and 2.2, respectively. From this result, we deducted correction factors and calculated correction O/TM ratio of cycled OH-MNC: 2.11647 and D-MNC: 2.155897. Associating the normalized oxygen line mapping intensity data in supplementary figure with corrected O/TM ratio, the oxygen deficiency in accordance with the distance from outer-surface of $100^{th}$ cycled OH-MNC and D-MNC were demonstrated in color maps. In contrast to D-MNC, O/TM ratio below 1.33 were detected from outer-surface to 23nm in OH-MNC which suffered severe structural transition. Oxygen loss arose from redox mechanism and band structure of Li-excess 3*d*-transition-metal oxide leads cation disordering, which is accelerated at outer-surface directly reacted with electrolyte. Phase transition sequence from well-ordered layered to $TM_3O_4$ spinel phase with I41 space group observed in both $[310]_{mono}$ and $[100]_{mono}$ direction has direct correlation with oxygen deficiency (**Fig. 3-26**).

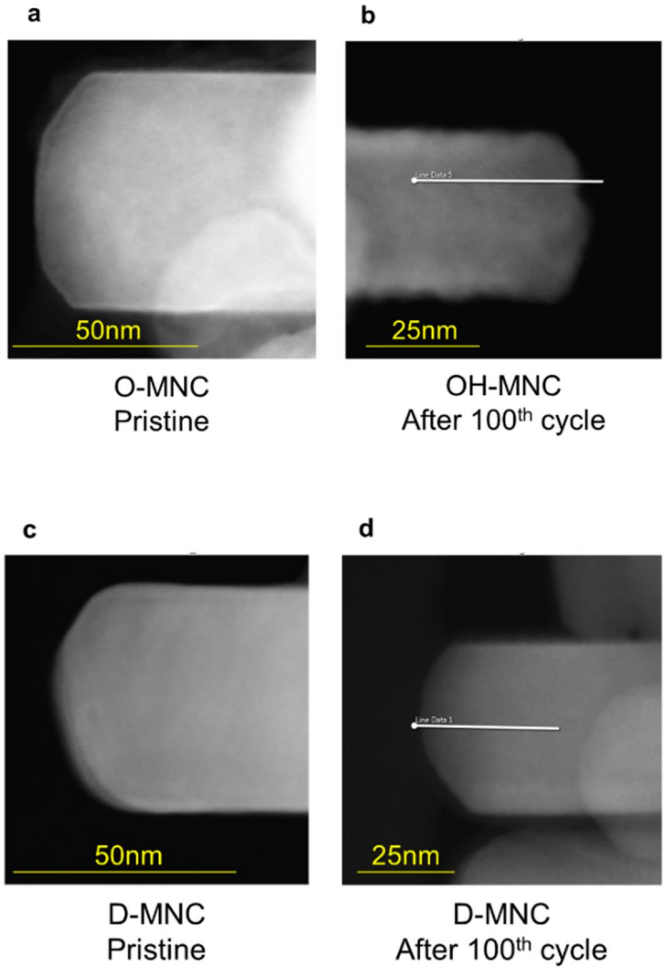


| Sample | **O-MNC Pristine** $Li_{1.15}Mn_{0.51}Ni_{0.17}Co_{0.17}O_2$ $0.35(Li_2MnO_3)$-$0.65(LiMn_{0.38}Ni_{0.31}Co_{0.31}O_2)$ | **D-MNC Pristine** $Li_{1.09}Mn_{0.550}Ni_{0.320}Co_{0.043}O_2$ $0.2(Li_2MnO_3)$-$0.8(LiMn_{0.5}Ni_{0.44}Co_{0.063}O_2)$ |
|---|---|---|
| **Theoretical value** | 2.350 | 2.200 |
| **Experimental value** | 2.238 | 2.145 |
| **correction factor** | 1.050 | 1.025 |
| Sample | **OH-MNC** after 100th cycle | **D-MNC** after 100th cycle |
| **Experimental value** | 2.0156 | 2.102 |
| **Theoretical value** | 2.116 | 2.156 |

**Figure 3-24. HR-TEM image of pristine O-MNC/D-MNC samples and 100th cycled OH-MNC/D-MNC for EDS mapping analysis.** Theoretical and experimental O/TM ratio result of pristine O-MNC/D-MNC and 100th cycled OH-MNC/D-MNC from EDS mapping analysis.

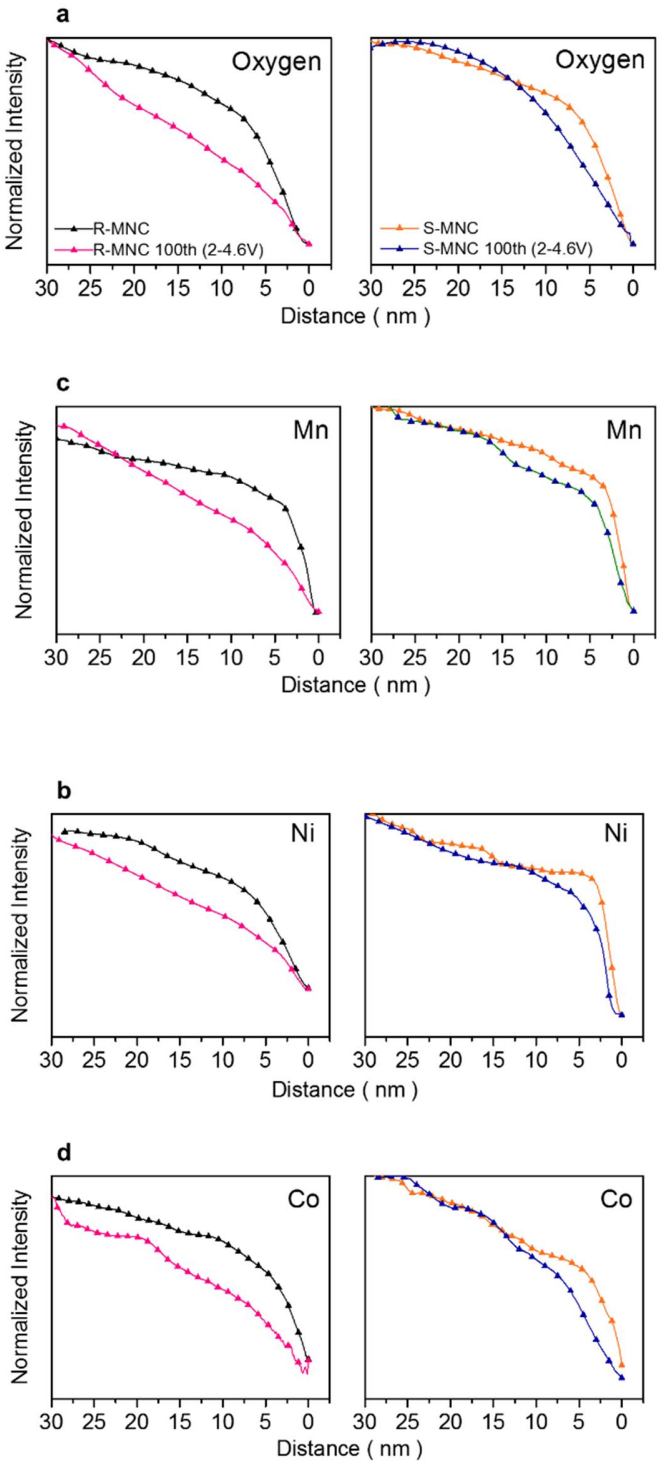


**Figure 3-25. EDS line scan signal counts of Pristine and 100$^{th}$ cycled OH-MNC /D-MNC samples.** Degree of elemental signal count change of a) Oxygen, b) Ni, c) Mn, and d) Co from outer-surface to 30nm.

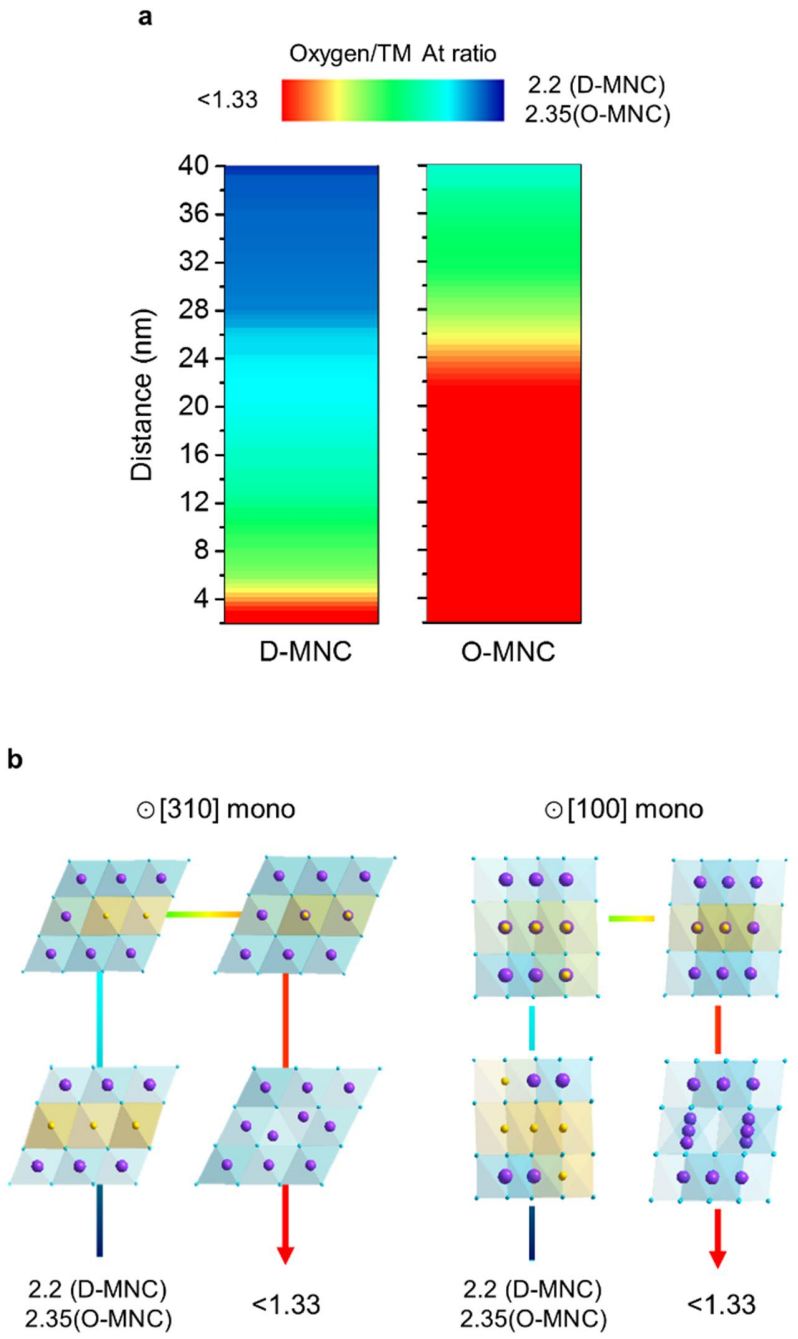


**Figure 3-26. Comparison of surface atomic rearrangement of OH-MNC and D-MNC on long cycling**. a) The image plot of oxygen ratio line mapping (30nm long) for cycled OH-MNC and D-MNC from surface region. The intensity represented as color scale bare shown on up. b) Schematic of surface structure rearrangement at $[310]_{mono}$ and $[100]_{mono}$ zone direction. Scale bar denote 1nm.

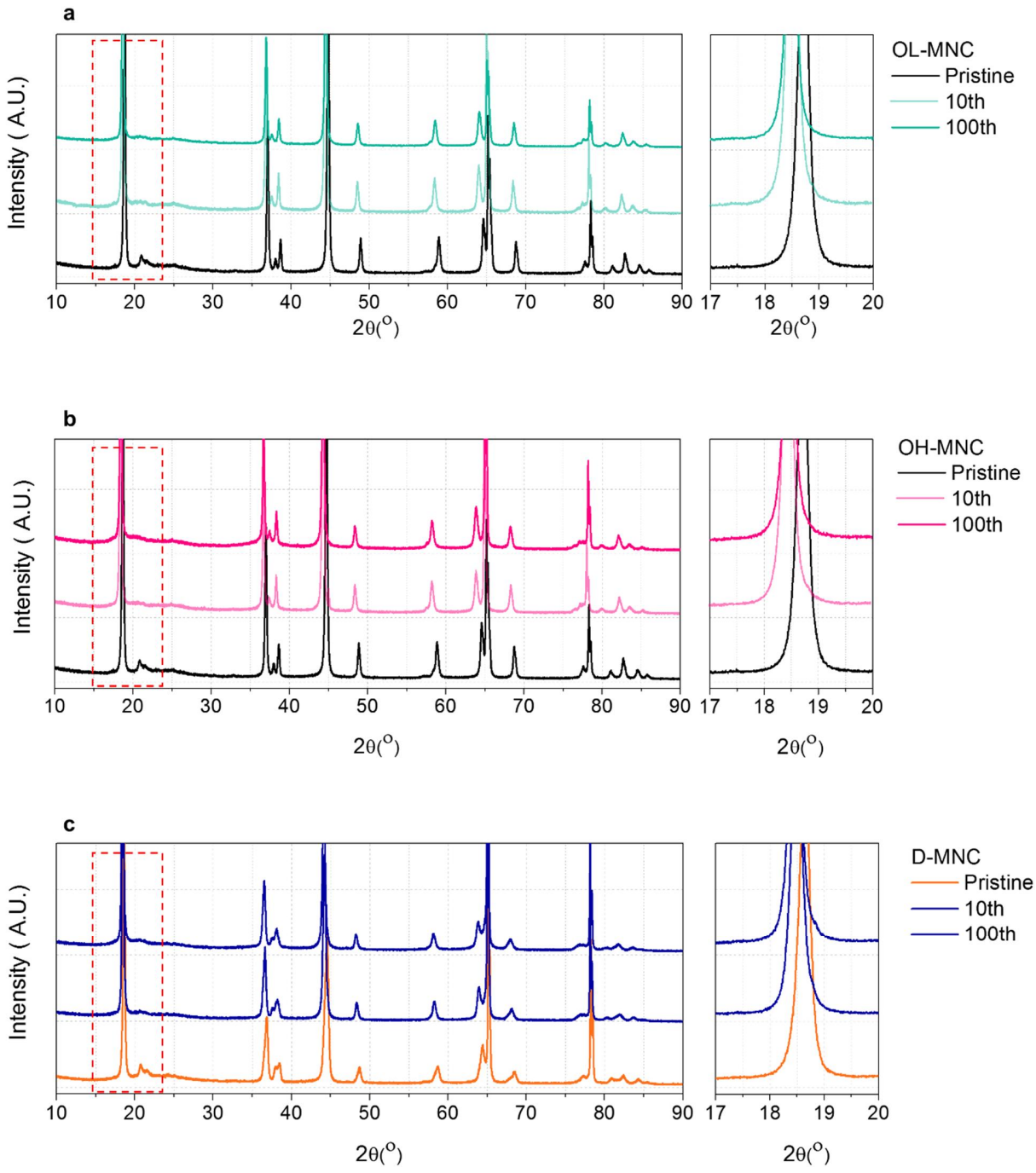


**Figure 3-27. Powder XRD pattern of pristine O-MNC, D-MNC and cycled samples (10 and 100 cycles).** a) OL-MNC, b) OH-MNC, and c) D-MNC.

**Atomic-selective structural analysis.** In order to reveal the relationship between atomic rearrangement and TM redox mechanism changes on prolonged cycling, XRD profiles and extended X-ray absorption fine structure (EXAFS) spectra were investigated. The XRD patterns of OL-MNC, OH-MNC, and D-MNC show significant peak shifts towards lower angles and the super-lattice peak disappears from their XRD profiles after 10 cycles. However, even if severe voltage decay is occurred in OH-MNC during 100 cycles, a slight peak shift towards lower angles is observed (**Fig. 3-27**). Although the XRD profiles reveal the expansion of lattice, they do not indicate mutual atomic arrangements and local atomic transitions around the specific TM related to voltage decay.

The radial distribution function (RDF) of the Mn, Ni, and Co K-edge $k^3\chi(k)$ EXAFS spectra providing local structure of a specific TM element was investigated and the interatomic distance was quantitatively analysed. Additionally, correlations between spectra peaks and structural information are schematically described in **Fig. 3-28**. Interestingly, the lower TM-A/C peak and higher TM-B peak were observed in pristine D-MNC than those of pristine O-MNC. This indicates that the pristine D-MNC structure has a relatively disordered arrangement in the TM and Li layer than the pristine O-MNC structure does (**Fig. 3-29**). After the 100$^{th}$ cycle, a significant decrease in Mn-O and Ni/Co-TM peaks were observed in 100$^{th}$-cycled OH-MNC compared with the OL-MNC (**Fig. 3-30a and 3-31**), which originated from irreversible Ni/Co ion migration (intra-layer to $O_{Li}$ in the inter-layer) and evolution of layered $MnO_2$-type structure caused by lithium extraction and oxygen loss from $Li_2MnO_3$ and $LiTMO_2$ phases.[146, 172-175] In contrast, overall peak features in all RDFs for D-MNC were relatively constant, compared with OH-MNC, indicating the relative preservation of TM local structure surrounded by oxygen and TM even during 100$^{th}$ cycle.

In order to investigate real-time structural variation and consequent atomic rearrangement after 10$^{th}$ and 100$^{th}$ cycle, the RDFs of TM-O and TM-A K-edge peak at all TM were plotted with a 2D contour map as a function of electrochemical reaction for clarity (**Fig. 3-30b and 3-30c**). During the charge-discharge, the 2D pattern intensities for each bonding pair in D-MNC keep a constant feature or become more intense from 10$^{th}$ to 100$^{th}$ cycle, while OH-MNC at 100$^{th}$ cycle distinctly shows a significant decrease in pattern intensity compared to OH-MNC at 10$^{th}$ cycle. The diminishing intensities in OH-MNC from 10$^{th}$ to 100$^{th}$ cycle indicate more oxygen loss from the lattice, less covalent bonding, and a static disorder of edge-shared TM coordination (ordered-to-disordered phase transformation). On the other hand, constant intensity of D-MNC for both 10$^{th}$ and 100$^{th}$ cycle reflects less oxygen loss from lattice and low possibility of cation disordering (disordered-to-disordered). Considering the RDFs, Soft-XAS, and XANES data in **Fig. 3-8**, we conclude that the stability of Mn-O bonding in Li-excessed 3*d*TM layered oxides is highly correlated with the overall reversibility of TM-O and immobilization of TM ion during cycling. Furthermore, maintenance of TM-O bonding and immobilization of TM ion in

D-MNC, especially Mn-O bonding and Ni/Co ion, is expected to highly affect the stable TM redox activity and the suppression of voltage decay during cycling, unlike in OH-MNC with ordered structure.

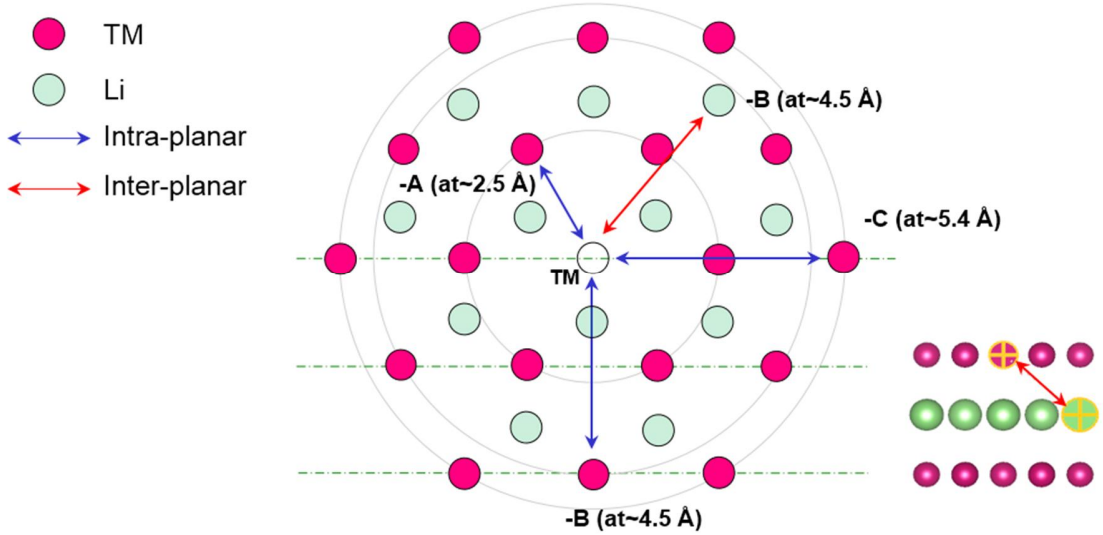


**Figure 3-28. Schematic diagram of scattering paths in the TM atomic arrangements within the ab plane.**[176] Schematic diagram shows the possible intra/inter-planar scattering paths in the TM atomic array within the ab plane. The peak at ~ 1.5 Å (TM-O) and ~2.5 Å (TM-A) corresponds to six-coordinated oxygen and TM of the nearest neighboring atom around the TM atom is important to determine the correct structural information, respectively. The peak of ~4.5 Å (TM-B) is mainly contributed from TM around at ~4.5 Å and substituted TM at Li sites located ~ 4.5 Å from TM. The peak of ~5.4 Å (TM-C) is mainly contributed from TM around at ~5.4 Å Moreover, significant variation has been observed in the higher FT peaks above ~4.0 Å which shows useful structural information for Li-excess 3*d*-transition metal oxides.

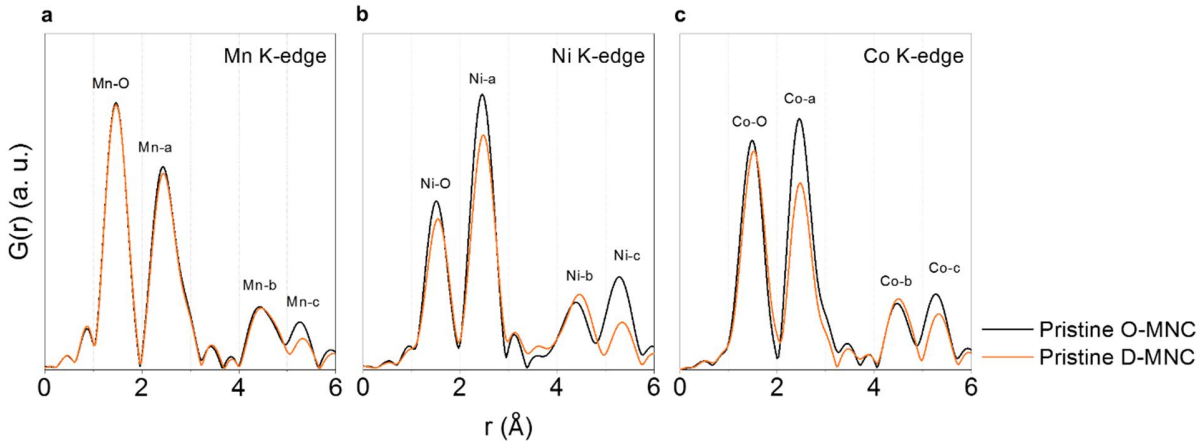


**Figure 3-29. Radial distribution function (RDF) of (a) Mn, (b) Ni, and (c) Co K-edge k3-weighted EXAFS spectra as a function of interatomic distance for pristine electrode of OH-MNC and D-MNC.** Pristine O-MNC and D-MNC, show higher Mn-O peak intensity than Mn-A peak, which is typical EXAFS data at the Mn K-edge. This feature originates from the specific structure of Li-excess 3*d*-transition-metal oxide which has $Li_2MnO_3$ and $LiTMO_2$ domains.[177]

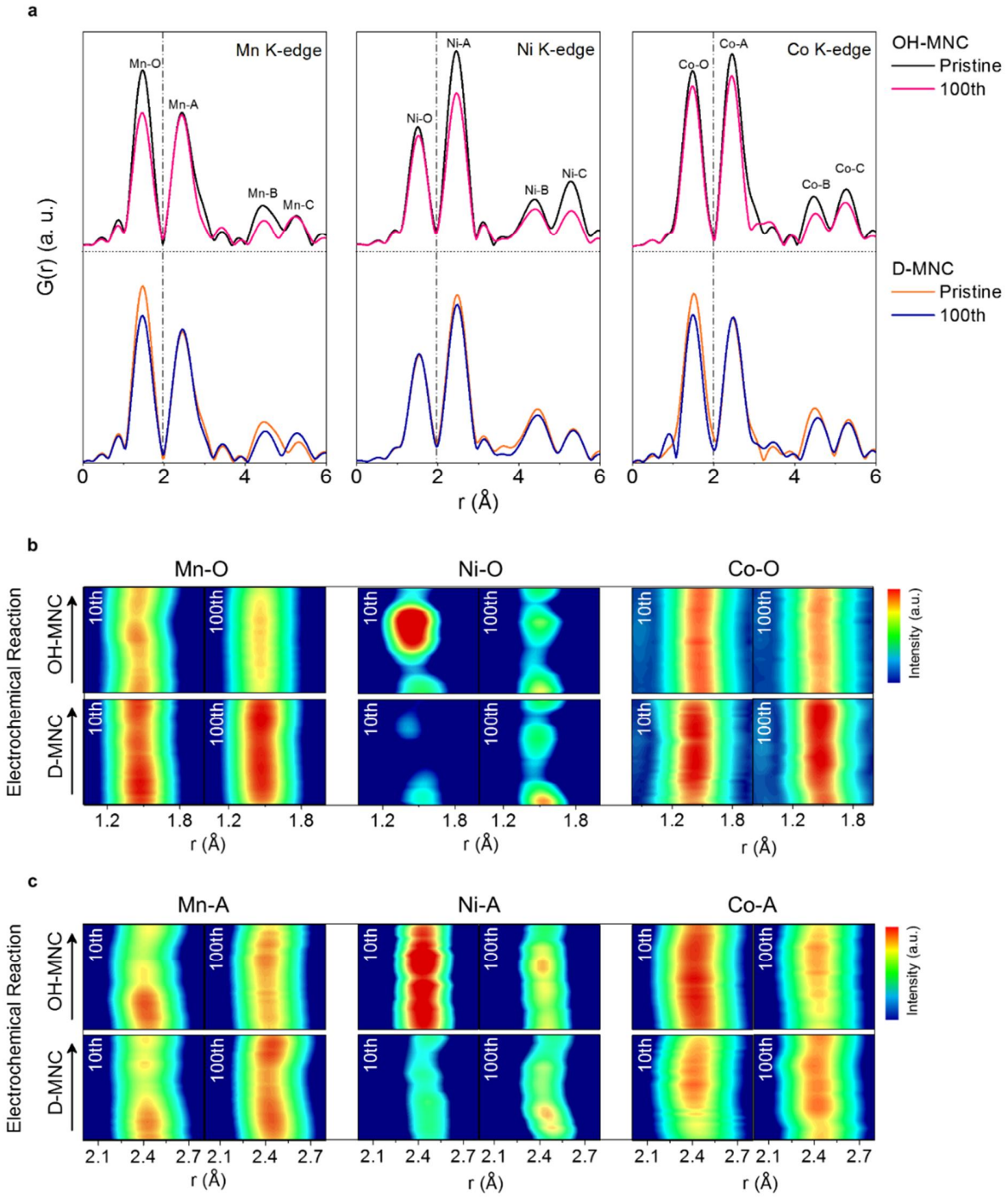


**Figure 3-30. Migration of specific elements due to the structural instability.** (**a**) Radial distribution function (RDF) of Mn, Ni, and Co K-edges $k^3$-weighted EXAFS spectra for pristine and 100$^{th}$ cycled electrode of OH-MNC and D-MNC; Comparison of OH-MNC and D-MNC K-edge o*perando* EXAFS spectra (2D contour plot) collected during 10$^{th}$ and 100$^{th}$ cycle. Spectra represents (**b**) TM-O peak and (**c**) TM-A peak variation of Mn, Ni, and Co K-edges.

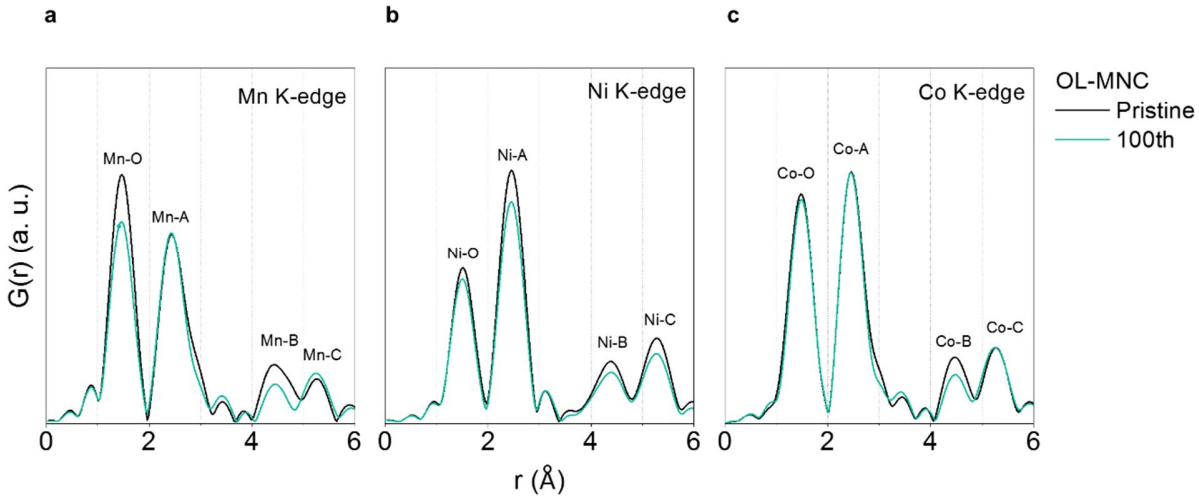


**Figure 3-31.** Radial distribution function (RDF) of (a) Mn, (b) Ni, and (c) Co K-edge k3-weighted EXAFS spectra as a function of interatomic distance for Pristine O-MNC, $10^{th}$ cycled and $100^{th}$ cycled electrode of OL-MNC.

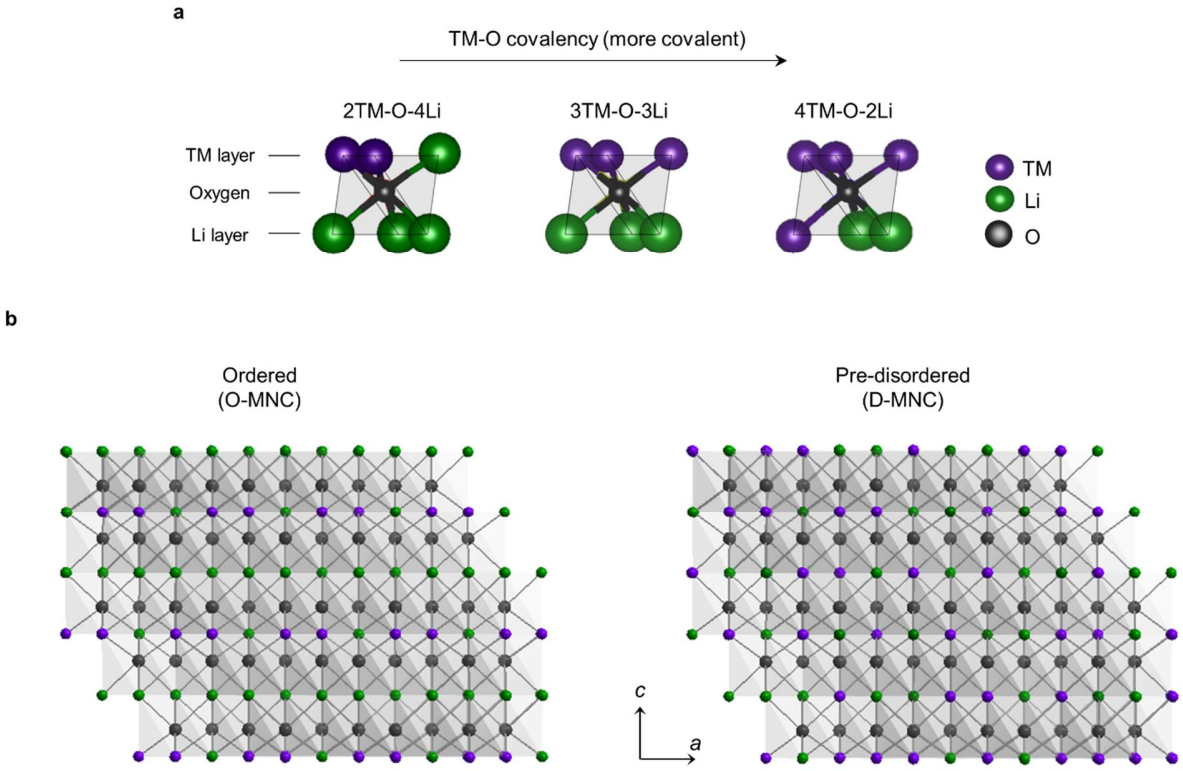


**Figure 3-32.** Oxygen-centred structure model of pristine O-MNC and D-MNC (**a**) Three oxygen-centred octahedron ($M_6O$) of Li-excess material. Each oxygen anions coordinated by six cations with different portion of $Li^+$ and transition-metal in TM and Li layer. 2TM-O-4Li, 3TM-O-3Li and 4TM-O-2Li octahedron represent the base structure of $Li_2TMO_3$, $LiTMO_2$ and disordered-$LiTMO_2$ (**b**) Oxygen-centred macroscopic structure model of pristine O-MNC and D-MNC along $[100]_{mono}$.

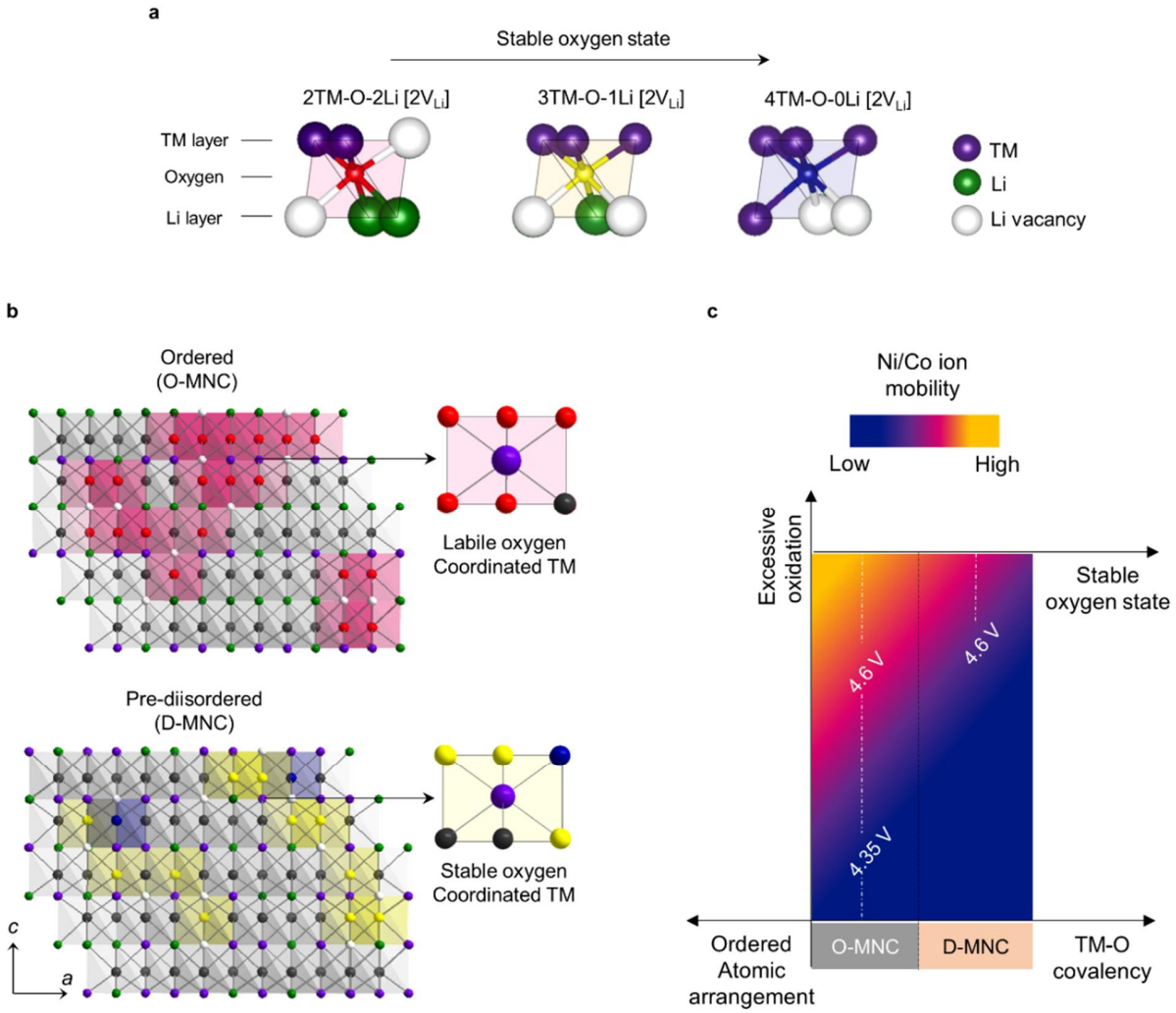


**Figure 3-33. Factors to consider in interpreting the structural stability of high capacity cathode material.** (**a**) Three de-lithiated oxygen-centred octahedron ($M_4O$) of Li-excess material. Each oxygen anions coordinated by four cations and two lithium vacancies ($V_{Li}$) with different portion of $Li^+$ and transition-metal in TM and Li layer. 2TM-O-2Li [2$V_{Li}$], 3TM-O-1Li [2$V_{Li}$] and 4TM-O-0Li [2$V_{Li}$] octahedron represent the base structure of de-lithiated $Li_2TMO_3$, $LiTMO_2$ and pre-disordered-$LiTMO_2$, and the degree of stability on centred oxygen represented as different color (Red is highly labile); (**b**) Oxygen-centred macroscopic structure model of de-lithiated state OH-MNC and D-MNC along $[100]_{mono}$ (**c**) Schematic of structure stability according to the material characteristics and electrochemical conditions.

**How atomic arrangement affect structure stability of Li-excess material.** Based on the multilateral analysis results, we described oxygen-centred macroscopic structure models of OH-MNC and D-MNC with three types of de-lithiated $M_6O$ octahedron ($M_4O$) to explain the fundamental reason for the difference in oxygen stability and structural reversibility according to atomic arrangement (**Fig. 3-32a**). Each $O^{2-}$ ion is coordinated by four cations and two lithium vacancies ($V_{Li}$) with different portion of $Li^+$ and transition-metal in TM and Li layer. 2TM-O-2Li [$2V_{Li}$], 3TM-O-1Li [$2V_{Li}$] and 4TM-O-0Li [$2V_{Li}$] models represent the base structures of de-lithiated $C2/m$, $R\bar{3}m$, and pre-disordered $R\bar{3}m$, respectively (**Fig. 3-32a**). High number of TM around oxygen increases the O2$p$-TM3$dt_{2g}$ orbital hybridization and decreases the possibility of holes localization on the oxygen sites at charged states compare to high number of Li around oxygen.[28, 29]

Microscopic structural analysis along $[310]_{mono}$ and $[100]_{mono}$ directions and EXAFS spectra revealed that O-MNC with a well-ordered structure has long-range ordering of 2TM-O-4Li octahedron. In contrast, 2TM-O-4Li ordering is broken in D-MNC because the pre-disordered cations in the Li layer form 3TM-O-3Li and 4TM-O-2Li octahedrons in the $[100]_{mono}$ structure (**Fig. 3-33**). At de-lithiated state, the presence of 4TM-O-0Li [$2V_{Li}$] octahedrons in structure increases the possibility of hole delocalization on oxygen related with low oxidation number and high covalency of TM-O bonding in D-MNC. In perspective of cation, stable oxygen resulting from short-range ordered 2TM-O-2Li [$2V_{Li}$] octahedron is coordinated around the TM of D-MNC unlike in OH-MNC (**Fig. 3-32b**). High-voltage condition causes excessive oxidation of TM in the structure, resulting in more oxygen loss on TM-O bonding, especially $Mn^{3.65+}$-O bonding (less covalent) compared to $Ni^{3.08+}$/$Co^{2.98+}$-O bonding. When charge compensation is continuously repeated, series of oxygen loss occurs from overall TM-O bonding, and Ni/Co cation migration is preferentially occurred in the ordered structure of OH-MNC than in the pre-disordered structure of D-MNC (**Fig. 3-32c**).

**Conclusions**

Structural arrangement with de-lithiated oxygen-centred octahedron ($M_4O$) and interactions between those octahedrons are important reasons for Li-excess material degradation. By combining spectroscopy and microscopy techniques, we reveal that the cation distribution in Li and TM layers determines the ordering of octahedron ($M_6O$) and different TM-O bonding covalency. At charged state, numbers of labile oxygen (high possibility of hole localization) arisen from excess oxidation of well-ordered $Li_2TMO_3$ phase leads to decrease of TM-O bonding covalency, especially Mn-O bonding, resulting in oxygen loss from lattice and irreversibility of the overall TM-O bonding. In particularly, Ni/Co ions surrounded with labile oxygens and oxygen vacancies significantly migrate into Li vacancies, and consequently causes 'layered to $TM_3O_4$' phase transition during the cycling. These features finally bring about the inactive-redox and active-redox reaction in Ni/Co and Mn, respectively, causing the voltage decay phenomenon. By comparing ordered and pre-disordered Li-excess 3dTM material, we advance the basic understanding of voltage decay phenomenon, in terms of de-lithiated oxygen-centred octahedron($M_4O$), and propose candidate structure model to suppress voltage decay, having partially distributed pre-disordered site, not a well-ordered structure.

## References


1. Goodenough JB, Abruña HD, Buchanan MV, Visco S, Whittingham MS, Dunn B, *et al.* Report of the Basic Energy Sciences Workshop on Electrical Energy Storage. **2007,** http://web.anl.gov/energy-storage-science/publications/EES_rpt.pdf.

2. Whittingham MS. History, Evolution, and Future Status of Energy Storage. *Proc. IEE* **2012,** 100, 1518-1534.

3. Lu Z, Dahn JR. Understanding the Anomalous Capacity of Li/Li[$Ni_xLi_{(1/3-2x/3)}Mn_{(2/3-x/3)}$]$O_2$ Cells Using In Situ X-Ray Diffraction and Electrochemical Studies. *J. Electrochem. Soc.* **2002,** 149, A815-A822.

4. Kang SH, Amine K. Layered Li($Li_{0.2}Ni_{0.15+0.5z}Co_{0.10}Mn_{0.55-0.5z}$)$O_{2-z}F_z$ cathode materials for Li-ion secondary batteries. *J. Power Sources* **2005,** 146, 654-657.

5. Thackeray MM, Johnson CS, Vaughey JT, Li N, Hackney SA. Advances in manganese-oxide composite electrodes for lithium-ion batteries. *J. Mater. Chem.* **2005,** 15, 2257-2267.

6. Armstrong AR, Holzapfel M, Novák P, Johnson CS, Kang S-H, Thackeray MM, *et al.* Demonstrating Oxygen Loss and Associated Structural Reorganization in the Lithium Battery Cathode Li[$Ni_{0.2}Li_{0.2}Mn_{0.6}$]$O_2$. *J. Am. Chem. Soc.* **2006,** 128, 8694.

7. Thackeray MM, Kang S-H, Johnson CS, Vaughey JT, Benedek R, Hackney SA. $Li_2MnO_3$-stabilized $LiMO_2$ (M=Mn, Ni, Co) electrodes for lithium-ion batteries. *J. Mater. Chem.* **2007,** 17, 3112-3125.

8. Yabuuchi N, Yoshii K, Myung ST, Nakai I, Komaba S. Detailed Studies of a High-Capacity Electrode Material for Rechargeable Batteries, Li(2)MnO(3)-LiCo(1/3)Ni(1/3)Mn(1/3)O(2). *J. Am. Chem. Soc.* **2011,** 133, 4404-4419.

9. Sun Y-K, Lee M-J, Yoon CS, Hassoun J, Amine K, Scrosati B. The Role of $AlF_3$ Coatings in Improving Electrochemical Cycling of Li-Enriched Nickel-Manganese Oxide Electrodes for Li-Ion Batteries. *Adv. Mater.* **2012,** 24, 1192-1196.

10. Yu H, Zhou H. High-Energy Cathode Materials ($Li_2MnO_3$–$LiMO_2$) for Lithium-Ion Batteries. *J. Phys. Chem. Lett.* **2013,** 4, 1268.

11. Hong J, Gwon H, Jung S-K, Ku K, Kang K. Review—Lithium-Excess Layered Cathodes for Lithium Rechargeable Batteries. *J. Electrochem. Soc.* **2015,** 162, A2447-A2467.

12. Rozier P, Tarascon JM. Review—Li-Rich Layered Oxide Cathodes for Next-Generation Li-Ion Batteries: Chances and Challenges. *J. Electrochem. Soc.* **2015,** 162, A2490-A2499.

13. Ye DL, Wang LZ. $Li_2MnO_3$ based Li-rich cathode materials: towards a better tomorrow of high energy lithium ion batteries. *Mater. Technol.* **2014,** 29, A59-A69.

14. Johnson CS, Kim JS, Lefief C, Li N, Vaughey JT, Thackeray MM. The significance of the $Li_2MnO_3$ component in 'composite' $xLi_2MnO_3 \cdot (1\text{-}x)LiMn_{0.5}Ni_{0.5}O_2$ electrodes. *Electrochem. Commun.* **2004,** 6, 1085-1091.

15. Lee DK, Park SH, Amine K, Bang HJ, Parakash J, Sun YK. High capacity $Li[Li_{0.2}Ni_{0.2}Mn_{0.6}]O_2$ cathode materials via a carbonate co-precipitation method. *J. Power Sources* **2006,** 162, 1346-1350.

16. Lim J-H, Bang H, Lee K-S, Amine K, Sun Y-K. Electrochemical characterization of $Li_2MnO_3$–$Li[Ni_{1/3}Co_{1/3}Mn_{1/3}]O_2$–$LiNiO_2$ cathode synthesized via co-precipitation for lithium secondary batteries. *J. Power Sources* **2009,** 189, 571-575.

17. Choi N-S, Chen Z, Freunberger SA, Ji X, Sun Y-K, Amine K*, et al.* Challenges Facing Lithium Batteries and Electrical Double-Layer Capacitors. *Angew. Chem. Int. Ed.* **2012,** 51, 9994-10024.

18. Zheng J, Gu M, Xiao J, Zuo P, Wang C, Zhang J-G. Corrosion/Fragmentation of Layered Composite Cathode and Related Capacity/Voltage Fading during Cycling Process. *Nano Lett.* **2013,** 13, 3824.

19. Robertson AD, Bruce PG. Mechanism of Electrochemical Activity in $Li_2MnO_3$. *Chem. Mater.* **2003,** 15, 1984-1992.

20. Xu B, Fell CR, Chi M, Meng YS. Identifying surface structural changes in layered Li-excess nickel manganese oxides in high voltage lithium ion batteries: A joint experimental and theoretical study. *Energy Environ. Sci.* **2011,** 4, 2223.

21. Wu Y, Ma C, Yang J, Li Z, Allard LF, Liang C*, et al.* Probing the initiation of voltage decay in Li-rich layered cathode materials at the atomic scale. *J. Mater. Chem. A* **2015,** 3, 5385-5391.

22. Lu Z, Dahn JR. Understanding the Anomalous Capacity of $Li/Li[Ni_xLi_{(1/3-2x/3)}Mn_{(2/3-x/3)}]O_2$ Cells Using In Situ X-Ray Diffraction and Electrochemical Studies. *J. Electrochem. Soc.* **2002,** 149, A815–A822.

23. Tran N, Croguennec L, Ménétrier M, Weill F, Biensan P, Jordy C*, et al*. Mechanisms Associated with the "Plateau" Observed at High Voltage for the Overlithiated $Li_{1.12}(Ni_{0.425}Mn_{0.425}Co_{0.15})_{0.88}O_2$ System. *Chem. Mater.* **2008,** 20, 4815–4825.

24. Croy JR, Gallagher KG, Balasubramanian M, Chen Z, Ren Y, Kim D*, et al.* Examining Hysteresis in Composite $xLi_2MnO_3\cdot(1-x)LiMO_2$ Cathode Structures. *J. Phys. Chem. C* **2013,** 117, 6525–6536.

25. Yu X, Lyu Y, Gu L, Wu H, Bak S-M, Zhou Y*, et al.* Understanding the Rate Capability of High-Energy-Density Li-Rich Layered Li1.2Ni0.15Co0.1Mn0.55O2 Cathode Materials. *Adv. Energy Mater.* **2014,** 4, DOI: 10.1002/aenm.201300950.

26. Fell CR, Qian D, Carroll KJ, Chi M, Jones JL, Meng YS. Correlation Between Oxygen Vacancy, Microstrain, and Cation Distribution in Lithium-Excess Layered Oxides During the First Electrochemical Cycle. *Chem. Mater.* **2013,** 25, 1621–1629.

27. Boulineau A, Simonin L, Colin J-F, Bourbon C, Patoux S. First Evidence of Manganese–Nickel Segregation and Densification upon Cycling in Li-Rich Layered Oxides for Lithium Batteries. *Nano Lett.* **2013,** 13, 3857-3863.

28. Zheng J, Gu M, Xiao J, Polzin BJ, Yan P, Chen X*, et al.* Functioning Mechanism of $AlF_3$ Coating on the Li-and Mn-Rich Cathode Materials. *Chem. Mater.* **2014,** 26, 6320–6327.

29. Boulineau A, Simonin L, Colin J-F, Canévet E, Daniel L, Patoux S. Evolutions of $Li_{1.2}Mn_{0.61}Ni_{0.18}Mg_{0.01}O_2$ during the Initial Charge/Discharge Cycle Studied by Advanced Electron Microscopy. *Chem. Mater.* **2012,** 24, 3558–3566.

30. Mohanty D, Sefat AS, Li J, Meisner RA, Rondinone AJ, Payzant EA*, et al.* Correlating cation ordering and voltage fade in a lithium-manganese-rich lithium-ion battery cathode oxide: a joint magnetic susceptibility and TEM study. *Phys. Chem. Chem. Phys.* **2013,** 15, 19496–19509.

31. Mohanty D, Li J, Nagpure SC, Wood DLI, Daniel C. Understanding the structure and structural degradation mechanisms in high-voltage, lithium-manganese–rich lithium-ion battery cathode oxides: A review of materials diagnostics. *MRS Energy & Sustainability - A Review Journal* **2015,** 2, doi:10.1557/mre.2015.1516.

32. Oh P, Ko M, Myeong S, Kim Y, Cho J. A Novel Surface Treatment Method and New Insight into Discharge Voltage Deterioration for High-Performance $0.4Li_2MnO_3–0.6LiNi_{1/3}Co_{1/3}Mn_{1/3}O_2$ Cathode Materials. *Adv. Energy Mater.* **2014,** 4, 201400631.

33. Zheng J, Xu P, Gu M, Xiao J, Browning ND, Yan P*, et al.* Structural and Chemical Evolution of Li- and Mn-rich Layered Cathode Material. *Chem. Mater.* **2015,** 27, 1381–1390.

34. Yan P, Nie A, Zheng J, Zhou Y, Lu D, Zhang X*, et al.* Evolution of Lattice Structure and Chemical Composition of the Surface Reconstruction Layer in $Li_{1.2}Ni_{0.2}Mn_{0.6}O_2$ Cathode Material for Lithium Ion Batteries. *Nano Lett.* **2015,** 15, 514-522.

35. Urban A, Lee J, Ceder G. The Configurational Space of Rocksalt-Type Oxides for High-Capacity Lithium Battery Electrodes. *Adv. Energy Mater.* **2014,** 4, DOI: 10.1002/aenm.201400478.

36. Urban A, Lee J, Ceder G. The Configurational Space of Rocksalt-Type Oxides for High-Capacity Lithium Battery Electrodes. *Adv. Energy Mater.* **2014,** 4, 201400478.

37. Wu Y, Manthiram A. Effect of surface modifications on the layered solid solution cathodes (1-z)$Li[Li_{1/3}Mn_{2/3}]O_2$ − (z)$Li[Mn_{0.5-y}Ni_{0.5-y}Co_{2y}]O_2$. *Solid State Ionics* **2009,** 180, 50-56.

38. Croy JR, Kim D, Balasubramanian M, Gallagher K, Kang S-H, Thackeray MM. Countering the Voltage Decay in High Capacity xLi2MnO3●(1–x)LiMO2 Electrodes (M=Mn, Ni, Co) for Li+-Ion Batteries. *J Electrochem Soc* **2012,** 159, A781.

39. Kim D, Croy JR, Thackeray MM. Comments on stabilizing layered manganese oxide electrodes for Li batteries. *Electrochem. Commun.* **2013,** 36, 103-106.

40. Croy JR, Gallagher KG, Balasubramanian M, Long BR, Thackeray MM. Quantifying Hysteresis and Voltage Fade in xLi2MnO3bullet(1-x)LiMn0.5Ni0.5O2 Electrodes as a Function of Li2MnO3 Content. *J. Electrochem. Soc.* **2013,** 161, A318-A325.

41. Hong Y-S, Park YJ, Ryu KS, Chang SH. Charge/discharge behavior of $Li[Ni_{0.20}Li_{0.20}Mn_{0.60}]O_2$ and $Li[Co_{0.20}Li_{0.27}Mn_{0.53}]O_2$ cathode materials in lithium secondary batteries. *Solid State Ionics* **2005,** 176, 1035-1042.

42. Hong Y-S, Park YJ, Ryu KS, Chang SH, Shin Y-J. Structural and electrochemical properties of (1−x) $Li[Ni_{0.20}Li_{0.20}Mn_{0.60}]O_2$–x$Li[Co_{0.50}Li_{0.167}Mn_{0.333}]O_2$ for lithium secondary batteries. *J. Power Sources* **2005,** 147, 214-219.

43. Fell CR, Carroll KJ, Chi M, Meng YS. Synthesis–Structure–Property Relations in Layered, "Li-excess" Oxides Electrode Materials $Li[Li_{1/3-2x/3}Ni_xMn_{2/3-x/3}]O_2$ (x=1/3, 1/4, and 1/5). *J. Electrochem. Soc.* **2010,** 157, A1202-A1211.

44. Meng YS, Ceder G, Grey CP, Yoon WS, Jiang M, Bréger J*, et al.* Cation Ordering in Layered O3 $Li[Ni_xLi_{1/3-2x/3}Mn_{2/3-x/3}]O_2(0\leq x\leq 1/2)$ Compounds. *Chem. Mater.* **2005,** 17, 2386-2394.

45. Lu ZH, Beaulieu LY, Donaberger RA, Thomas CL, Dahn JR. Synthesis, structure, and electrochemical behavior of $Li[Ni_xLi_{1/3-2x/3}Mn_{2/3-x/3}]O_2$. *J. Electrochem. Soc.* **2002,** 149, A778-A791.

46. Kobayashi H, Sakaebe H, Kageyama H, Tatsumi K, Arachi Y, Kamiyama T. Changes in the structure and physical properties of the solid solution $LiNi_{1-x}Mn_xO_2$ with variation in its composition. *J. Mater. Chem.* **2003,** 13, 590-595.

47. Yan PF, Zheng JM, Lv DP, Wei Y, Zheng JX, Wang ZG, *et al.* Atomic-Resolution Visualization of Distinctive Chemical Mixing Behavior of Ni, Co, and Mn with Li in Layered Lithium Transition-Metal Oxide Cathode Materials. *Chem. Mater.* **2015,** 27, 5393-5401.

48. Zheng J, Gu M, Genc A, Xiao J, Xu P, Chen X, *et al.* Mitigating Voltage Fade in Cathode Materials by Improving the Atomic Level Uniformity of Elemental Distribution. *Nano Lett.* **2014,** 14, 2628–2635.

49. Li Y, Bai Y, Wu C, Qian J, Chen G, Liu L, *et al.* Three-Dimensional Fusiform Hierarchical Micro/Nano $Li_{1.2}Ni_{0.2}Mn_{0.6}O_2$ with Preferred Orientation (110) Plane as High Energy Cathode Material for Lithium-Ion Batteries. *J. Mater. Chem. A* **2016**.

50. Nayak PK, Grinblat J, Levi M, Levi E, Kim S, Choi JW, *et al.* Al Doping for Mitigating the Capacity Fading and Voltage Decay of Layered Li and Mn-Rich Cathodes for Li-Ion Batteries. *Adv. Energy Mater.* **2016,** n/a-n/a.

51. Zhang T, Li J-t, Liu J, Deng Y-p, Wu Z-g, Yin Z-w, *et al.* Suppressing the voltage-fading of layered lithium-rich cathode materials via an aqueous binder for Li-ion batteries. *Chem. Commun.* **2016,** 52, 4683-4686.

52. Wei Z, Zhang W, Wang F, Zhang Q, Qiu B, Han S, *et al.* Eliminating Voltage Decay of Lithium-Rich $Li_{1.14}Mn_{0.54}Ni_{0.14}Co_{0.14}O_2$ Cathodes by Controlling the Electrochemical Process. *Chem. Eur. J.* **2015,** 21, 7503-7510.

53. Ito A, Li D, Sato Y, Arao M, Watanabe M, Hatano M, *et al.* Cyclic deterioration and its improvement for Li-rich layered cathode material $Li[Ni_{0.17}Li_{0.2}Co_{0.07}Mn_{0.56}]O_2$. *J. Power Sources* **2010,** 195, 567-573.

54. Gu M, Belharouak I, Genc A, Wang D, Wang Z, Amine K, *et al.* Conflicting Roles of Ni in Controlling Cathode Performance in Li-ion Batteries. *Nano Lett.* **2012,** 12, 5186-5191.

55. Bareño J, Lei CH, Wen JG, Kang SH, Petrov I, Abraham DP. Local Structure of Layered Oxide Electrode Materials for Lithium-Ion Batteries. *Adv. Mater.* **2010,** 22, 1122-1127.

56. Xu W, Chen X, Ding F, Xiao J, Wang D, Pan A, *et al.* Reinvestigation on the state-of-the-art nonaqueous carbonate electrolytes for 5 V Li-ion battery applications. *J. Power Sources* **2012,** 213, 304.

57. Zheng X, Wang X, Qiu Y, Li Y, Zhou C, Sui Y, *et al.* One-Electron Oxidation of an Organic Molecule by $B(C_6F_5)_3$; Isolation and Structures of Stable Non-para-substituted Triarylamine Cation Radical and Bis(triarylamine) Dication Diradicaloid. *J. Am. Chem. Soc.* **2013,** 135, 14912–14915.

58. Jarvis KA, Deng Z-Q, Allard LF, Manthiram A, Ferreira PJ. Atomic Structure of a Lithium-Rich Layered Oxide Material for Lithium-Ion Batteries: Evidence of a Solid Solution. *Chem. Mater.* **2011,** 23, 3614-3621.

59. Yu H, Ishikawa R, So Y-G, Shibata N, Kudo T, Zhou H, *et al.* Direct Atomic-Resolution Observation of Two Phases in the $Li_{1.2}Mn_{0.567}Ni_{0.166}Co_{0.067}O_2$ Cathode Material for Lithium-Ion Batteries. *Angew. Chem. Int. Ed.* **2013,** 52, 5969-5973.

60. Shukla AK, Ramasse QM, Ophus C, Duncan H, Hage F, Chen G. Unravelling structural ambiguities in lithium- and manganese-rich transition metal oxides. *Nat Commun* **2015,** 6.

61. Kim D, Croy JR, Thackeray MM. Comments on stabilizing layered manganese oxide electrodes for Li batteries,. *Electrochem. Commun.* **2013,** 36, 103-106.

62. Kim D, Sandi G, Croy JR, Gallagher KG, Kang S-H, Lee E, *et al.* Composite 'Layered-Layered-Spinel' Cathode Structures for Lithium-Ion Batteries. *J. Electrochem. Soc.* **2013,** 160, A31-A38.

63. Park SH, Sun Y-K. Synthesis and electrochemical properties of layered Li[Li0.15Ni(0.275−x/2)AlxMn(0.575−x/2)]O2 materials prepared by sol–gel method. *J. Power Sources* **2003,** 119–121, 161.

64. Yu Z, Shang S-L, Gordin ML, Mousharraf A, Liu Z-K, Wang D. Ti-substituted $Li[Li_{0.26}Mn_{0.6-x}Ti_xNi_{0.07}Co_{0.07}]O_2$ layered cathode material with improved structural stability and suppressed voltage fading. *J. Mater. Chem. A* **2015,** 3, 17376-17384.

65. Park J-H, Lim J, Yoon J, Park K-S, Gim J, Song J, *et al.* The effects of Mo doping on 0.3Li[Li0.33Mn0.67]O2[middle dot]0.7Li[Ni0.5Co0.2Mn0.3]O2 cathode material. *Dalton Trans.* **2012,** 41, 3053.

66. Yu H, Zhou H. Initial Coulombic efficiency improvement of the $Li_{1.2}Mn_{0.567}Ni_{0.166}Co_{0.067}O_2$ lithium-rich material by ruthenium substitution for manganese. *J. Mater. Chem.* **2012,** 22, 15507.

67. Jiao LF, Zhang M, Yuan HT, Zhao M, Guo J, Wang W, *et al.* Effect of Cr doping on the structural, electrochemical properties of Li[Li0.2Ni0.2−x/2Mn0.6−x/2Crx]O2 (x = 0, 0.02, 0.04, 0.06, 0.08) as cathode materials for lithium secondary batteries. *J. Power Sources* **2007,** 167, 178.

68. Song B, Zhou C, Wang H, Liu H, Liu Z, Lai MO, *et al.* Advances in Sustain Stable Voltage of Cr-Doped Li-Rich Layered Cathodes for Lithium Ion Batteries. *J. Electrochem. Soc.* **2014,** 161, A1723-A1730.

69. Lee CW, Sun Y-K, Prakash J. A novel layered Li [Li0.12NizMg0.32−zMn0.56]O2 cathode material for lithium-ion batteries. *Electrochim. Acta* **2004,** 49, 4425.

70. Li Q, Li G, Fu C, Luo D, Fan J, Li L. $K^+$-Doped $Li_{1.2}Mn_{0.54}Co_{0.13}Ni_{0.13}O_2$: A Novel Cathode Material with an Enhanced Cycling Stability for Lithium-Ion Batteries. *ACS Appl. Mater. Interfaces* **2014,** 6, 10330-10341.

71. Qing R-P, Shi J-L, Xiao D-D, Zhang X-D, Yin Y-X, Zhai Y-B, *et al.* Enhancing the Kinetics of Li-Rich Cathode Materials through the Pinning Effects of Gradient Surface $Na^+$ Doping. *Adv. Energy Mater.* **2015,** 201501914.

72. Zheng Z, Guo X-D, Zhong Y-J, Hua W-B, Shen C-H, Chou S-L, *et al.* Host Structural Stabilization of $Li_{1.232}Mn_{0.615}Ni_{0.154}O_2$ through K-Doping Attempt: toward Superior Electrochemical Performances. *Electrochim. Acta* **2016,** 188, 336-343.

73. Ates MN, Jia Q, Shah A, Busnaina A, Mukerjee S, Abraham KM. Mitigation of Layered to Spinel Conversion of a Li-Rich Layered Metal Oxide Cathode Material for Li-Ion Batteries. *J. Electrochem. Soc.* **2014,** 161, A290-A301.

74. Zheng J, Wu X, Yang Y. Improved electrochemical performance of $Li[Li_{0.2}Mn_{0.54}Ni_{0.13}Co_{0.13}]O_2$ cathode material by fluorine incorporation. *Electrochim. Acta* **2013,** 105, 200-208.

75. Li L, Song BH, Chang YL, Xia H, Yang JR, Lee KS, *et al.* Retarded phase transition by fluorine doping in Li-rich layered $Li_{1.2}Mn_{0.54}Ni_{0.13}Co_{0.13}O_2$ cathode material. *J. Power Sources* **2015,** 283, 162-170.

76. Johnson CS, Li N, Lefief C, Vaughey JT, Thackeray MM. Synthesis, Characterization and Electrochemistry of Lithium Battery Electrodes: $xLi_2MnO_3 \cdot (1-x)LiMn_{0.333}Ni_{0.333}Co_{0.333}O_2$ ($0 \le x \le 0.7$). *Chem. Mater.* **2008,** 20, 6095-6106.

77. Croy JR, Kim D, Balasubramanian M, Gallagher K, Kang S-H, Thackeray MM. Countering the Voltage Decay in High Capacity $xLi_2MnO_3$•$(1-x)LiMO_2$ Electrodes (M=Mn, Ni, Co) for $Li^+$-Ion Batteries. *J. Electrochem. Soc.* **2012,** 159, A781-A790.

78. Wu Y, Manthiram A. High Capacity, Surface-Modified Layered $Li[Li_{(1-x)/3}Mn_{(2-x)/3}Ni_{x/3}Co_{x/3}]O_2$ Cathodes with Low Irreversible Capacity Loss. *Electrochem. Solid-State Lett.* **2006,** 9, A221-A224.

79. Bettge M, Li Y, Sankaran B, Rago ND, Spila T, Haasch RT, *et al.* Improving high-capacity $Li_{1.2}Ni_{0.15}Mn_{0.55}Co_{0.1}O_2$-based lithium-ion cells by modifiying the positive electrode with alumina. *J. Power Sources* **2013,** 233, 346-357.

80. Zheng JM, Li J, Zhang ZR, Guo XJ, Yang Y. The effects of $TiO_2$ coating on the electrochemical performance of $Li[Li_{0.2}Mn_{0.54}Ni_{0.13}Co_{0.13}]O_2$ cathode material for lithium-ion battery. *Solid State Ionics* **2008,** 179, 1794-1799.

81. Zhao Y, Zhao C, Feng H, Sun Z, Xia D. Enhanced Electrochemical Performance of $Li[Li_{0.2}Ni_{0.2}Mn_{0.6}]O_2$ Modified by Manganese Oxide Coating for Lithium-Ion Batteries. *Electrochem. Solid-State Lett.* **2011,** 14, A1-A5.

82. Kang S-H, Thackeray MM. Enhancing the rate capability of high capacity $xLi_2MnO_3$·$(1-x)LiMO_2$ (M=Mn, Ni, Co) electrodes by Li-Ni-$PO_4$ treatment. *Electrochem. Commun.* **2009,** 11, 748-751.

83. Zheng F, Yang C, Xiong X, Xiong J, Hu R, Chen Y, *et al.* Nanoscale Surface Modification of Lithium-Rich Layered-Oxide Composite Cathodes for Suppressing Voltage Fade. *Angew. Chem. Int. Ed.* **2015,** 54, 13058-13062.

84. Liu W, Oh P, Liu X, Myeong S, Cho W, Cho J. Countering Voltage Decay and Capacity Fading of Lithium-Rich Cathode Material at 60 °C by Hybrid Surface Protection Layers. *Adv. Energy Mater.* **2015,** 5, 201500274.

85. Wu F, Li N, Su Y, Zhang L, Bao L, Wang J, *et al.* Ultrathin Spinel Membrane-Encapsulated Layered Lithium-Rich Cathode Material for Advanced Li-Ion Batteries. *Nano Lett.* **2014,** 14, 3550-3555.

86. Zhang J, Lu Q, Fang J, Wang J, Yang J, NuLi Y. Polyimide Encapsulated Lithium-Rich Cathode Material for High Voltage Lithium-Ion Battery. *ACS Appl. Mater. Interfaces* **2014,** 6, 17965-17973.

87. Wu C, Fang X, Guo X, Mao Y, Ma J, Zhao C, *et al.* Surface modification of $Li_{1.2}Mn_{0.54}Co_{0.13}Ni_{0.13}O_2$ with conducting polypyrrole. *J. Power Sources* **2013,** 231, 44-49.

88. Li J, Xing L, Zhang R, Chen M, Wang Z, Xu M*, et al.* Tris(trimethylsilyl)borate as an electrolyte additive for improving interfacial stability of high voltage layered lithium-rich oxide cathode/carbonate-based electrolyte. *J. Power Sources* **2015,** 285, 360-366.

89. Lee SJ, Han J-G, Park I, Song J, Cho J, Kim J-S*, et al.* Effect of Lithium Bis(oxalato)borate Additive on Electrochemical Performance of $Li_{1.17}Ni_{0.17}Mn_{0.5}Co_{0.17}O_2$ Cathodes for Lithium-Ion Batteries. *J. Electrochem. Soc.* **2014,** 161, A2012-A2019.

90. Nayak PK, Grinblat J, Levi M, Aurbach D. Understanding the Effect of Lithium Bis(oxalato) Borate (LiBOB) on the Structural and Electrochemical Aging of Li and Mn Rich High Capacity $Li_{1.2}Ni_{0.16}Mn_{0.56}Co_{0.08}O_2$ Cathodes. *J. Electrochem. Soc.* **2015,** 162, A596-A602.

91. Tan S, Zhang Z, Li Y, Li Y, Zheng J, Zhou Z*, et al.* Tris(hexafluoro-iso-propyl)phosphate as an SEI-Forming Additive on Improving the Electrochemical Performance of the $Li[Li_{0.2}Mn_{0.56}Ni_{0.16}Co_{0.08}]O_2$ Cathode Material. *J. Electrochem. Soc.* **2013,** 160, A285-A292.

92. Ji Y, Zhang Z, Gao M, Li Y, McDonald MJ, Yang Y. Electrochemical Behavior of Suberonitrile as a High-Potential Electrolyte Additive and Co-Solvent for $Li[Li_{0.2}Mn_{0.56}Ni_{0.16}Co_{0.08}]O_2$ Cathode Material. *J. Electrochem. Soc.* **2015,** 162, A774-A780.

93. Patra J, Dahiya PP, Tseng C-J, Fang J, Lin Y-W, Basu S*, et al.* Electrochemical performance of $0.5Li_2MnO_3–0.5Li(Mn_{0.375}Ni_{0.375}Co_{0.25})O_2$ composite cathode in pyrrolidinium-based ionic liquid electrolytes. *J. Power Sources* **2015,** 294, 22-30.

94. Pham HQ, Nam K-M, Hwang E-H, Kwon Y-G, Jung HM, Song S-W. Performance Enhancement of 4.8 V $Li_{1.2}Mn_{0.525}Ni_{0.175}Co_{0.1}O_2$ Battery Cathode Using Fluorinated Linear Carbonate as a High-Voltage Additive. *J. Electrochem. Soc.* **2014,** 161, A2002-A2011.

95. Zheng JM, Zhang ZR, Wu XB, Dong ZX, Zhu Z, Yang Y. The Effects of $AlF_3$ Coating on the Performance of $Li[Li_{0.2}Mn_{0.54}Ni_{0.13}Co_{0.13}]O_2$ Positive Electrode Material for Lithium-Ion Battery. *J. Electrochem. Soc.* **2008,** 155, A775.

96. Li LF, Lee HS, Li H, Yang XQ, Nam KW, Yoon WS*, et al.* New electrolytes for lithium ion batteries using LiF salt and boron based anion receptors. *J. Power Sources* **2008,** 184, 517.

97. Choi N-S, Jeong G, Koo B, Lee Y-W, Lee KT. Tris(pentafluorophenyl) borane-containing electrolytes for electrochemical reversibility of lithium peroxide-based electrodes in lithium–oxygen batteries. *J. Power Sources* **2013,** 225, 95.

98. De Giorgio F, Soavi F, Mastragostino M. Effect of lithium ions on oxygen reduction in ionic liquid-based electrolytes. *Electrochem. Commun.* **2011,** 13, 1090.

99. Xie B, Lee HS, Li H, Yang XQ, McBreen J, Chen LQ. New electrolytes using Li2O or Li2O2 oxides and tris(pentafluorophenyl) borane as boron based anion receptor for lithium batteries. *Electrochem. Commun.* **2008,** 10, 1195.

100. Hong J, Gwon H, Jung SK, Ku K, Kanga K. Review-Lithium-Excess layered cathodes for lithium rechargeable batteries. *J. Electrochem. Soc.* **2015,** 162, A2447-A2467.

101. Mohanty D, Li J, Nagpure SC, Wood DL, Daniel C. Understanding the structure and structural degradation mechanisms in high-voltage, lithium-manganese–rich lithium-ion battery cathode oxides: A review of materials diagnostics. *MRS Energy Sustainabil.* **2015,** 2, E15.

102. Rozier P, Tarascon JM. Review-Li-rich layered oxide cathodes for next-generation Li-ion batteries: Chances and challenges. *J. Electrochem. Soc.* **2015,** 162, A2490-A2499.

103. Yan J, Liu X, Li B. Recent progress in Li-rich layered oxides as cathode materials for Li-ion batteries. *RSC Advances* **2014,** 4, 63268-63284.

104. Zheng J, Myeong S, Cho W, Yan P, Xiao J, Wang C*, et al.* Li- and Mn-Rich Cathode Materials: Challenges to Commercialization. *Adv. Energy Mater.* **2017,** 7.

105. Armstrong AR, Holzapfel M, Novák P, Johnson CS, Kang SH, Thackeray MM*, et al.* Demonstrating oxygen loss and associated structural reorganization in the lithium battery cathode $Li[Ni_{0.2}Li_{0.2}Mn_{0.6}]O_2$. *J. Am. Chem. Soc.* **2006,** 128, 8694-8698.

106. Castel E, Berg EJ, El Kazzi M, Novák P, Villevieille C. Differential electrochemical mass spectrometry study of the interface of x $Li_2MnO_3$·(1- x)$LiMO_2$ (M = Ni, Co, and Mn) material as a positive electrode in li-ion batteries. *Chem. Mater.* **2014,** 26, 5051-5057.

107. Luo K, Roberts MR, Hao R, Guerrini N, Pickup DM, Liu YS*, et al.* Charge-compensation in 3d-transition-metal-oxide intercalation cathodes through the generation of localized electron holes on oxygen. *Nat Chem* **2016,** 8, 684-691.

108. Hong J, Lim HD, Lee M, Kim SW, Kim H, Oh ST*, et al.* Critical role of oxygen evolved from layered Li-Excess metal oxides in lithium rechargeable batteries. *Chem. Mater.* **2012,** 24, 2692-2697.

109. Hy S, Felix F, Rick J, Su WN, Hwang BJ. Direct in situ observation of Li2O evolution on Li-rich high-capacity cathode material, $Li[Ni_xLi_{(1-2x)/3}Mn_{(2-x)/3}]O_2$ ($0 \leq x \leq 0.5$). *J. Am. Chem. Soc.* **2014,** 136, 999-1007.

110. Cho IH, Kim SS, Shin SC, Choi NS. Effect of SEI on capacity losses of spinel lithium manganese oxide/graphite batteries stored at 60°C. *Electrochem. Solid-State Lett.* **2010,** 13, A168-A172.

111. Aoshima T, Okahara K, Kiyohara C, Shizuka K. Mechanisms of manganese spinels dissolution and capacity fade at high temperature. *J. Power Sources* **2001,** 97-98, 377-380.

112. Chang HJ, Ilott AJ, Trease NM, Mohammadi M, Jerschow A, Grey CP. Correlating Microstructural Lithium Metal Growth with Electrolyte Salt Depletion in Lithium Batteries Using7Li MRI. *J. Am. Chem. Soc.* **2015,** 137, 15209-15216.

113. Gu M, Belharouak I, Zheng J, Wu H, Xiao J, Genc A*, et al.* Formation of the spinel phase in the layered composite cathode used in Li-ion batteries. *ACS nano* **2013,** 7, 760-767.

114. Oh P, Ko M, Myeong S, Kim Y, Cho J. A novel surface treatment method and new insight into discharge voltage deterioration for high-performance 0.4Li2MnO3-0.6LiNi1/3Co1/3Mn1/3O2cathode materials. *Adv. Energy Mater.* **2014,** 4.

115. Xu B, Fell CR, Chi MF, Meng YS. Identifying surface structural changes in layered Li-excess nickel manganese oxides in high voltage lithium ion batteries: A joint experimental and theoretical study. *Energy & Environmental Science* **2011,** 4, 2223-2233.

116. Kim S, Cho W, Zhang X, Oshima Y, Choi JW. A stable lithium-rich surface structure for lithium-rich layered cathode materials. *Nature Communications* **2016,** 7.

117. Qiao QQ, Zhang HZ, Li GR, Ye SH, Wang CW, Gao XP. Surface modification of Li-rich layered Li(Li0.17Ni 0.25Mn0.58)O2 oxide with Li-Mn-PO4 as the cathode for lithium-ion batteries. *J. Mater. Chem.* **2013,** 1, 5262-5268.

118. Zheng J, Gu M, Xiao J, Polzin BJ, Yan P, Chen X*, et al.* Functioning mechanism of AlF3 coating on the Li- and Mn-rich cathode materials. *Chem. Mater.* **2014,** 26, 6320-6327.

119. Tebbe JL, Holder AM, Musgrave CB. Mechanisms of LiCoO2 Cathode Degradation by Reaction with HF and Protection by Thin Oxide Coatings. *ACS Applied Materials and Interfaces* **2015,** 7, 24265-24278.

120. Moses AW, Flores HGG, Kim JG, Langell MA. Surface properties of LiCoO2, LiNiO2and LiNi1-xCoxO2. *Applied Surface Science* **2007,** 253, 4782-4791.

121. Danks AE, Hall SR, Schnepp Z. The evolution of 'sol-gel' chemistry as a technique for materials synthesis. *Materials Horizons* **2016,** 3, 91-112.

122. Wu F, Li N, Su Y, Zhang L, Bao L, Wang J*, et al.* Ultrathin spinel membrane-encapsulated layered lithium-rich cathode material for advanced Li-ion batteries. *Nano Lett.* **2014,** 14, 3550-3555.

123. Zheng F, Yang C, Xiong X, Xiong J, Hu R, Chen Y*, et al.* Nanoscale Surface Modification of Lithium-Rich Layered-Oxide Composite Cathodes for Suppressing Voltage Fade. *Angew. Chem. Int. Ed.* **2015,** 54, 13058-13062.

124. Liu W, Oh P, Liu X, Myeong S, Cho W, Cho J. Countering Voltage Decay and Capacity Fading of Lithium-Rich Cathode Material at 60 °c by Hybrid Surface Protection Layers. *Adv. Energy Mater.* **2015,** 5.

125. Xu S, Luo G, Jacobs R, Fang S, Mahanthappa MK, Hamers RJ*, et al.* Ab Initio Modeling of Electrolyte Molecule Ethylene Carbonate Decomposition Reaction on Li(Ni,Mn,Co)O2Cathode Surface. *ACS Applied Materials and Interfaces* **2017,** 9, 20545-20553.

126. Živković ZD, Dobovišek B. Kinetics of aluminium hydroxide dehydration. *Journal of Thermal Analysis* **1977,** 12, 207-215.

127. Zhu B, Fang B, Li X. Dehydration reactions and kinetic parameters of gibbsite. *Ceramics International* **2010,** 36, 2493-2498.

128. Lagunas MC, Pitner WR, Van Den Berg JA, Seddon KR. Solvent-solute interactions in ionic liquid media: Electrochemical studies of the ferricenium-ferrocene couple. *ACS Symposium Series*; 2003. pp. 421-438.

129. Socrates G. Infrared and Raman characteristic group frequencies: tables and charts. *Infrared Raman Charact. Gr. Freq.* **2017,** 4508819.

130. Malmgren S, Ciosek K, Hahlin M, Gustafsson T, Gorgoi M, Rensmo H*, et al.* Comparing anode and cathode electrode/electrolyte interface composition and morphology using soft and hard X-ray photoelectron spectroscopy. *Electrochim. Acta* **2013,** 97, 23-32.

131. Zheng J, Gu M, Genc A, Xiao J, Xu P, Chen X*, et al.* Mitigating voltage fade in cathode materials by improving the atomic level uniformity of elemental distribution. *Nano Lett.* **2014,** 14, 2628-2635.

132. Sathiya M, Abakumov AM, Foix D, Rousse G, Ramesha K, Saubanere M*, et al.* Origin of voltage decay in high-capacity layered oxide electrodes. *Nat Mater* **2015,** 14, 230-238.

133. Edström K, Gustafsson T, Thomas JO. The cathode-electrolyte interface in the Li-ion battery. *Electrochim. Acta* **2004,** 50, 397-403.

134. Zheng J, Xu P, Gu M, Xiao J, Browning ND, Yan P*, et al.* Structural and chemical evolution of Li- and Mn-rich layered cathode material. *Chem. Mater.* **2015,** 27, 1381-1390.

135. Vetter J, Novák P, Wagner MR, Veit C, Möller KC, Besenhard JO*, et al.* Ageing mechanisms in lithium-ion batteries. *J. Power Sources* **2005,** 147, 269-281.

136. Campion CL, Li W, Lucht BL. Thermal decomposition of LiPF 6-based electrolytes for lithium-ion batteries. *J. Electrochem. Soc.* **2005,** 152, A2327-A2334.

137. Arora P, White RE, Doyle M. Capacity fade mechanisms and side reactions in lithium-ion batteries. *J. Electrochem. Soc.* **1998,** 145, 3647-3667.

138. Goodenough JB, Kim Y. Challenges for rechargeable Li batteries. *Chem. Mater.* **2010,** 22, 587-603.

139. Whittingham MS. Lithium batteries and cathode materials. *Chem. Rev.* **2004,** 104, 4271-4301.

140. Palacín MR. Recent advances in rechargeable battery materials: A chemist's perspective. *Chem. Soc. Rev.* **2009,** 38, 2565-2575.

141. Thackeray MM, Kang SH, Johnson CS, Vaughey JT, Benedek R, Hackney SA. Li(2)MnO(3)-stabilized LiMO(2) (M = Mn, Ni, Co) electrodes for lithium-ion batteries. *J. Mater. Chem.* **2007,** 17, 3112-3125.

142. Zhou F, Zhao X, Van Bommel A, Xia X, Dahn JR. Comparison of Li [Li1/9 Ni1/3 Mn5/9] O2, Li [Li1/5 Ni1/5 Mn3/5] O 2, Li Ni0.5 Mn1.5 O4, and Li Ni 2/3 Mn1/3 O2 as High Voltage Positive Electrode Materials. *J. Electrochem. Soc.* **2011,** 158, A187-A191.

143. Bettge M, Li Y, Gallagher K, Zhu Y, Wu Q, Lu W*, et al.* Voltage fade of layered oxides: Its measurement and impact on energy density. *J. Electrochem. Soc.* **2013,** 160, A2046-A2055.

144. Gallagher KG, Croy JR, Balasubramanian M, Bettge M, Abraham DP, Burrell AK, *et al.* Correlating hysteresis and voltage fade in lithium- and manganese-rich layered transition-metal oxide electrodes. *Electrochemistry Communications* **2013,** 33, 96-98.

145. Croy JR, Kim D, Balasubramanian M, Gallagher K, Kang SH, Thackeray MM. Countering the Voltage Decay in High Capacity xLi(2)MnO(3)center dot(1-x)LiMO2 Electrodes (M=Mn, Ni, Co) for Li+-Ion Batteries. *J. Electrochem. Soc.* **2012,** 159, A781-A790.

146. Yu XQ, Lyu YC, Gu L, Wu HM, Bak SM, Zhou YN, *et al.* Understanding the Rate Capability of High-Energy-Density Li-Rich Layered Li 1.2 Ni 0.15 Co 0.1 Mn 0.55 O 2 Cathode Materials. *Adv. Energy Mater.* **2014,** 4.

147. Shimoda K, Oishi M, Matsunaga T, Murakami M, Yamanaka K, Arai H, *et al.* Direct observation of layered-to-spinel phase transformation in Li2MnO3and the spinel structure stabilised after the activation process. *J. Mater. Chem. A* **2017,** 5, 6695-6707.

148. Shi JL, Zhang JN, He M, Zhang XD, Yin YX, Li H, *et al.* Mitigating Voltage Decay of Li-Rich Cathode Material via Increasing Ni Content for Lithium-Ion Batteries. *ACS Appl Mater Interfaces* **2016,** 8, 20138-20146.

149. Shi J-L, Xiao D-D, Zhang X-D, Yin Y-X, Guo Y-G, Gu L, *et al.* Improving the structural stability of Li-rich cathode materials via reservation of cations in the Li-slab for Li-ion batteries. *Nano Research* **2017**.

150. Oh P, Ko M, Myeong S, Kim Y, Cho J. A novel surface treatment method and new insight into discharge voltage deterioration for high-performance 0.4Li2MnO3-0.6LiNi1/3Co1/3Mn1/3O2 cathode materials. *Adv. Energy Mater.* **2014,** 4.

151. Yan P, Nie A, Zheng J, Zhou Y, Lu D, Zhang X, *et al.* Evolution of lattice structure and chemical composition of the surface reconstruction layer in Li(1.2)Ni(0.2)Mn(0.6)O2 cathode material for lithium ion batteries. *Nano Lett.* **2015,** 15, 514-522.

152. Zheng J, Gu M, Xiao J, Zuo P, Wang C, Zhang JG. Corrosion/fragmentation of layered composite cathode and related capacity/voltage fading during cycling process. *Nano Lett* **2013,** 13, 3824-3830.

153. Mohanty D, Sefat AS, Kalnaus S, Li JL, Meisner RA, Payzant EA, *et al.* Investigating phase transformation in the Li1.2Co0.1Mn0.55Ni0.15O2 lithium-ion battery cathode during high-voltage hold (4.5 V) via magnetic, X-ray diffraction and electron microscopy studies. *J. Mater. Chem. A* **2013,** 1, 6249-6261.

154. Wu Y, Ma C, Yang J, Li Z, Allard LF, Liang C, *et al.* Probing the initiation of voltage decay in Li-rich layered cathode materials at the atomic scale. *Journal of Materials Chemistry A* **2015,** 3, 5385-5391.

155. Hong J, Seo DH, Kim SW, Gwon H, Oh ST, Kang K. Structural evolution of layered Li1.2Ni0.2Mn0.6O2 upon electrochemical cycling in a Li rechargeable battery. *J. Mater. Chem.* **2010,** 20, 10179-10186.

156. Liu WD, Oh PD, Liu XD, Myeong S, Cho W, Cho J. Countering Voltage Decay and Capacity Fading of Lithium-Rich Cathode Material at 60 °c by Hybrid Surface Protection Layers. *Adv. Energy Mater.* **2015,** 5.

157. Yan P, Xiao L, Zheng J, Zhou Y, He Y, Zu X, *et al.* Probing the Degradation Mechanism of Li2MnO3 Cathode for Li-Ion Batteries. *Chem. Mater.* **2015,** 27, 975-982.

158. Jarvis KA, Wang C-C, Manthiram A, Ferreira PJ. The role of composition in the atomic structure, oxygen loss, and capacity of layered Li–Mn–Ni oxide cathodes. *J. Mater. Chem. A* **2014,** 2, 1353-1362.

159. Goodenough JB. Perspective on engineering transition-metal oxides. *Chem. Mater.* **2014,** 26, 820-829.

160. Seo DH, Lee J, Urban A, Malik R, Kang S, Ceder G. The structural and chemical origin of the oxygen redox activity in layered and cation-disordered Li-excess cathode materials. *Nature chemistry* **2016,** 8, 692-697.

161. Luo K, Roberts MR, Guerrini N, Tapia-Ruiz N, Hao R, Massel F, *et al.* Anion Redox Chemistry in the Cobalt Free 3d Transition Metal Oxide Intercalation Electrode Li[Li0.2Ni0.2Mn0.6]O2. *J. Am. Chem. Soc.* **2016,** 138, 11211-11218.

162. Kiss AM, Harris WM, Wang S, Vila-Comamala J, Deriy A, Chiu WKS. In-situ observation of nickel oxidation using synchrotron based full-field transmission X-ray microscopy. *Appl. Phys. Lett.* **2013,** 102.

163. Simonin L, Colin JF, Ranieri V, Canevet E, Martin JF, Bourbon C, *et al.* In situ investigations of a Li-rich Mn-Ni layered oxide for Li-ion batteries. *J. Mater. Chem.* **2012,** 22, 11316-11322.

164. Oishi M, Fujimoto T, Takanashi Y, Orikasa Y, Kawamura A, Ina T, *et al.* Charge compensation mechanisms in Li1.16Ni0.15Co0.19Mn0.50O2 positive electrode material for Li-ion batteries analyzed by a combination of hard and soft X-ray absorption near edge structure. *J. Power Sources* **2013,** 222, 45-51.

165. Oishi M, Yamanaka K, Watanabe I, Shimoda K, Matsunaga T, Arai H*, et al.* Direct observation of reversible oxygen anion redox reaction in Li-rich manganese oxide, Li2MnO3, studied by soft X-ray absorption spectroscopy. *Journal of Materials Chemistry A* **2016,** 4, 9293-9302.

166. Yan W, Sun Z, Pan Z, Liu Q, Yao T, Wu Z*, et al.* Oxygen vacancy effect on room-temperature ferromagnetism of rutile Co:TiO2 thin films. *Appl. Phys. Lett.* **2009,** 94, 042508.

167. Yu H, So YG, Kuwabara A, Tochigi E, Shibata N, Kudo T*, et al.* Crystalline Grain Interior Configuration Affects Lithium Migration Kinetics in Li-Rich Layered Oxide. *Nano Lett.* **2016,** 16, 2907-2915.

168. Bareno J, Lei CH, Wen JG, Kang SH, Petrov I, Abraham DP. Local structure of layered oxide electrode materials for lithium-ion batteries. *Adv. Mater.* **2010,** 22, 1122-1127.

169. Boulineau A, Simonin L, Colin J-F, Canévet E, Daniel L, Patoux S. Evolutions of Li1.2Mn0.61Ni0.18Mg0.01O2 during the Initial Charge/Discharge Cycle Studied by Advanced Electron Microscopy. *Chem. Mater.* **2012,** 24, 3558-3566.

170. Jarvis KA, Deng Z, Allard LF, Manthiram A, Ferreira PJ. Atomic Structure of a Lithium-Rich Layered Oxide Material for Lithium-Ion Batteries: Evidence of a Solid Solution. *Chem. Mater.* **2011,** 23, 3614-3621.

171. Jarvis KA, Deng Z, Allard LF, Manthiram A, Ferreira PJ. Understanding structural defects in lithium-rich layered oxide cathodes. *J. Mater. Chem.* **2012,** 22, 11550.

172. Rana J, Kloepsch R, Li J, Scherb T, Schumacher G, Winter M*, et al.* On the structural integrity and electrochemical activity of a 0.5Li(2)MnO(3)center dot 0.5LiCoO(2) cathode material for lithium-ion batteries. *J. Mater. Chem. A* **2014,** 2, 9099-9110.

173. Croguennec L, Pouillerie C, Delmas C. NiO2 obtained by electrochemical lithium deintercalation from lithium nickelate: structural modifications. *J. Electrochem. Soc.* **2000,** 147, 1314-1321.

174. Croguennec L, Pouillerie C, Mansour AN, Delmas C. Structural characterisation of the highly deintercalated LixNi1.02O2 phases (with x≤0.30). *J. Mater. Chem.* **2001,** 11, 131-141.

175. Yin SC, Rho YH, Swainson I, Nazar LF. X-ray/neutron diffraction and electrochemical studies of lithium De/Re-intercalation in Li1-xCo1/3Ni1/3Mn 1/3O2 (x = 0 → 1). *Chem. Mater.* **2006,** 18, 1901-1910.

176. Kim MG, Yo CH. X-ray Absorption Spectroscopic Study of Chemically and Electrochemically Li Ion Extracted LiyCo$_{0.85}$Al0.15O2 Compounds. *J. Phys. Chem. B* **1999,** 103, 6457-6465.

177. Rana J, Kloepsch R, Li J, Stan M, Schumacher G, Winter M*, et al*. Structural Changes in a Li-Rich 0.5Li$_2$MnO$_3$*0.5LiMn$_{0.4}$Ni$_{0.4}$Co$_{0.2}$O$_2$Cathode Material for Li-Ion Batteries: A Local Perspective. *J. Electrochem. Soc.* **2016,** 163, A811-A820.